REACTIVITY CHANGES DURING STARTUP
IN LARGE NUCLEAR ROCKETS

by

Winston W. Little, Jr.

Supervisors: Edward A. Mason

Kent F. Hansen

Department of Nuclear Engineering

Massachusetts Institute of Technology

Cambridge, Massachusetts

AUGUST, 1964

REACTIVITY CHANGES DURING STARTUP
IN LARGE NUCLEAR ROCKETS

by

Winston W. Little, Jr.

Submitted in Partial Fulfillment
of the Requirements for the Degree of
Doctor of Science
at the
Massachusetts Institute of Technology

Supervisors: Edward A. Mason
Kent F. Hansen

DEPARTMENT OF NUCLEAR ENGINEERING
MASSACHUSETTS INSTITUTE OF TECHNOLOGY
Cambridge, Massachusetts

August, 1964

REACTIVITY CHANGES DURING STARTUP
IN LARGE NUCLEAR ROCKETS

by

Winston W. Little, Jr.

ABSTRACT

)1/46

The objective of this thesis was to investigate some of the nucleonic problems associated with starting large, solid core nuclear rockets fueled with uranium-235. Primary emphasis was placed on obtaining the reactivity variations during startup induced by changes in hydrogen density and core temperature.

A detailed nucleonic analysis of a nuclear rocket during startup would be extremely complex and time consuming. In order to make the problem tractable, the following procedure was adopted. First, the material properties, such as core temperature, hydrogen density, etc., were computed as a function of time during startup for a specified power and flow rate buildup. Using these time dependent properties, the reactivity variations during startup were calculated using a diffusion theory model with 55 energy groups. The spatial dimensions were approximated by assuming $\nabla^2\phi(E) = -B^2\phi(E)$. Such an assumption should be permissible in light of the fact that changes in core temperature and hydrogen density have little effect on the spatial distribution, but have a significant effect on the energy distribution.

It was found that large thermal nuclear rocket reactors (C/U = 2500) are much more sensitive to changes in hydrogen density and core temperature than small nuclear rockets (C/U = 250). The large reactivity coefficients present in thermal reactors cause both large ($\sim -\$13.$) and rapid ($\sim -\$1./$sec) reactivity variations during the quick startups contemplated for nuclear rockets. This problem can be ameliorated to some degree by adding a nuclear poison to the core. However, any poison has the adverse side effect of decreasing the worth of an external control rod system by decreasing the leakage.

An estimation of the worth of an external control rod system was obtained using a one-dimensional nucleonics model with three energy groups. It was found that thermal reactors would require very thick and heavy reflectors in order to control the reactivity variation during startup.

ACKNOWLEDGMENTS

TABLE OF CONTENTS

6

8

LIST OF FIGURES

LIST OF TABLES

I. INTRODUCTION

1.1 Sketch of Nuclear Rocket History

On December 2, 1942, Enrico Fermi and his colleagues demonstrated that it was indeed possible to achieve a controllable neutron chain reaction (1). The event was of trancendent importance. For the first time, man had at his disposal an incredibly compact energy supply. It was perhaps inevitable that man would attempt to employ this vast energy source to aid in space propulsion.

As early as 1944, Stan Ulam and F. de Hoffmann published speculations on possible methods to utilize nuclear energy for propulsion (2). By the early 1950's, a number of survey papers were available on various means to convert nuclear heat to rocket thrust (3).

However, prior to 1955, only preliminary studies had been performed on solid core nuclear rockets. In particular, there was very little information available on the physical and chemical properties of material at elevated temperatures, which was of critical importance for the adequate evaluation of possible nuclear rockets.

Solid core nuclear rocket development was begun in earnest in 1955 with the initiation of the Rover project (4). This program has as its objective the development of heat-exchanger nuclear rockets.

1.2 Fundamentals of Nuclear Rockets

In principle, a nuclear rocket is quite simple. A schematic diagram showing the essential components of a nuclear rocket is given in Figure 1.2.1.

The liquid propellant is pumped into the reactor core, heated, then accelerated by a converging-diverging nozzle to achieve thrust. Heated propellant supplies energy to the turbine, which drives the pump.

14
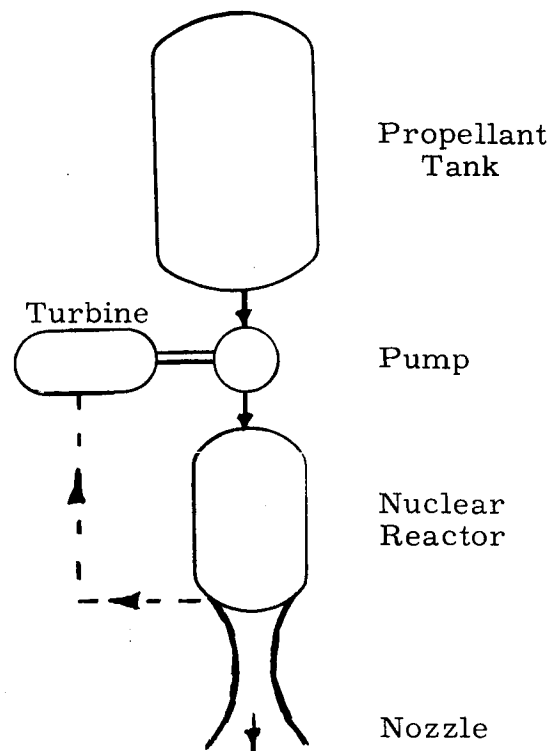
Figure 1.2.1. Schematic Diagram of Nuclear Rocket

It is important to understand that the mission capability of a nuclear rocket is limited only by the amount of propellant it can carry aloft. In other words, the nuclear engine in a nuclear rocket could, if required, supply an almost inexhaustible amount of energy. But energy, per se, is of no value because mass (propellant) must be expelled from the rocket system to produce thrust.

Observe that the above situation is in distinct contrast with a chemical rocket, which must obtain both energy and thrust from the propellant. This fact sharply restricts the choice of propellants which can be used in a chemical rocket. It is precisely the freedom of choice of propellant which gives nuclear rockets a clear advantage over chemical rockets.

1.3 Advantages of Nuclear Rockets

The relative merits of nuclear and chemical rockets have been discussed at length by numerous authors (5, 6). The objective of this section is to demonstrate the advantages possessed by nuclear rockets using very elementary mathematical models. Emphasis will be placed on physical concepts rather than mathematical detail.

Consider a rocket of mass $m(t)$, expelling propellant at a constant velocity v_e with respect to the rocket. In a gravity-free environment, the rocket velocity, v, can be obtained from Newton's Second Law. Neglecting air resistance and nozzle exhaust pressure,

$$\frac{d}{dt}(mv) = -\frac{dm}{dt}(v_e - v) \tag{1.3.1}$$

or

$$m\frac{dv}{dt} = -\frac{dm}{dt}v_e \tag{1.3.2}$$

If the initial rocket velocity is assumed to be zero, the solution of Eq. (1.3.1) is

$$v_f = v_e \ln(m_o/m_f) \tag{1.3.3}$$

where the subscripts o and f denote the initial and final values, respectively.

Assuming that the ratio m_o/m_f is approximately the same for both chemical and nuclear rockets, it is clear from Eq. (1.3.3) that the propellant exhaust velocity is the most important figure of merit in judging the relative performance of nuclear and chemical rockets.

Both nuclear and chemical rockets produce thrust by accelerating a hot gas through a converging-diverging nozzle. In such a system, the exhaust velocity is easy to compute. Consider the nozzle shown in Figure 1.3.1.
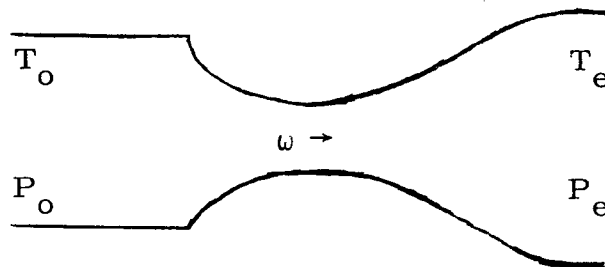
Figure 1.3.1. Schematic Diagram of Exhaust Nozzle

For adiabatic flow, the well known First Law energy flow equation has the form

$$h_o = v_e^2/2 + h_e \tag{1.3.4}$$

where all symbols are defined in Table 1.3.1. Assuming reversible expansion of a perfect gas, Eq. (1.3.4) becomes

$$v_e = \sqrt{2C_p(T_o - T_e)} \tag{1.3.5}$$

or

$$v_e = \sqrt{\frac{2\gamma\eta R T_o}{(\gamma-1)\underline{M}}} \tag{1.3.6}$$

where

$$\eta = 1 - T_e/T_o = 1 - (P_e/P_o)^{(\gamma-1)/\gamma} \tag{1.3.7}$$

If γ, η, and T_o are assumed to be approximately the same for chemical and nuclear rocket systems, the important parameter in evaluating rocket performance is clearly the propellant weight, $\underline{M}$. Because $v_e \propto 1/\sqrt{M}$, it is highly desirable to use a propellant with a low molecular weight. Advanced chemical rockets burn a mixture of hydrogen and oxygen, which has an average molecular weight of about 9. Nuclear rockets employ the lightest of fluids, molecular hydrogen; hence the exhaust velocity of a nuclear rocket is approximately $\sqrt{\frac{9}{2}} \cong$ 2.1 times greater than a chemical rocket.

In a practical sense, a gain of a factor of two in exhaust velocity is very significant. To illustrate the advantage more graphically, let us rewrite Eq. (1.3.3) in the form

$$m_o = m_f \exp(v_f/v_e) \tag{1.3.8}$$

For example, for a chemical rocket, assume $m_o = 10m_f$. For a speci-·fied final velocity v_f, and final mass m_f, an increase of a factor of two in the exhaust velocity reduces the initial rocket mass, m_o, to 3.15 m_f. Therefore, for a given mission using a one-stage rocket, we have decreased the initial rocket weight by over a factor of three simply by using nuclear propulsion. An even greater weight reduction is possible using larger multi-stage rockets. Conversely, for a fixed initial rocket

mass, the final rocket mass can be increased by a factor of 3 by employing nuclear propulsion.

The above analysis is rather elementary. A precise investigation would include many other factors. In fairness to chemical rockets, it should be mentioned that nuclear rockets have a number of disadvantages. First, the nuclear engine, or reactor, penalizes a nuclear rocket system because of its weight. Second, and probably of more significance, is the fact that hydrogen has a low density (~.07 gm/cc). For a given total propellant mass, a nuclear rocket therefore requires a larger propellant tank than a chemical rocket. However, in spite of these and other difficulties, a nuclear rocket is much better suited than a chemical rocket for the performance of long missions with heavy payloads.

<div align="center">Table 1.3.1. Symbols Used in Chapter I.</div>

C_p	propellant heat capacity
h_e	enthalpy at nozzle exhaust
h_o	stagnation enthalpy at nozzle entrance
$\underline{M}$	propellant molecular weight
m	mass of rocket
m_o	initial rocket mass
m_f	final rocket mass
P_e	propellant pressure at nozzle exhaust
P_o	propellant stagnation pressure at nozzle entrance
R	universal gas constant
t	time
T_e	propellant temperature at nozzle exhaust
T_o	stagnation temperature at nozzle entrance
v	rocket velocity
v_e	exhaust velocity of propellant
v_f	final rocket velocity
ω	propellant flow rate
η	Carnot efficiency, defined by Equation (1.3.7)
γ	gas constant (C_p/C_v)

1.4 Current Status of Nuclear Rocket Development

Graphite moderated nuclear rockets are being developed under Project Rover, which is managed by the Space Nuclear Propulsion Office (SNPO) (7). The first generation of nuclear rocket reactors, which are incapable of flying, are designed to give a proof of principle. These reactors are appropriately called Kiwi reactors, after the flightless Australian bird. To date, a number of Kiwi reactors have been tested. Unfortunately, the Kiwi B-1B and B-4A hot flow tests using liquid hydrogen were plagued with vibration problems (8). These difficulties delayed the program for over a year. However, it is now thought that these difficulties have been identified and corrected (9). The Kiwi B-4D test, which was run on May 13, 1964, gave no indication of vibration (10).

The NERVA reactors, or Nuclear Engine for Rocket Vehicle Application, are operational models of the basic Kiwi reactor. These reactors are being built by Aerojet General-Westinghouse. The first NERVA ground test is expected in mid-1964 (11).

It should be pointed out that the thrust level of the NERVA rocket engine is rather small compared to that of present chemical rockets. The power is estimated to be 1000 Mw (12), which is equivalent to about 50,000 lbs thrust. Hence, it would be useful only as an upper stage of a large chemical rocket.

1.5 Startup of Large Nuclear Rockets: Statement of Problem

In order for a nuclear rocket to produce a thrust comparable to large chemical rockets ($\sim 10^6$ lb), the reactor core must be rather large. The necessary core size is easy to estimate. If we assume a power density of 2 Mw/liter (13), and employ the rule of thumb for nuclear rockets (6) that

$$\text{Thrust (lb)} \approx 50 \times \text{Power (Mw)} \tag{1.5.1}$$

the core volume, V_c, is given by the approximation

$$V_c \text{ (m}^3\text{)} \approx 10^{-5} \times \text{Thrust (lb)} \tag{1.5.2}$$

Therefore, a rocket reactor producing a thrust in the range of 10^6 lbs must have dimensions of several meters.

Such large reactors pose serious nucleonics problems. If the core size is increased, the ratio of carbon to fuel (C/U) will be larger; hence, the spectrum will be more thermal. This, in turn, indicates that the reactivity changes during startup, caused by variations in hydrogen density and temperature, may be too large or too rapid to control.

II. OBJECTIVE AND OUTLINE

2.1 Purpose

In general terms, the objective of this thesis is to investigate some of the nucleonics problems encountered in starting large nuclear rockets. The study is restricted to the analysis of graphite-moderated nuclear rocket reactors fueled with uranium-235. Primary emphasis is placed on finding the effect of changes in hydrogen density and core temperature on reactivity during startup. Other facets of the startup problem which are considered include an estimate of the reactivity worth of an external control system, and an evaluation of the consequences of an inadvertent prompt critical excursion.

2.2 Thesis Outline

In Chapter III, a nucleonics model is set up which computes changes in reactivity induced by changes in core temperature and hydrogen density. This is a multigroup model with no time or space dependence.

The spatially dependent core temperature and hydrogen density startup are computed in Chapter IV. For these calculations, it is assumed that the power and flow rate follow a specified time profile during startup (i.e., programmed). Using an averaging procedure discussed in Chapter V, lumped values of core temperature and hydrogen density are then substituted into the reactivity model to obtain the reactivity changes during startup caused by changes in core temperature and hydrogen density. In other words, the multigroup nucleonics model is used to take "snapshots" of the reactivity using data supplied by the fluid flow model.

The severity of a given reactivity variation depends, in part, on the magnitude of the reactivity required to achieve the desired power increase and the total reactivity worth of the control system. These factors are estimated in Chapters VI and VII, respectively. For example, if the reactivity variation induced by changes in core temperature and hydrogen

density were greater than the worth of the control system, startup would be extremely difficult, if not impossible.

Chapter VIII delineates some of the catastrophic consequences of introducing reactivities appreciably greater than one dollar. Such an accident is quite conceivable in light of the large reactivity worth of dense hydrogen.

A number of supporting calculations are given in the appendixes. Appendixes A and B discuss the maximum permissible power density in a nuclear rocket from the viewpoint of thermal stress and fluid flow, respectively. In the time dependent fluid flow model employed in Chapter IV, it is assumed that the spatial power distribution is constant. The validity of this assumption is estimated in Appendix C.

All kinetics startup calculations in this thesis are performed using six groups of delayed neutrons. However, a few authors have investigated nuclear rocket startup using a two or three precursor group model. The accuracy of various few group models are examined in Appendix D. Appendix E gives the numerical algorithm which was employed to solve all kinetics problems shown in Chapter VIII and Appendix D.

2.3 Remarks

The general approach outlined in the previous section permits a total separation of the fluid flow calculation (core properties) and the reactivity calculation. In other words, the calculation of the core temperature and hydrogen density distribution during startup is completely independent of the neutronics calculation because the power variation has been specified as a function of time. All hydrogen and temperature feedback can be pictured as being "instantaneously countered" by the external control rods.

Such an attack, of course, completely neglects problems associated with stability, which are certainly important. However, it is thought that the gross nucleonics behavior of large nuclear rockets should be established before detailed stability analysis is performed.

As always, the question of units arises. This problem is particularly acute in the realm of nuclear rockets. Fluid flow and rocket technology is often expressed in English units, whereas the metric system is universally employed in reactor physics. For convenience, the metric system, including both the MKS and CGS units, is used throughout this thesis. A table is given in Appendix F for conversion to the more common English units.

III. NUCLEONICS MODEL

3.1 Introduction

In this chapter, a nucleonics model is set up which computes the reactivity for a given lumped value of hydrogen density and core temperature. Typical slowing down and thermal spectra in nuclear rocket reactors of various sizes are presented. In Chapter V, the reactivity model derived here will be used with the core properties computed in Chapter IV to obtain the reactivity variation during startup.

3.2 General Philosophy of Reactivity Calculation

Plebuch (14) has shown that the spatial distribution of neutrons in a nuclear rocket reactor does not appreciably change with either hydrogen density or core temperature. This fact is also demonstrated in Appendix C for a slab graphite reactor. The energy spectrum, however, does significantly change. This is shown in sections 3.4 and 3.5.

Hence, for survey calculations of the reactivity worth of changes in hydrogen and temperature, it was considered appropriate in the present study to devise a new nucleonics model that treats the neutron energy dependence in detail, but only roughly considers the spatial distribution. Such a model should not be expected to give a precise value of critical mass; yet it should give a good approximation to the reactivity change for a given change in core temperature or hydrogen density.

To this end, an infinite medium model was devised with an approximate leakage term of the form $D(u) B^2 \phi(u)$. For a given core, the buckling, B^2, is obtained from the criticality equation. A schematic diagram of the model is given in Figure 3.2.1. The Goertzel-Selengut Equations (15) were chosen to compute the fast slowing down spectrum. Within the context of isotropic scattering, these equations rigorously treat the slowing down by hydrogen. The Wilkins Equation (16) was chosen to calculate the thermal spectrum and the variation of thermal properties with
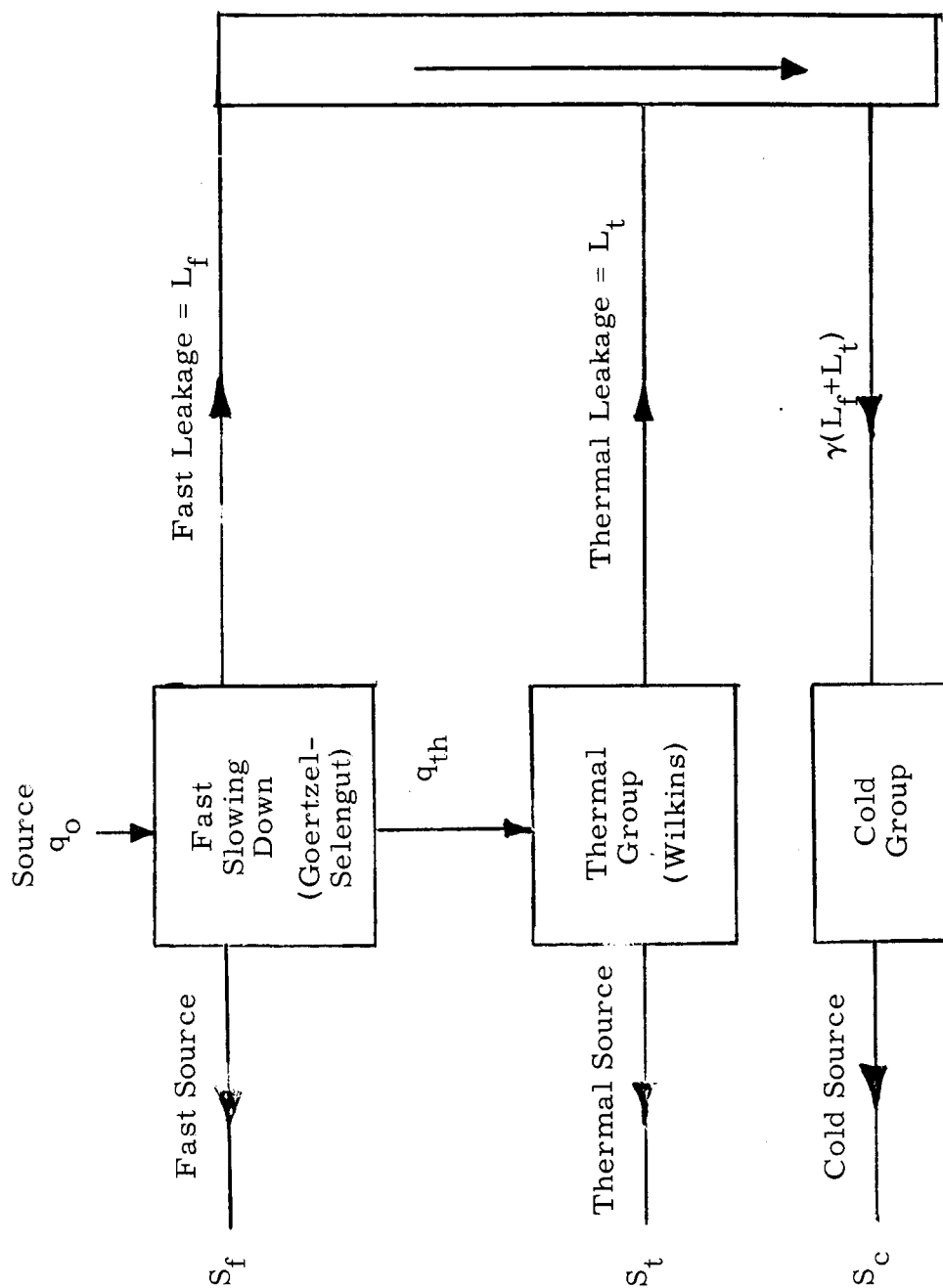
Figure 3.2.1. Reactivity Model

core temperature. Both of these spectra can be computed very rapidly, hence are ideally suited for startup calculations.

The major assumptions made in setting up the model are listed below:

1) The albedo of the reflector is independent of the hydrogen density and temperature in the core.

2) The slowing down spectrum depends on hydrogen density, but not the core temperature.

3) The thermal spectrum depends on the core temperature, but not on the hydrogen density.

4) The Goertzel-Selengut Equations adequately represent the slowing down spectrum.

5) The thermal group can be adequately simulated by the Wilkins Equation.

These assumptions shall be discussed in the following sections, where each segment of the model is analyzed in detail.

3.3 Goertzel-Selengut Equations

In this section, an energy dependent, space independent, modification of the Goertzel-Selengut Equations will be set up and discussed. Typical slowing down spectra for various nuclear rocket cores will be presented in the next section.

The crux of the Goertzel-Selengut method is to divide the neutron slowing down into two components, the slowing down by a heavy moderator (carbon in this case) and the moderation by hydrogen. This is performed in the following manner. Consider an element in lethargy space of width δu at lethargy u. See Figure 3.3.1.
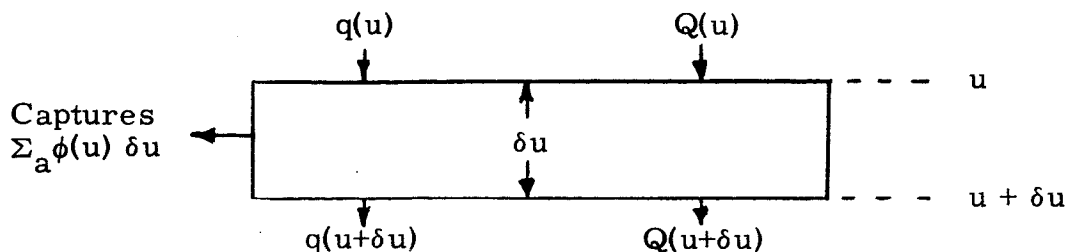
Figure 3.3.1. Lethargy Interval

For the heavy moderator, the continuous slowing down expression

$$q(u) = \xi \Sigma_s^C(u) \phi(u) \tag{3.3.1}$$

is assumed valid, where:

$q(u)$ = slowing down density by graphite moderation only

$\Sigma_s^C(u)$ = macroscopic scattering cross section of carbon

$\phi(u)$ = flux per unit lethargy

ξ = average lethargy change per collision for moderation by carbon.

It should be stressed that the slowing down density appearing in Eq. (3.3.1) denotes the slowing down by graphite only. The moderation rate for hydrogen cannot be expressed in such simple terms because the neutron energy change per collision can be as large as the original neutron energy. Let us define $Q(u)$ as the slowing down density for hydrogen. For isotropic scattering by hydrogen, the probability, $P(u',u)$, that a neutron of lethargy u' will scatter to a lethargy u or greater is ([15])

$$P(u',u) = e^{-(u-u')} \tag{3.3.2}$$

Therefore, the slowing down density, $Q(u)$, can be obtained by merely integrating this scattering kernel times the scattering rate over the appropriate lethargy range, or

$$Q(u) = \int_0^u \Sigma_s^H(u') \phi(u') \, e^{-(u-u')} \, du' \tag{3.3.3}$$

For computational purposes, it is more convenient to recast the above equation into the differential form

$$\frac{dQ}{du} = -Q(u) + \Sigma_s^H(u) \phi(u) \tag{3.3.4}$$

Using Eqs. (3.3.1) and (3.3.4), the energy dependent diffusion equation can now be written in the form

$$D(u)\nabla^2 \phi(u) - \Sigma_a(u) \phi(u) - \frac{\partial q(u)}{\partial u} - \frac{\partial Q(u)}{\partial u} = 0 \tag{3.3.5}$$

or

$$D(u)\nabla^2\phi(u) - \frac{\Sigma_a(u)}{\xi\Sigma_s^C(u)} q(u) - \frac{\partial q(u)}{\partial u} + Q(u) - \frac{\Sigma_s^H(u)}{\xi\Sigma_s^C} q(u) = 0$$

(3.3.6)

Up to this point, we have adhered to the usual formulation of the Goertzel-Selengut Equations. We now assume that the leakage term in Eq. (3.3.6) can be approximated by the expression

$$D(u)\nabla^2\phi(u) = -D(u)B^2\phi(u)$$

(3.3.7)

where B^2 is a constant buckling. Placing Eq. (3.3.7) into Eq. (3.3.6), and using Eq. (3.3.1), we obtain

$$\frac{dq(u)}{du} = Q(u) - \frac{q(u)}{\xi\Sigma_s^C} \left[\Sigma_s^H + DB^2 + \Sigma_a\right]$$

(3.3.8)

This equation, together with Eq. (3.3.4), compose the fast slowing down model used in this thesis.

Before the numerical solution of this set of coupled equations is given, it is perhaps appropriate to discuss the terms, or phenomena, which have been neglected. First, the above fast slowing down model has been assumed to be completely independent of the temperature of the core. This should be a good assumption because the lower energy limit, 1.44 ev, is significantly above the thermal energy range.

Even the temperature effect on the resonance integrals should be very small because we are using pure U-235 as fuel. Note that if one were to use a significant amount of Th-232, or U-238, the resonance integrals could become quite sensitive to temperature changes. Fortunately, for the purpose of this model, these materials are inappropriate for use in rocket reactors because of the weight penalty.

It has also been assumed that there is no inelastic scattering in the slowing down region. For light nuclides, such as carbon, there is practically no inelastic scattering because the excited energy levels are widely separated. Inelastic scattering does occur in heavy elements, like uranium, which have many closely spaced energy levels. Hence, it is conceivable that the combination of fuel, cladding, and

structure could cause appreciable inelastic scattering. However, for lack of a detailed design, we are not considering either cladding or structure. Moreover, it should again be pointed out that we are only considering reactivity changes for changes in hydrogen density and core temperature. A small constant error, therefore, will be of little import.

The most serious approximation made in setting up the slowing down model was to assume that the leakage could be adequately simulated by a constant buckling. It is rather difficult to assess the error involved in this approximation. Perhaps the only valid test of this assumption, and also of the entire model, is to compare the results of the model with more rigorous calculations. This is performed in sections 3.6 and 3.8.

3.4 Numerical Solution of the Goertzel-Selengut Equations

The final coupled set of equations can be written in the differential form

$$
\left\{
\begin{aligned}
\frac{dq}{du} &= Q - q\left[\frac{DB^2 + \Sigma_a + \Sigma_s^H}{\xi\Sigma_s^C}\right] \\
\frac{dQ}{du} &= -Q + \frac{\Sigma_s^H}{\xi\Sigma_s^C}\, q
\end{aligned}
\right\}
\tag{3.4.1}
$$

In order to conveniently solve this set of equations, it is assumed that the fission source distribution can be adequately approximated by a monoenergetic source at 1.05 Mev. This particular source level was chosen because it corresponds to an energy division in the GAM-I cross section set (18). The coupled set (3.4.1) is then numerically integrated from 1.05 Mev to 1.44 ev by a second-order implicit march out technique, the Adams-Moulton Method (17), using 55 energy mesh points. The energy dependent cross sections were taken from General Atomic's GAM-I library tape (18).

Briefly, the Adams-Moulton method can be described in the following manner. Let us, for simplicity, assume that we are solving the

first-order ordinary differential equation

$$\frac{dy}{dx} = f(x, y) \tag{3.4.2}$$

Let j be the space mesh denoting properties at position x_j. The second-order Adams-Moulton algorithm for Eq. (3.4.2) can now be written in the form

$$y_{j+1} = y_j + \frac{h}{12} [5f_{j+1} + 8f_j - f_{j-1}] \tag{3.4.3}$$

where h is the mesh point spacing. Observe that the march out algorithm is implicit in the sense that f_{j+1} on the right hand side of Eq. (3.4.3) cannot be found until y_{j+1} is known. One must iterate, therefore, at each mesh point in order to obtain y_{j+1}.

The Goertzel-Selengut Equations, Eqs. (3.4.1), can be solved in a completely analogous manner. The only added requirement is that at each lethargy mesh point, one must be sure that the two equations are compatible. This just requires a double iteration at each mesh point, instead of the single iteration required for Eq. (3.4.2).

Implicit algorithms, like the one described above, are usually more stable and accurate than corresponding explicit algorithms, but sometimes involve excessive computor time. This, of course, is no problem in our simple case which requires less than one second of IBM-7094 time.

Characteristic slowing down spectra for various nuclear rocket reactors are shown in Figures 3.4.1-3.4.4. In all graphs, the slowing down density, q', refers to the slowing down by both carbon and hydrogen. The source slowing down density was arbitrarily chosen to be 100 for all cases. Figure 3.4.1 demonstrates that essentially no neutrons reach thermal energy in cores with a carbon-to-fuel ratio of 125. In such cores, one might expect the temperature and hydrogen reactivity coefficients to be quite small.

For carbon-to-fuel ratios of 250-500, a few neutrons reach thermal energy. These spectra are shown in Figures 3.4.2 and 3.4.3. Note that changes in hydrogen density have only a small effect on the energy distribution, but it will be shown in section 3.6 that this
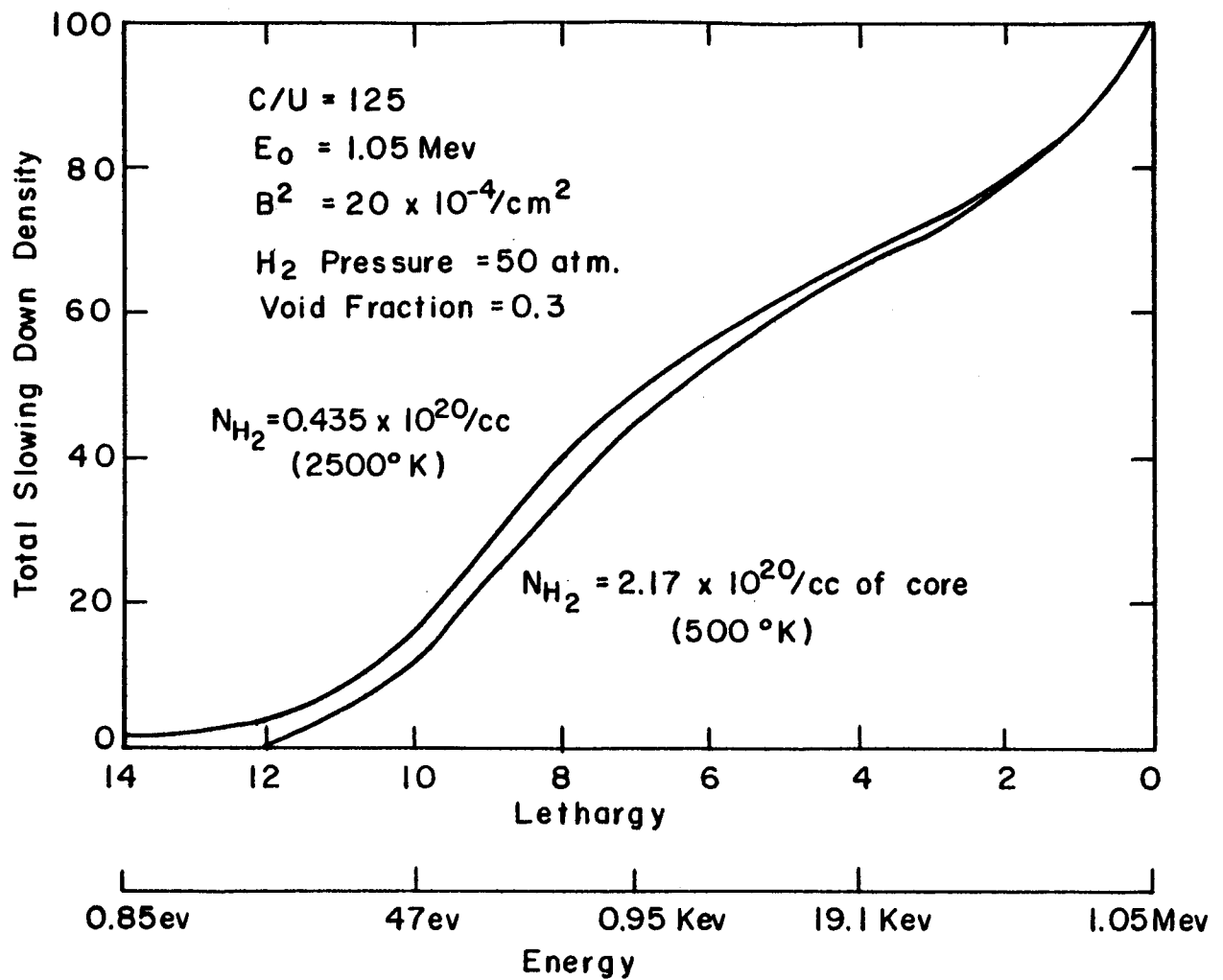
Figure 3.4.1. Effect of Hydrogen on Slowing Down Spectrum For C/U = 125.
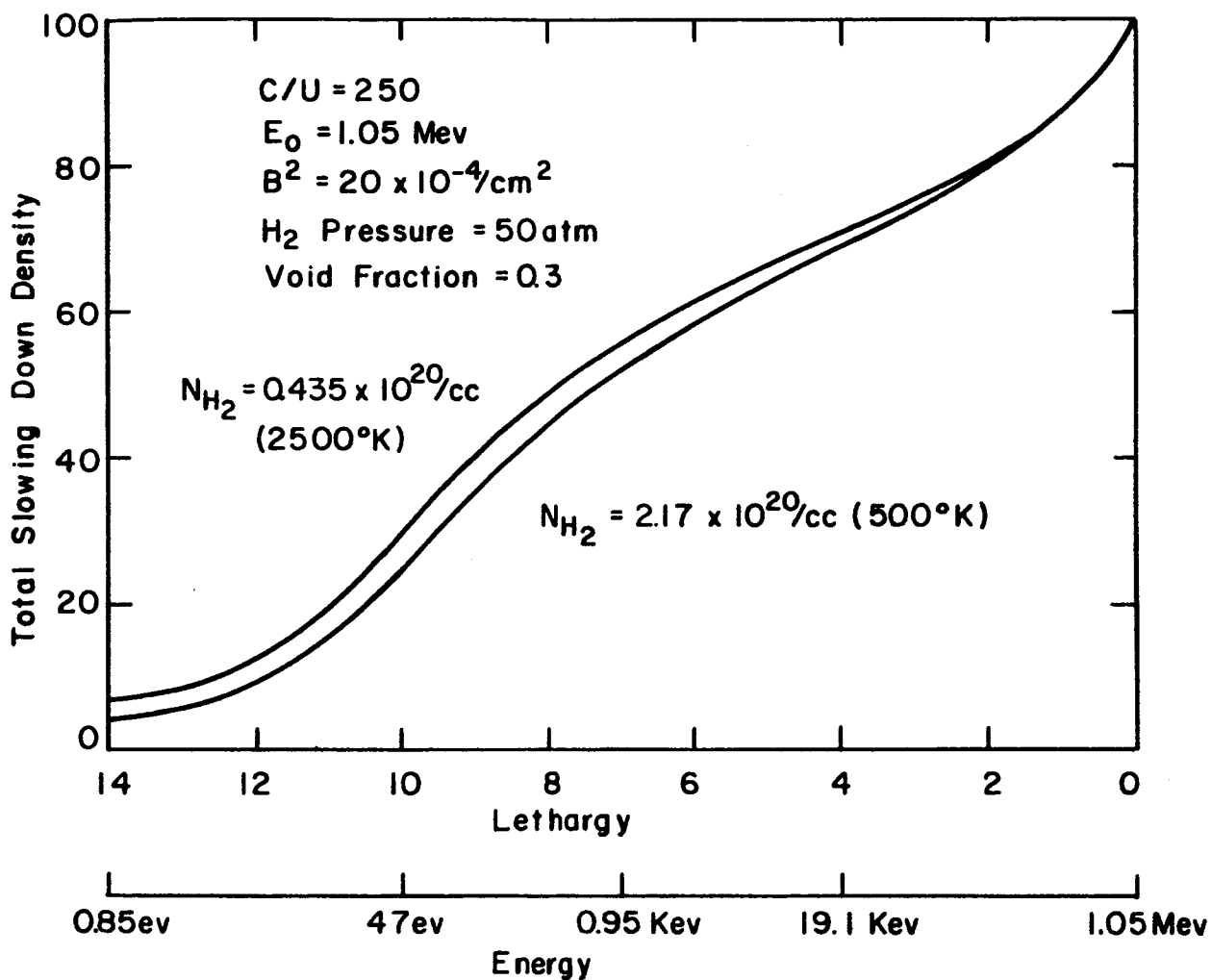
Figure 3.4.2. Effect of Hydrogen on Slowing Down Spectrum
For C/U = 250.
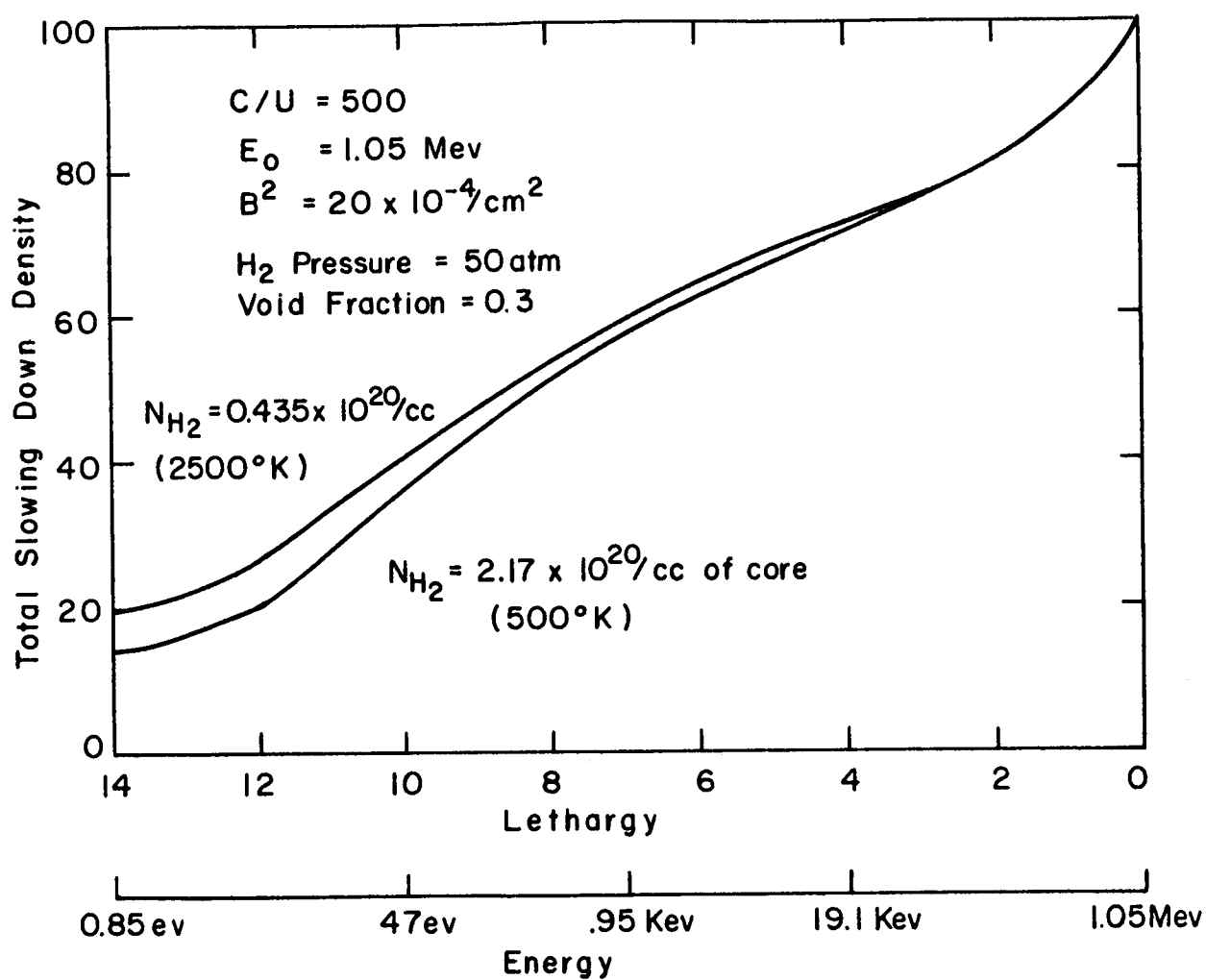
Figure 3.4.3. Effect of Hydrogen on Slowing Down Spectrum
For C/U =500.
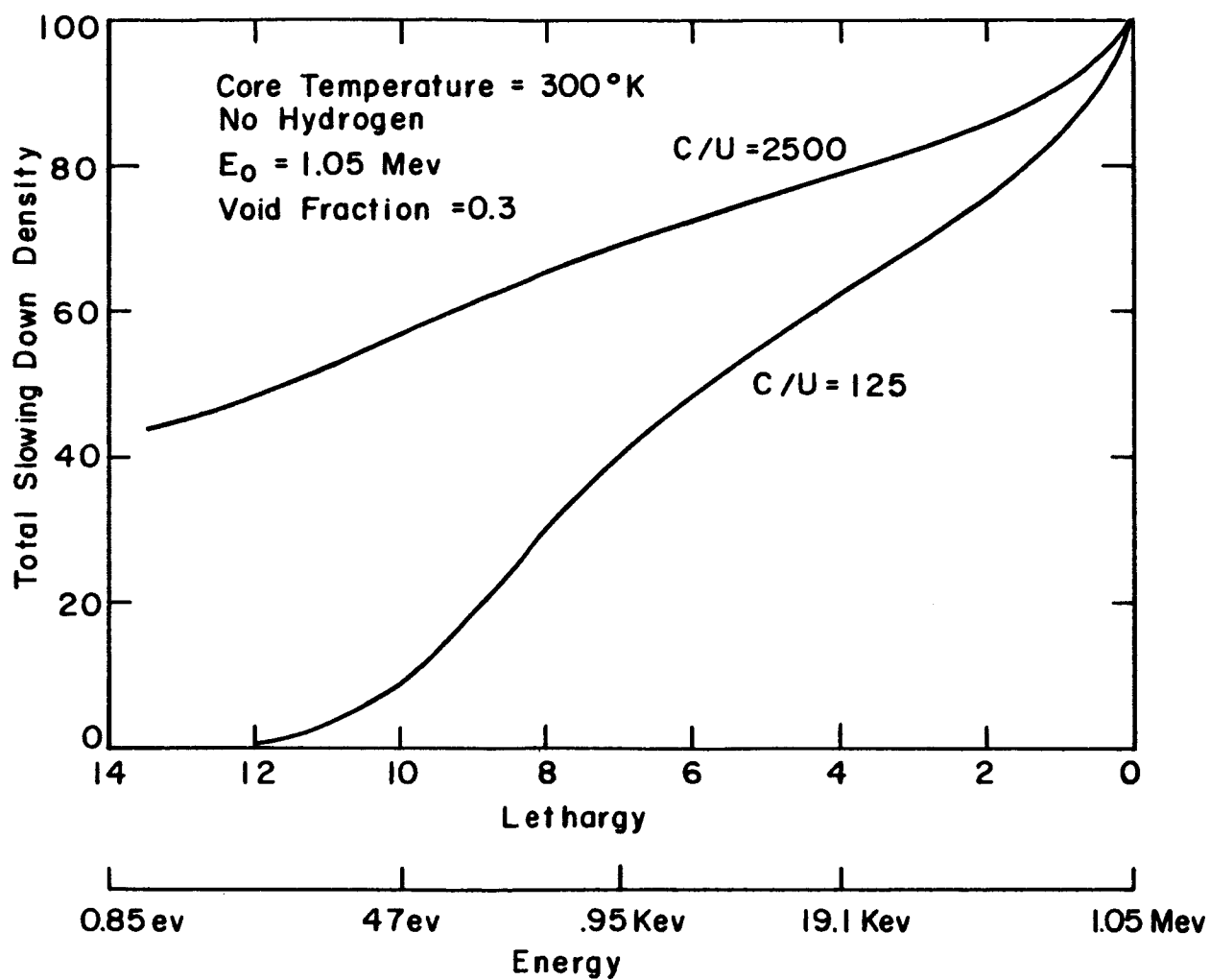
Figure 3.4.4. Slowing Down Spectra in Intermediate and Thermal Reactors.

corresponds to a relatively large reactivity change. Essentially, a small spectrum change can cause a rather large reactivity change because the extra neutrons that reach the thermal region have a high probability of being captured, hence are very valuable.

Figure 3.4.4 demonstrates the immense difference between the slowing down spectra of intermediate and thermal rocket reactors. In a strict sense, however, the "thermal" reactor shown in this figure is not actually thermal since only half the neutrons reach the thermal energy range.

3.5 Thermal Neutrons

For the thermal group, a simple neutron balance yields the relationship

$$D_t \nabla^2 \phi_t - \Sigma_a \phi_t + q_t + Q_t = 0 \tag{3.5.1}$$

where q_t and Q_t denote the slowing down rate into the thermal group by carbon and hydrogen, respectively. We shall now assume, as we did in the fast energy range, that the leakage term can be approximated by the expression

$$D_t \nabla^2 \phi_t = -D_t B^2 \phi_t \tag{3.5.2}$$

where the bucklings in the fast and thermal energy range are assumed to be equal. The thermal flux can now be obtained by substituting Eq. (3.5.2) into Eq. (3.5.1). Therefore,

$$\phi_t = \frac{q_t + Q_t}{\Sigma_a + D_t B^2} \tag{3.5.3}$$

Using the above equation for thermal flux, the thermal leakage rate, L_t, is simply

$$L_f = D_t B^2 \left[\frac{q_t + Q_t}{\Sigma_a + D_t B^2} \right] \tag{3.5.4}$$

Likewise, the fast neutron production rate from thermal fission, S_t, is

$$S_t = \upsilon\Sigma_f\left[\frac{q_t + Q_t}{\Sigma_a + D_t B^2}\right] \qquad (3.5.5)$$

The only unknown parameters in the above equation are the thermal group cross sections. These are obtained by computing the Wilkins Spectrum, and then averaging the cross section over this spectrum. In mathematical form,

$$\bar{\sigma} = \frac{\int v\sigma(v) N(v)\, dv}{\int vN(v)\, dv} \qquad (3.5.6)$$

where $N(v)$ is the solution of the Wilkins Equation

$$\frac{d^2N}{dv^2} + \left(\frac{2v}{\bar{v}} - \frac{1}{v}\right)\frac{dN}{dv} + \left(\frac{4}{\bar{v}^2} - \frac{\Delta}{v\bar{v}}\right)N = 0 \qquad (3.5.7)$$

and:

v = neutron velocity

$N(v)$ = neutron density per unit velocity

$\bar{v} = \sqrt{\dfrac{2kT}{m}}$, T = temperature of medium

$\Delta = \dfrac{4\Sigma_a(kT)}{\xi\Sigma_s}$

Rigorously, the Wilkins Equation is valid only under the following conditions:

1) $1/v$ absorption

2) Mass of moderator much greater than one

3) Moderator follows M-B velocity distribution

4) σ_s = constant

Figure 3.5.1 shows the U-235 absorption cross section as a function of energy. The dotted line portrays a strict $1/v$ cross section variation. Note that over much of the thermal energy range the U-235 absorption cross section has very nearly a $1/v$ behavior; hence the assumption should be permissible.
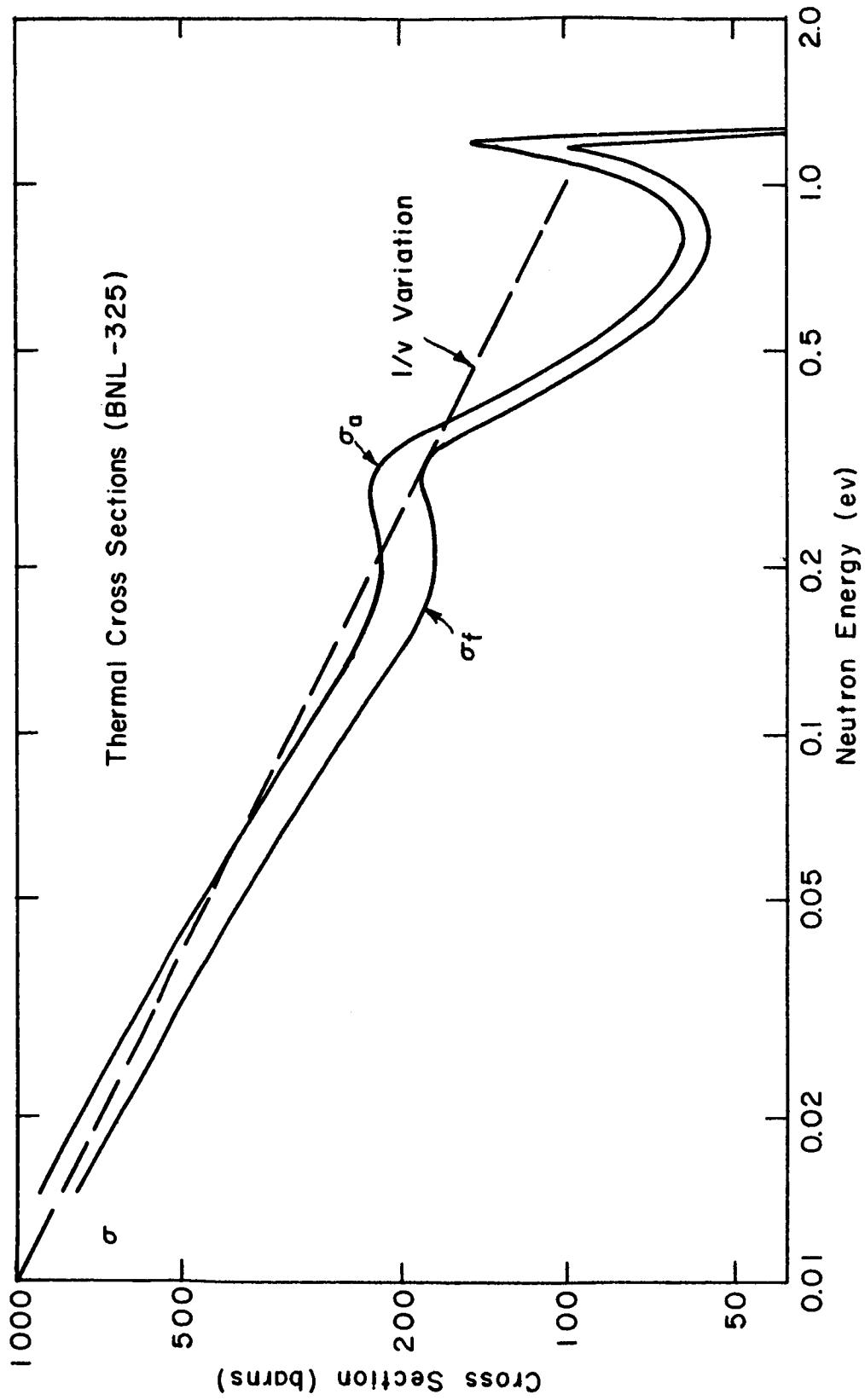
Figure 3.5.1. Absorption and Fission Cross Sections for U-235 (19).

The other three assumptions are a little difficult to justify. In light of the molecular scattering in graphite, it is particularly difficult to justify using a constant scattering cross section. The assumption that the moderator mass is much greater than unity is certainly valid for graphite. However, the effect of hydrogen on the thermal spectrum cannot be included in this model because the scattering mass of hydrogen is very close to unity. For a hydrogen temperature of 1000°K and pressure of 50 atmospheres, the macroscopic scattering cross section is 0.0275 cm^{-1}. Using these values, and a void fraction of 0.3, the cell averaged ratio of the scattering cross section of hydrogen to that of carbon is 0.03. From this, one would expect the effect of hydrogen on the thermal spectrum to be rather small.

It is clear from the above discussion that the Wilkins spectrum involved a number of quite binding assumptions. It has, however, been shown to yield reasonable agreement with more complex crystal scattering models. The interested reader should consult the paper by Nelkin [20]. For this thesis, a more sophisticated and time-consuming thermal model could have been employed. However, it was felt that within the context of a lumped parameter model there was little to be gained by striving for a more detailed thermal distribution. Observe that we only wish to find the average thermal cross sections, which are insensitive to small perturbations in the thermal flux distribution.

3.6 Thermal Spectra and Cross Sections

The Wilkins Equation, Eq. (3.5.7), was solved for various temperatures and carbon-to-fuel ratios by the Adams-Moulton integration algorithm (see section 3.4). Two hundred velocity mesh points were used over the energy range from 0.005 ev to 1.44 ev.

Typical thermal spectra are shown in Figures 3.6.1-3.6.3. The small circles on the graphs denote the velocity positions of the peak of a Maxwell-Boltzmann distribution $\left(v = \sqrt{\frac{2kT}{m}}\right)$. For each figure, the curves are normalized so that the neutron densities are equal at 1.44 ev. Clearly, carbon-to-fuel ratios less than 500 produce extremely hard thermal spectra. Figure 3.6.4 shows a comparison between the Wilkins spectrum and the Maxwell-Boltzmann spectrum for a carbon-to-fuel
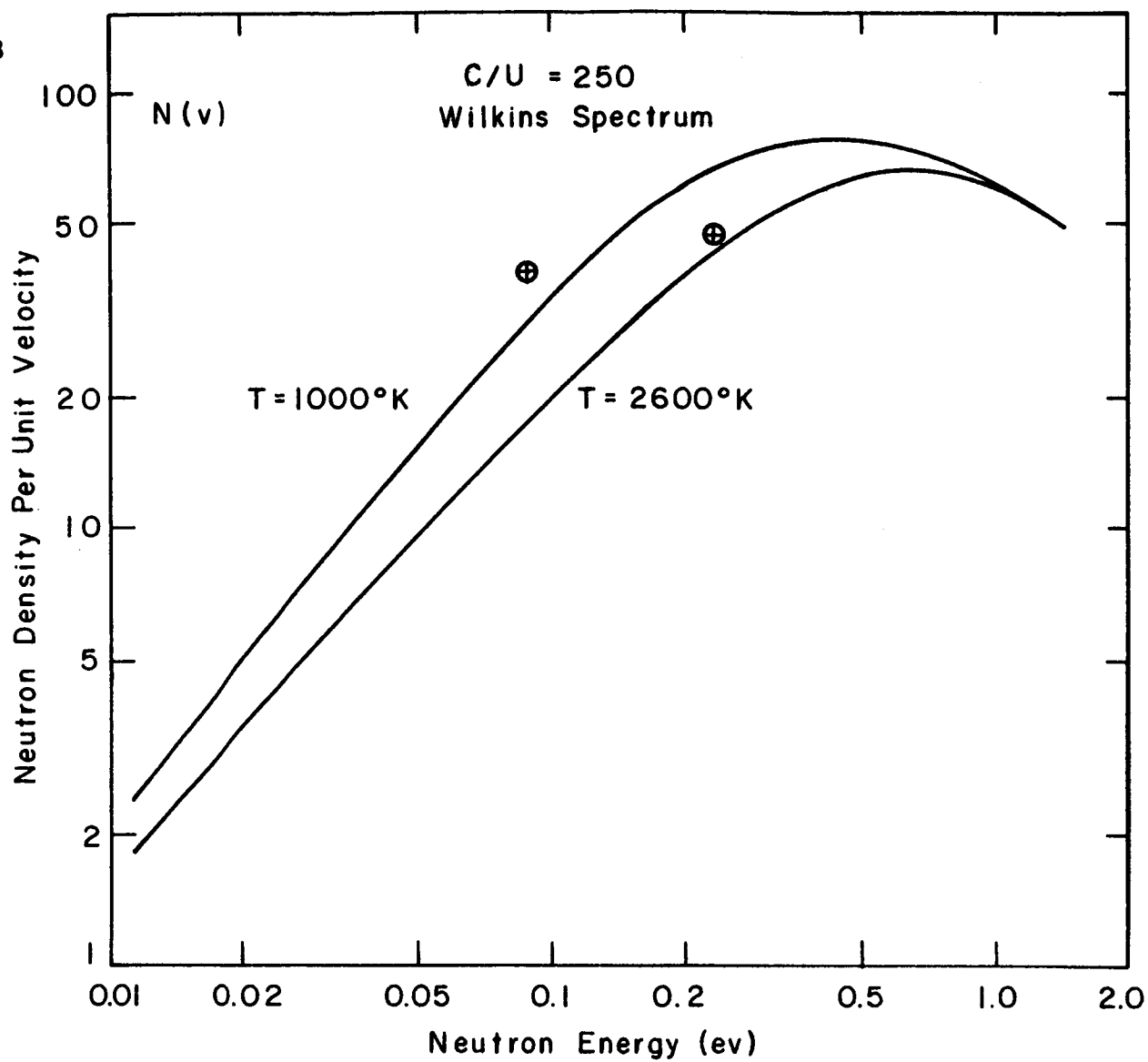
Figure 3.6.1. Thermal Spectra for C/U = 250.
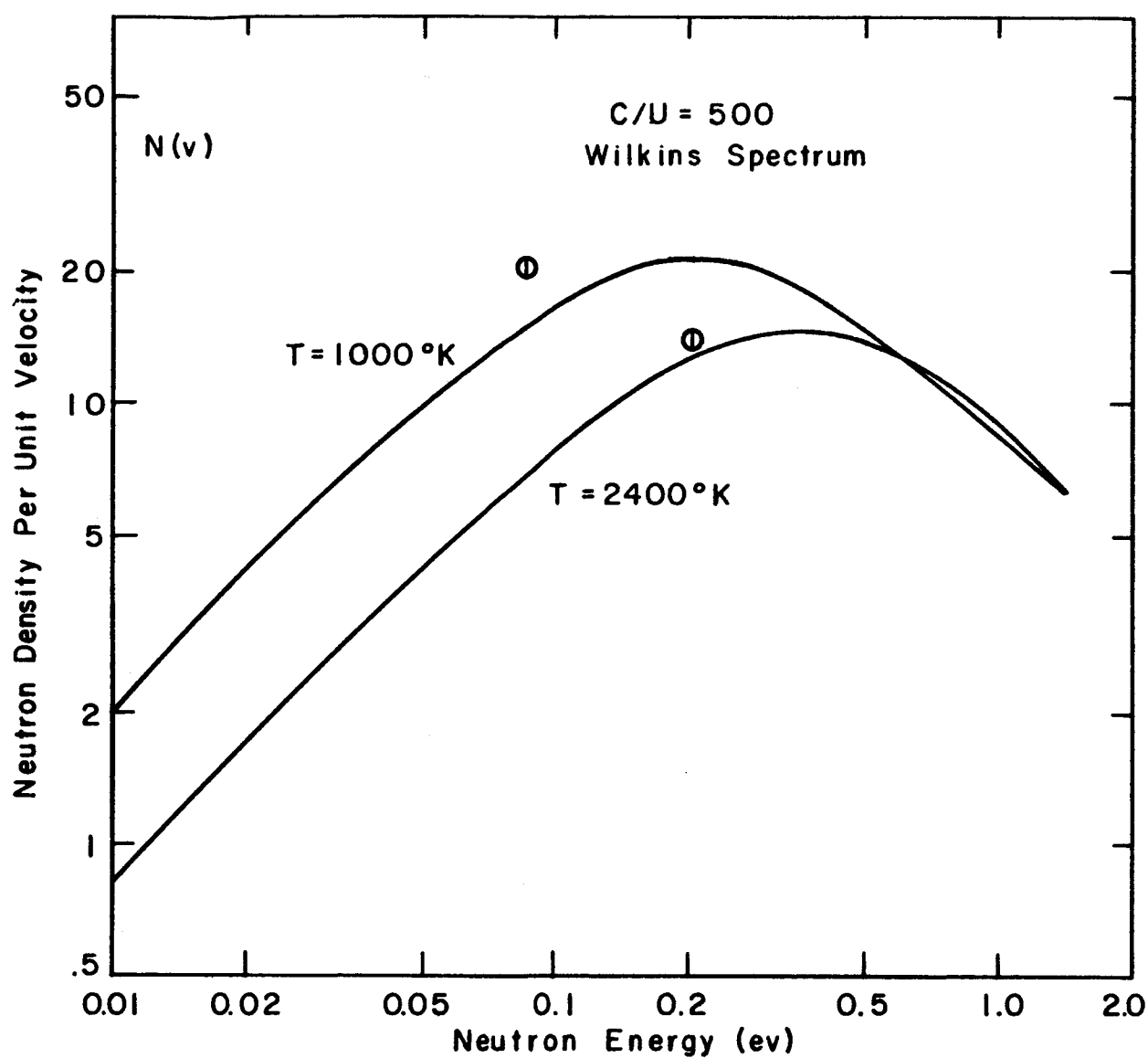
Figure 3. 6. 2. Thermal Spectra for C/U = 500,
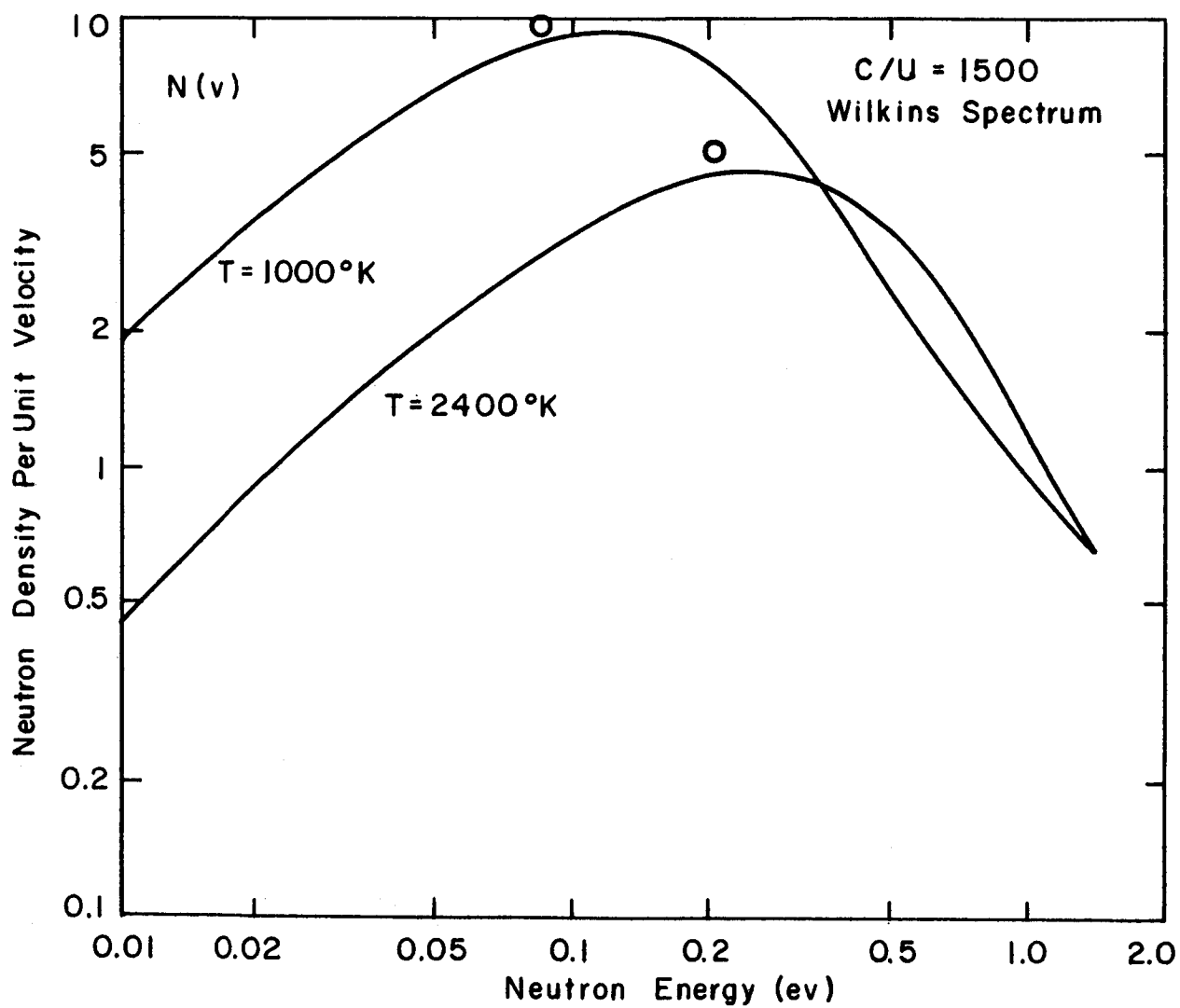
Figure 3.6.3. Thermal Spectra for C/U =1500.
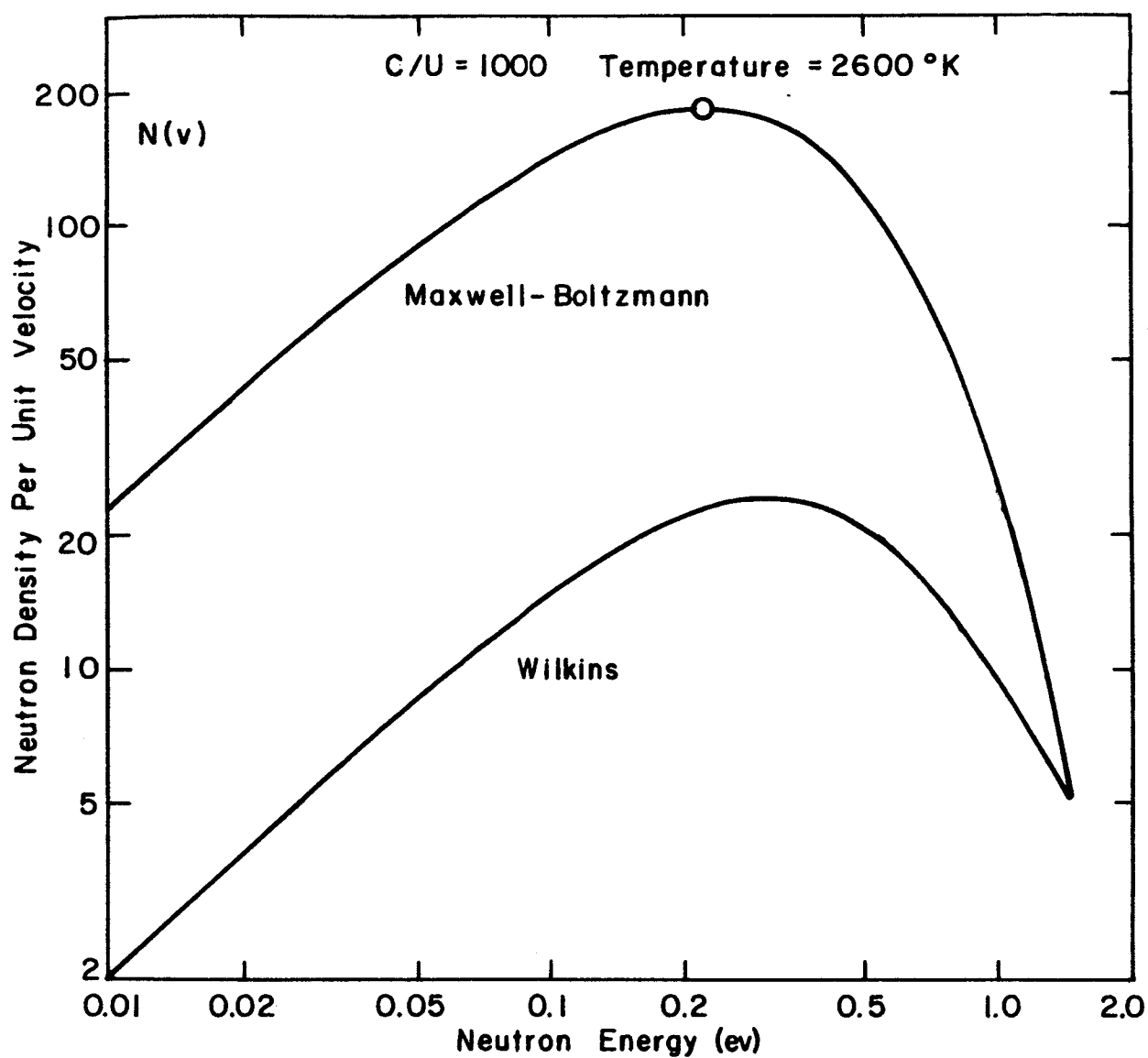
Figure 3.6.4. Comparison of Wilkins and Maxwell - Boltzmann
Spectra for C/U = 1000.

ratio of 1000. Even for this relatively "thermal" reactor, the Wilkins spectrum is obviously much harder than the M-B spectrum.

The average U-235 cross sections were obtained by averaging the cross section curve, Figure 3.5.1, over the appropriate Wilkins distribution. The results are given in Figure 3.6.5. It is obvious that the absorption cross section does not significantly vary with temperature for carbon-to-fuel ratios of less than 250. This results from the fact that most of the neutrons are captured before they reach thermal equilibrium. Note that appreciable cross section variations are found for fuel ratios greater than 1000. It will be demonstrated in section 3.8 that these large cross section variations cause the reactivity to be quite sensitive to temperature changes.

In Figure 3.6.6, eta for U-235 is shown as a function of temperature for various carbon-to-fuel ratios. The variation of eta is small and of little significance per se. However, the shape of the eta versus temperature plot is useful in obtaining a rough feel for the position of the maximum of the neutron capture rate distribution. The eta curve has a dip at 0.3 ev caused by the cross section resonance. Hence an increase of eta with temperature indicates that a predominant number of neutrons are captured over about 0.3 ev. Note that for a carbon-to-fuel ratio of 500, the peak of the neutron spectrum is "over the resonance" for temperatures greater than 700°K. For softer spectra, one must go to higher temperatures to get over the resonance.

3.7 Treatment of Leakage Neutrons

Let us define the fast and thermal leakage rates from the core to be L_f and L_t, respectively. It is now assumed that a fraction, γ, of these leakage neutrons are thermalized in the cold reflector, then scattered back into the core and captured in the core. In other words, the rate, R, that reflected cold neutrons are captured in the core is merely

$$R = \gamma(L_f + L_t) \tag{3.7.1}$$

Furthermore, γ is assumed to be independent of both core temperature and hydrogen density.
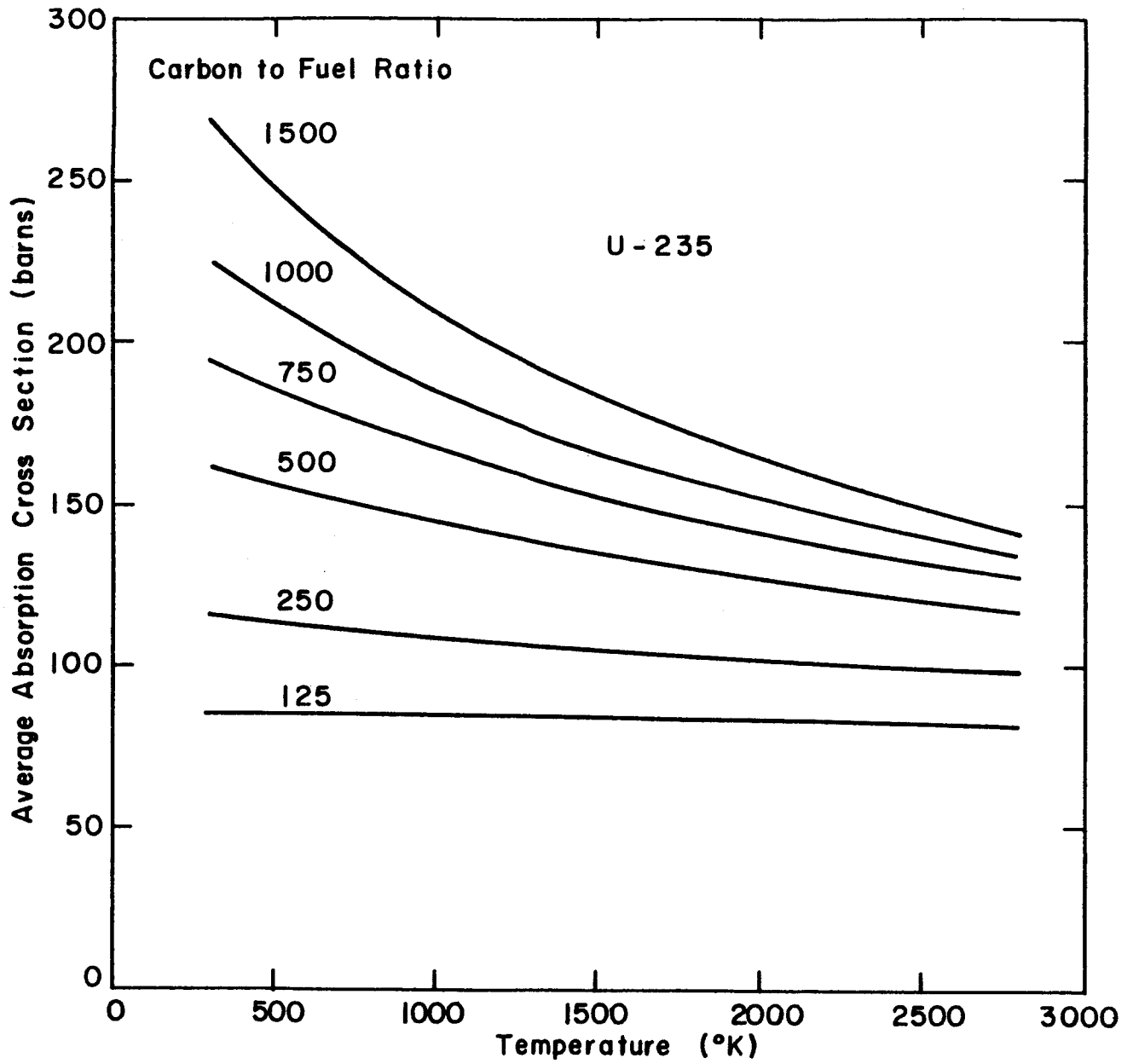
Figure 3.6.5. Average Absorption Cross Sections.

44
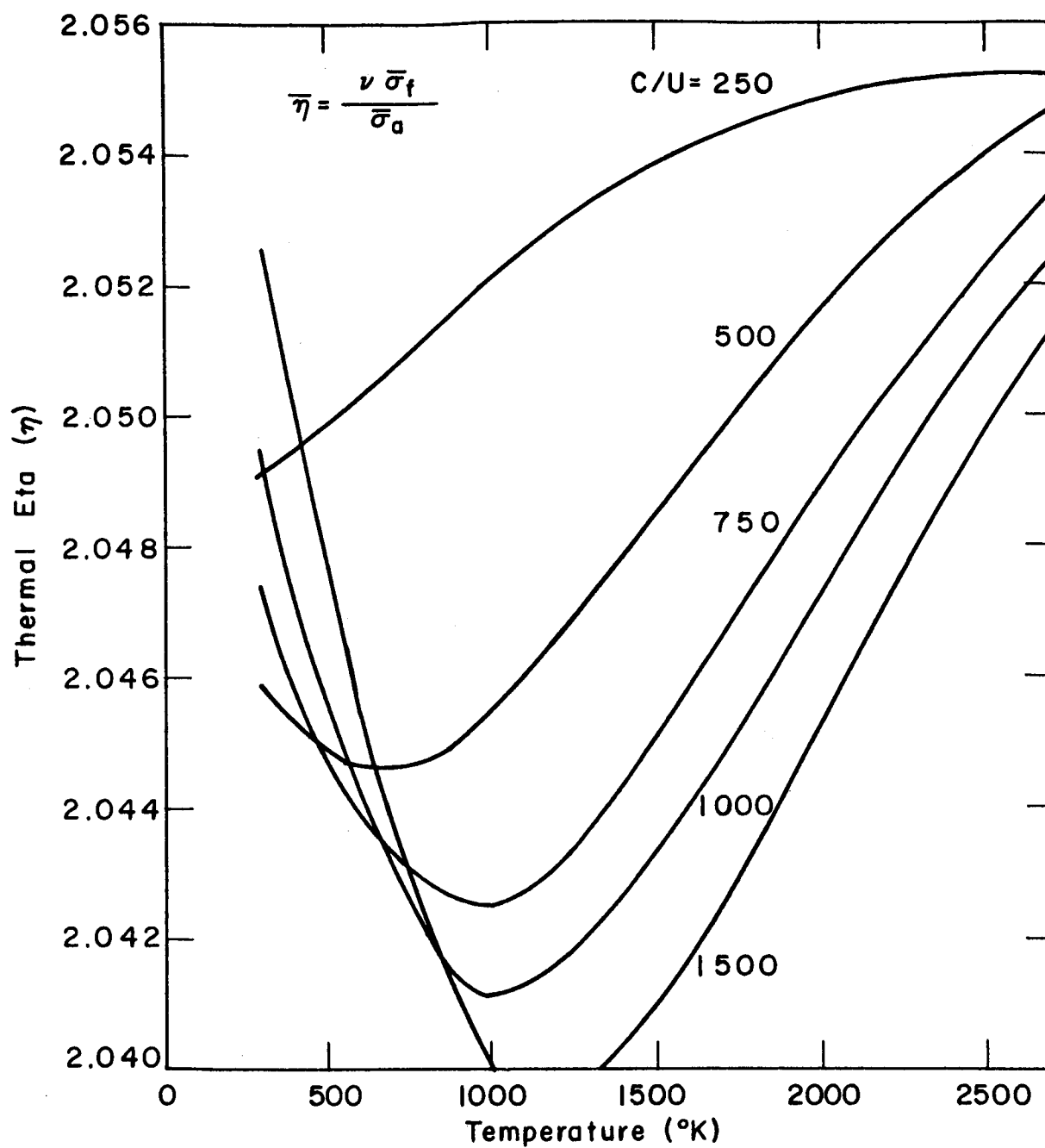
Figure 3.6.6. Average Value of Eta (η) for Thermal Group.

These are, of course, rather broad assumptions. Two questions could now be asked. First, one might ask if these are really valid assumptions for survey type calculations. And, if so, how does one compute γ?

Clearly, if the critical size, or mass, were of importance, the above assumptions would not be appropriate. However, as was previously mentioned, the purpose of this model is to compute reactivity changes, not absolute values. The model works in the same manner as a perturbation calculation. That is to say, the reactivity change caused by a variation in core temperature or hydrogen density, which is computed by taking the difference of two reactivity calculations, may be quite accurate even though each individual reactivity calculation may contain significant error.

Observe that the reflectivity, γ, depends mainly on the properties of the reflector. Hence, for a given reactor, γ is only a second-order function of the hydrogen density in the core and core temperature.

The numerical value for γ was obtained from a two-dimensional calculation with three energy groups (14). For a carbon-to-fuel ratio of 500 and a 10-cm beryllium reflector, γ was found to be 0.12. For simplicity, this value was employed for all calculations.

3.8 Numerical Results: Reactivity Changes for Various Lumped Values of Hydrogen Density and Core Temperature

In this section, the reactivity variations caused by lumped changes in hydrogen density and core temperature will be shown for various carbon-to-fuel ratios. The reactivity will be shown explicitly as a function of both hydrogen and temperature. These results will then be compared with data obtained by other workers. Discussion of the time dependent reactivity variations will be postponed until Chapter V.

From Figure 3.2.1, it is clear that the multiplication factor is simply

$$k = \frac{S_c + S_t + S_f}{q_o} \qquad (3.8.1)$$

For a given carbon-to-fuel ratio, core temperature, and hydrogen density, the only remaining parameter necessary to find k is the buckling, B^2. This is obtained in the following manner. For each carbon-to-fuel ratio, B^2 is computed so that the reactor is exactly critical at 300°K with no hydrogen in the core. As the hydrogen density and core temperature are varied, the buckling is assumed to remain constant.

A graph showing the effect of hydrogen on reactivity for various carbon-to-fuel ratios is given in Figure 3.8.1. The general behavior can be explained as follows. Essentially, hydrogen has a large reactivity value because it is an excellent moderator. The absorption cross section of hydrogen has very little significance in a nuclear rocket. The reactivity coefficient is rather small in an intermediate core (C/U = 125) because an increase of hydrogen merely alters the intermediate spectrum. Essentially no neutrons reach the relatively important thermal range with or without hydrogen.

Epithermal reactors (C/U = 500) have a larger hydrogen coefficient because an increase in hydrogen density significantly changes the number of neutrons reaching the thermal energy level. A clear understanding of these arguments can be obtained by referring back to the plots of slowing down spectra given in section 3.4.

One would expect the hydrogen reactivity coefficient to begin to decrease in magnitude as the carbon-to-fuel ratio is continually increased. Clearly, if the system is already thermal, the addition of hydrogen will be of little consequence. Figure 3.8.1 shows that this is indeed the case, and that the maximum hydrogen worth lies near a carbon-to-fuel ratio of 1500.

It is perhaps worthwhile to point out that the effect of hydrogen is not as severe as it may appear from a quick glance at Figure 3.8.1. In a core with a void fraction of 0.3, the density of H_2 at 50 atm and 1000°K is roughly 1×10^{20} molecules/(cc of core). Hence, the hydrogen worth would only be about four dollars in a core with a carbon-to-fuel ratio of 250. On the other hand, the enormous reactivity increase accompanying an inadvertent insertion of liquid hydrogen with a density of about 50×10^{20} molecules/(cc of core) is all too clear. Reactor behavior during prompt bursts will be discussed in Chapter VIII.
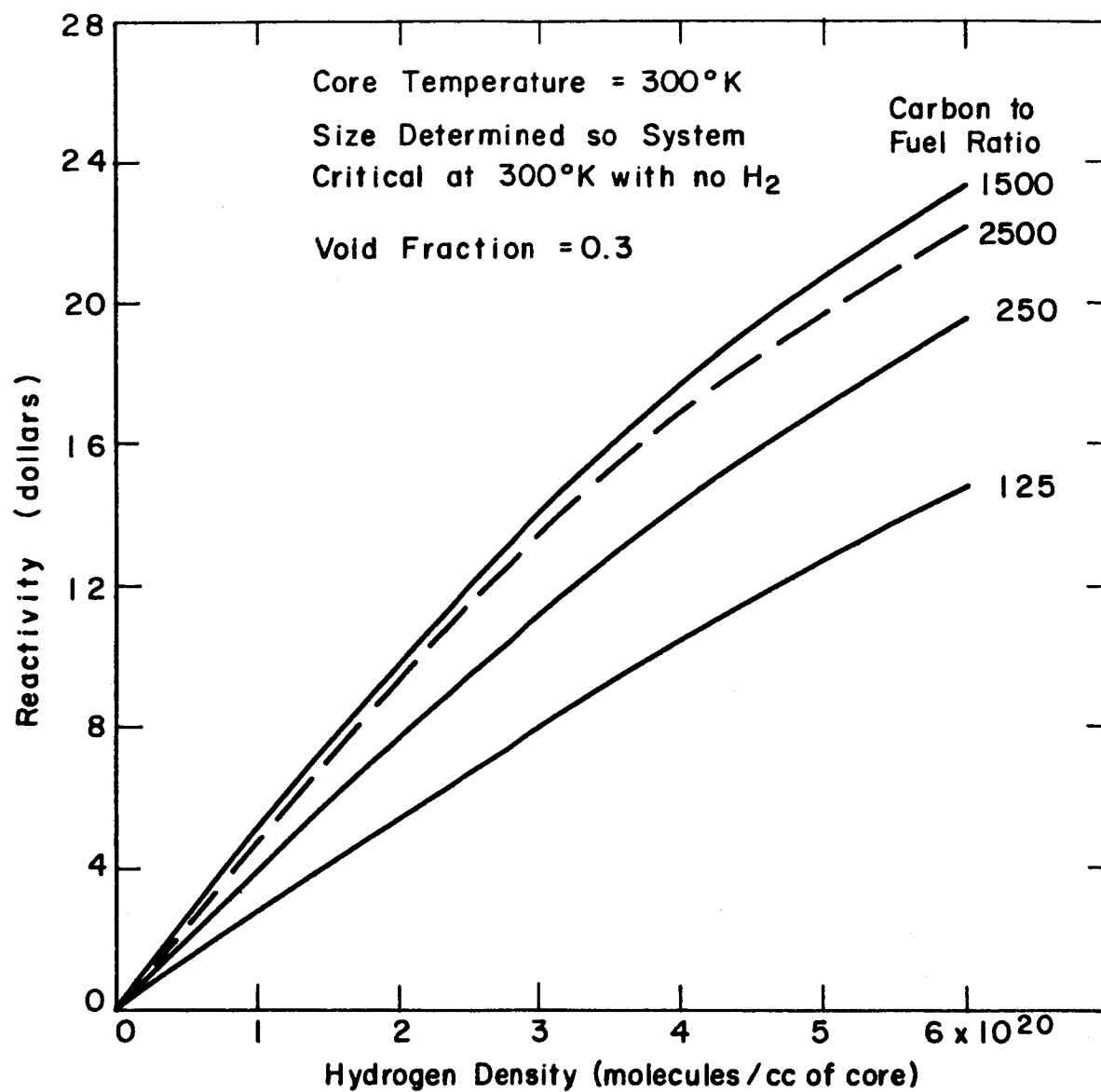
Figure 3.8.1. Effect of Hydrogen on Reactivity.

In passing, note that the reactivity worth of hydrogen is a linear function of hydrogen density over a relatively wide range. This is true for all carbon-to-fuel ratios. Such information might be of use in future stability analysis.

It is rather difficult to check the previous results because there is very little available information on the effect of hydrogen in graphite rocket reactors. A comparison of the data obtained in this thesis with the results found by Plebuch is shown in Table 3.8.1. This table shows the reactivity change, in dollars, caused by an insertion of homogeneous hydrogen at 222°K and 81.5 atm. The core temperature was assumed to be 300°K.

Table 3.8.1. Reactivity Worth of Gaseous Hydrogen
at 222°K and 81.5 atm.

	Thesis	Plebuch (14)
C/U = 500	$27.40	$34.00
C/U = 2500	$26.40	$27.00

For a carbon-to-fuel ratio of 500, the hydrogen reactivity worths differ by about 20%. Because the two models are so totally different, it is difficult to identify the source of error. Briefly, Plebuch's model was a two-dimensional diffusion theory calculation with one fast and two thermal energy groups. He obtained the fast group parameters from the GAM-I code, and the thermal constants from the THERMOS code. In light of the fact that the models agree very well for a carbon-to-fuel ratio of 2500 (thermal core), it is perhaps probable that the source of error lies in the fast energy range.

Figure 3.8.2 shows the effect of core temperature on reactivity for various carbon-to-fuel ratios. Again, for each carbon-to-fuel ratio, the buckling was determined so that the system was exactly critical at 300°K. All calculations were performed for a hydrogen free core.

As the carbon-to-fuel ratio is increased, the magnitude of the temperature coefficient increases because:
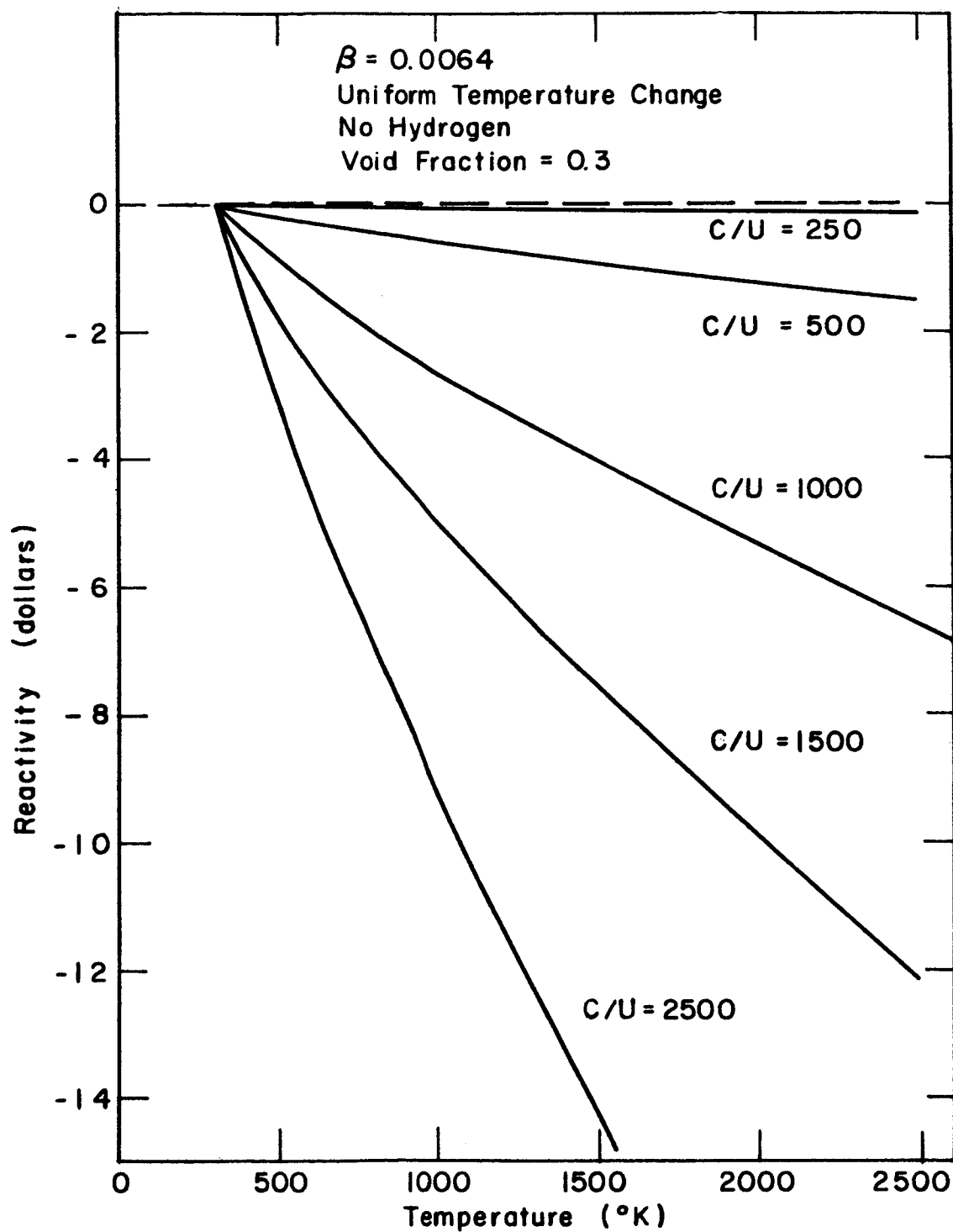
Figure 3.8.2. Effect of Core Temperature on Reactivity.

1) More neutrons reach the thermal energy range.

2) The thermal spectrum becomes softer.

Figure 3.8.2 shows that the reactivity variation can be quite large in thermal rocket reactors, but is of little consequence for carbon-to-fuel ratios less than 500.

It will be demonstrated in Chapter VIII that a large negative temperature coefficient is very desirable from the point of view of prompt burst shutdown. On the other hand, a large negative temperature coefficient requires a sizeable control system to override the negative reactivity change during startup. This point will be discussed in more detail in Chapter V.

The effect of core temperature on reactivity in rocket reactors has also been investigated by C. B. Mills (21) and Plebuch. A comparison of the data obtained in this thesis to their results is shown in Table 3.8.2. It should be pointed out that the carbon-to-fuel ratios employed by Mills do not correspond to those used in this thesis. Hence a direct comparison is impossible. Moreover, all of Mills's calculations, which are performed by either an 18-group S-4 model or a 24-group diffusion model, are for bare spherical assemblies. The leakage characteristics in such assemblies differ significantly from those in reflected cylindrical reactors.

Table 3.8.2. Reactivity Change for a Temperature Shift from 300°K to 2400°K

Thesis		C. B. Mills (21)		Plebuch (14)	
-$ .20	C/U = 250	-$ .60	C/U = 301	—	
-$ 1.50	C/U = 500	-$ 3.10	C/U = 603	—	
-$ 6.30	C/U = 1000	-$10.00	C/U = 1200	—	
-$20.00	C/U = 2500	-$22.00	C/U = 2355	≃$18.50	C/U = 2500

Therefore, it is not surprising that Mills's results differ appreciably from those found in this thesis.

IV. TIME DEPENDENT FLUID FLOW AND HEAT TRANSFER MODEL

4.1 Objective and Procedure

The objective of this chapter is to obtain the space dependent core temperature and hydrogen density during startup. In Chapter V, this information will be used to compute the reactivity variation during startup. It should be made clear from the outset that the fluid flow model developed here is in the spirit of a survey calculation. Because the ultimate goal is to find the reactivity variation during startup, small errors in the core or hydrogen temperature distribution are of no great consequence.

It is assumed that the hydrogen flow rate through the core and the power in the core are specified as a function of time during startup. The power, therefore, is completely decoupled from the flow rate. Such an approach completely neglects stability problems, but is in keeping with the objective of obtaining the effect of variations in core temperature and hydrogen density.

Note that the flow rate and reactor power completely determine the behavior of the system. Knowing these two variables, and the rocket configuration, other variables, such as core temperature, can be computed. Although the mathematical model developed in this chapter can handle almost any time variation of flow rate and power, only linear variations are investigated. The reasons for this choice are discussed at the end of the chapter.

4.2 Outline of Model and Basic Assumptions

The core and hydrogen temperature distributions are calculated as a function of time for a fixed axial power distribution. All radial variations and end effects are neglected. Hydrogen is assumed to follow

the perfect gas law, but variations in heat capacity are considered. In other words, hydrogen is assumed to be a "semi-perfect" gas.

In order to greatly simplify the mathematics, it is also assumed that the hydrogen temperature distribution can be computed as a function of time during startup using a steady-state heat transfer model at each time step. Actually, this assumption is quite good because the residence time of hydrogen in the core is much less than the period for temperature rise. Other approximations will be discussed as they are introduced.

4.3 Heat Transfer Model

At any axial position in the core, a simple energy balance yields the relationship

$$\rho V C_{pf}(T) \frac{dT}{dt}(x, t) = VP(x, t) - Ah(x, t)[T(x, t) - T_b(x, t)]$$

$$(4.3.1)$$

where all symbols are defined in Table 4.3.1. There are numerous approximations involved in the above equation. First, it is assumed that the channel wall temperature at a given axial position is equal to the average temperature in the fuel at the same axial position. Clearly, the average fuel temperature must be higher than the wall temperature. But Appendix A demonstrates that this temperature difference is small for channel sizes and void fractions of interest.

The specific heat of graphite, C_{pf}, is a rather sensitive function of temperature. In this thesis, the heat capacity is approximated by the empirical expression

$$C_{pf} = 2200(1 - e^{-0.00168\ T(°K)}) \text{ joules}/(\text{kg-}°K) \qquad (4.3.2)$$

which was obtained by curve fitting the data presented in reference (22). Figure 4.3.1 shows that Eq. (4.3.2) matches the original data quite well for temperatures above 400°K.

As previously mentioned, the power density in the core, P(x, t), is assumed to be separable in the form

$$P(x, t) = F(t) \cdot P(x) \qquad (4.3.3)$$

Table 4.3.1. Definition of Symbols Used in Fluid Flow Model

A	Heat transfer area/length of core (m)
C_{pf}	Fuel heat capacity (joules/(kg-°K))
C_{pH}	Hydrogen heat capacity (joules/(kg-°K))
D	Diameter of flow channel (m)
h	Heat transfer coefficient (watts/(m^2-°K))
k	Thermal conductivity (watts/(m-°K))
M	Mach Number
P	Power density in fuel (watts/m^3)
T	Temperature of fuel (°K)
T_b	Temperature of hydrogen (°K)
V	Volume of fuel/length of core (m^2)
ω	Flow rate (kg/sec)
ρ	Density of fuel (kg/m^3)
μ	Viscosity of hydrogen (kg/(sec-m))

In reality, of course, the spatial power distribution will vary with time during startup because the core properties change. Appendix C, however, shows that the change in the distribution is very small. The axial power distribution shown in Figure 4.3.2 was used for all fluid flow computations. This distribution was taken directly from a multigroup diffusion theory calculation performed by Plebuch (14). In a strict sense, this axial power distribution is only valid in the radial center of a beryllium reflected reactor with a carbon-to-fuel ratio of 500. However, Plebuch has shown that the axial power distribution is rather insensitive to the carbon-to-fuel ratio. Hence, it should be permissible to use the same distribution for all calculations.

Perhaps the most inaccurate term in Eq. (4.3.1) is the heat transfer coefficient, h, which is computed using the empirical relationship (23)

$$(hD/k)_b = 0.045 \ (Re)_b^{0.8} \ (Pr)_b^{0.4} \ (T_b/T)^{0.55} \ (\ell/D)^{-0.15} \qquad (4.3.4)$$

where the subscript b indicates that the variables are to be evaluated at the bulk temperature. It should be understood that there is nothing
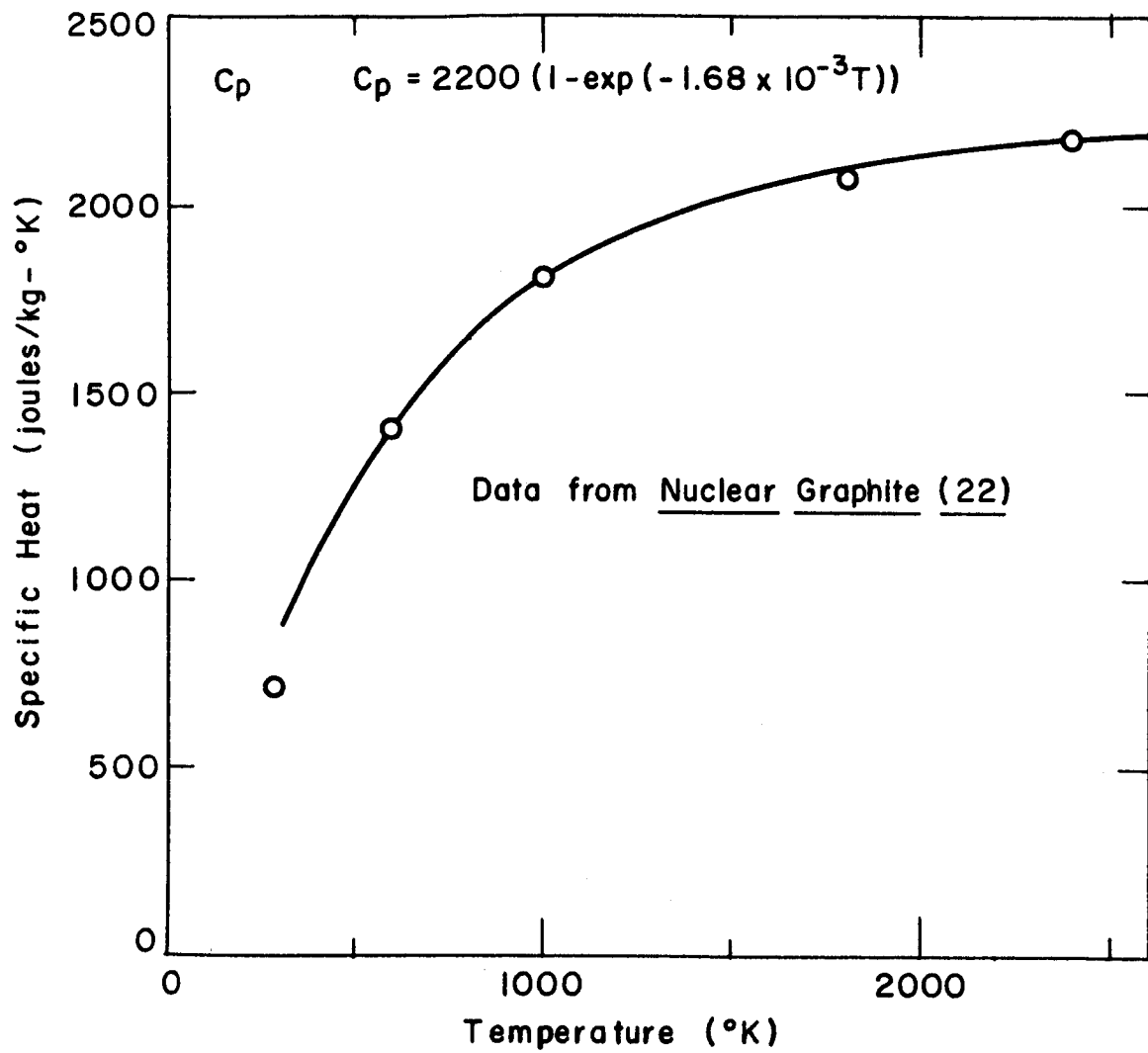
Figure 4.3.1. Specific Heat of Graphite.
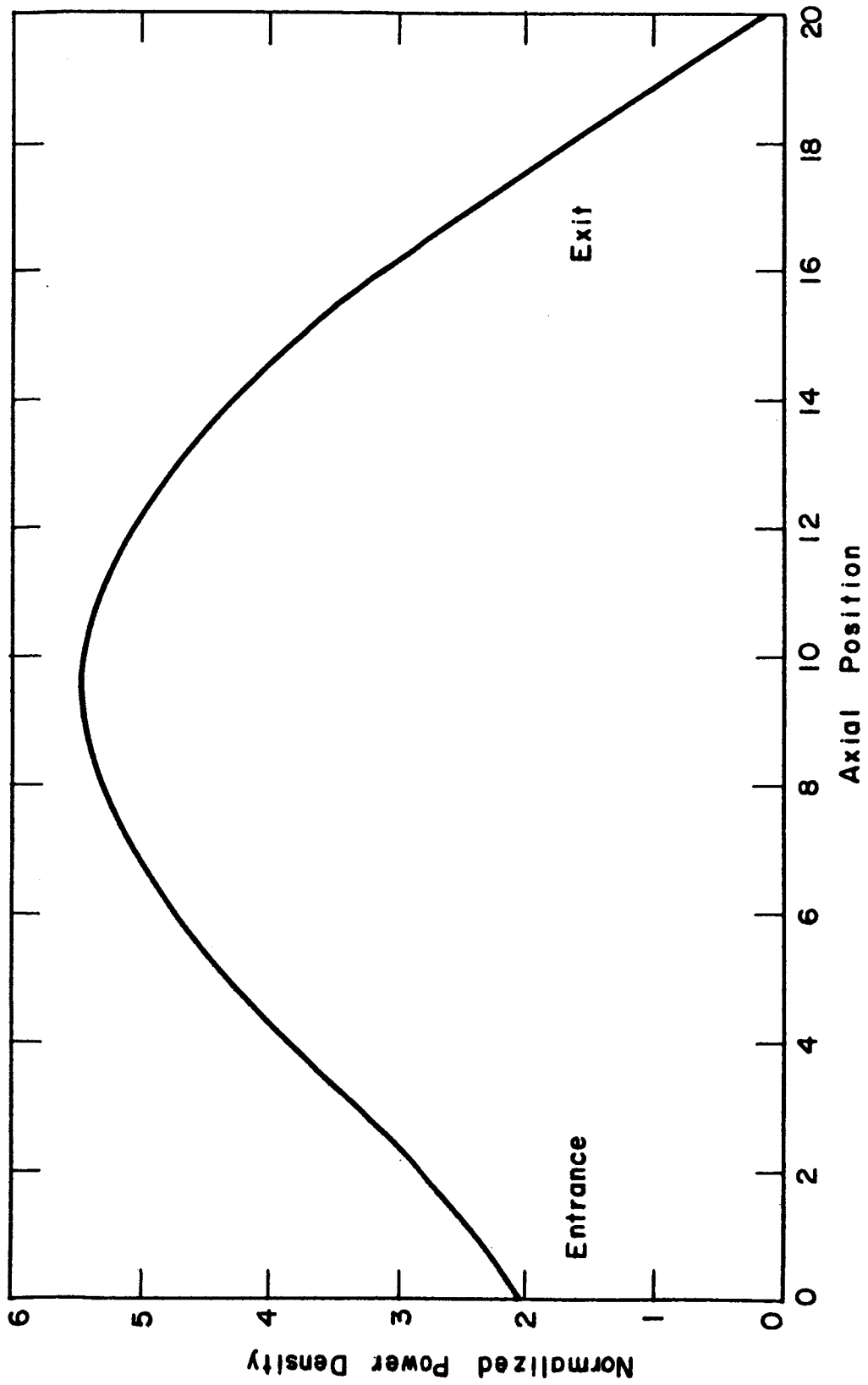
Figure 4.3.2. Axial Power Distribution (14).

sacrosanct about the above relationship, which was taken from the NASA-University Conference report (23). It appears to be at least as good as other similar empirical expressions (24).

In order to evaluate the parameters appearing in Eq. (4.3.4), one needs to know the heat capacity, thermal conductivity, and viscosity of hydrogen. These are approximated by the relations

$$C_p \text{ (joules/(kg-°K))} = 1.41 \times 10^4 + 0.94 \times 10^{-3} T^2 \text{ (°K)}$$

(4.3.5)

$$k \text{ (watts/(m-°K))} = 2.7 \times 10^{-3} T^{0.74} \text{ (°K)} \tag{4.3.6}$$

$$\mu \text{ (kg/(sec-m))} = 3.28 \times 10^{-7} T^{0.6} \text{ (°K)} \tag{4.3.7}$$

which, again, were found by curve fitting the data listed in reference (25). A comparison of the equations given above to the original data is shown in Figures 4.3.3-4.3.5. It can be seen that the agreement is quite good over a relatively broad temperature range.

The hydrogen temperature distribution, which is needed to solve Eq. (4.3.1), is obtained by integrating the differential equation

$$\omega C_{pH} \frac{dT_b}{dx} = hA(T - T_b) \tag{4.3.8}$$

where, for simplicity of notation, the explicit functional dependence of the variables has been omitted. The numerical procedure used to solve Eqs. (4.3.1) and (4.3.8) is discussed in the next section.

Note that all temperature dependence on the Mach Number, M, has been neglected. Rigorously,

$$T_o = \left(1 + \frac{\gamma - 1}{2} M^2\right) T \tag{4.3.9}$$

where T_o is the stagnation temperature. For hydrogen, $\gamma = 1.35$ (26); hence

$$T_o = (1 + 0.175 M^2) T \tag{4.3.10}$$

In the analysis in this chapter, only Mach Numbers less than 0.3 are considered; therefore the difference between the temperature and stagnation temperature is less than 2%. In light of the great reduction in mathematical complexity afforded by the neglect of the Mach Number, the error
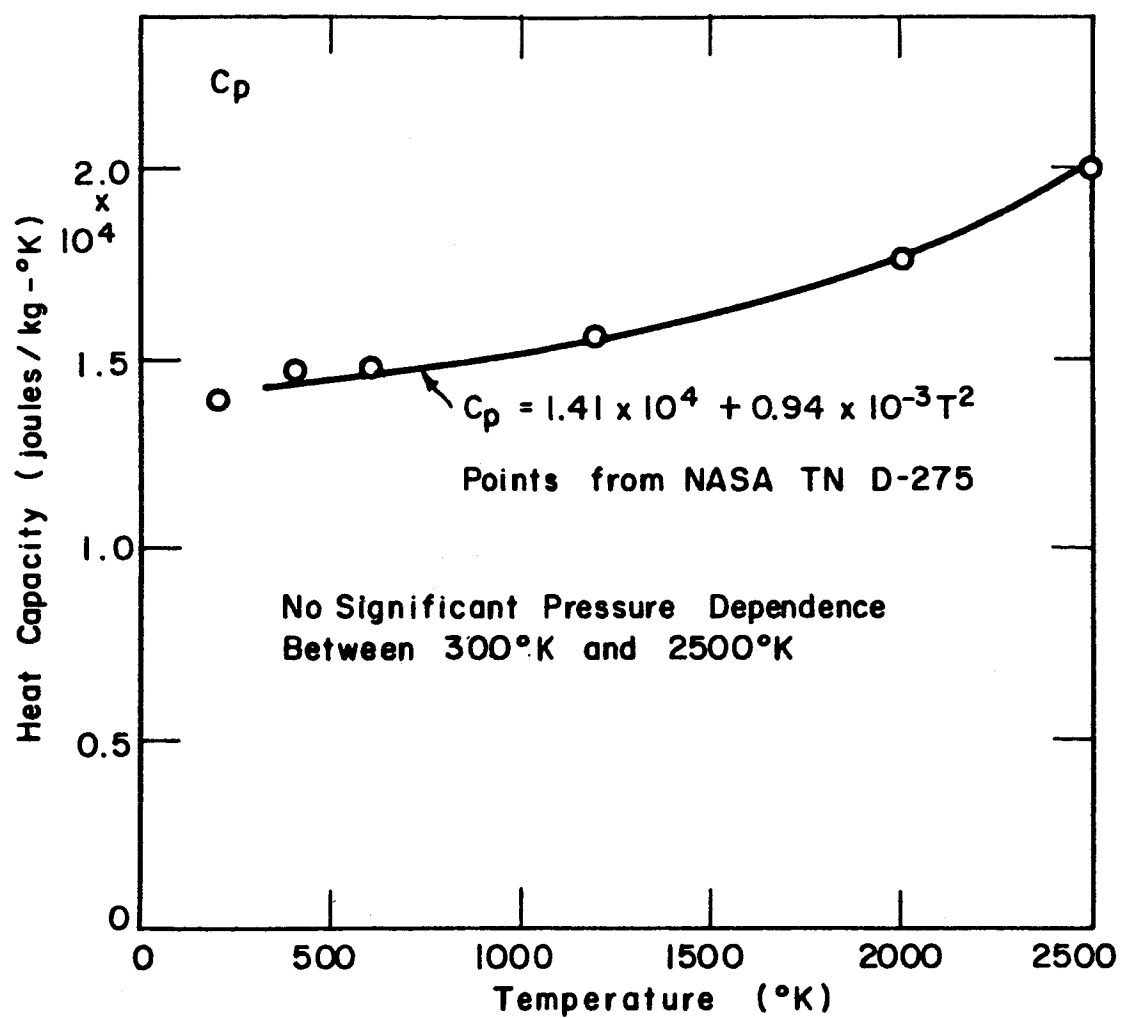
Figure 4. 3. 3. Heat Capacity of Hydrogen Gas.
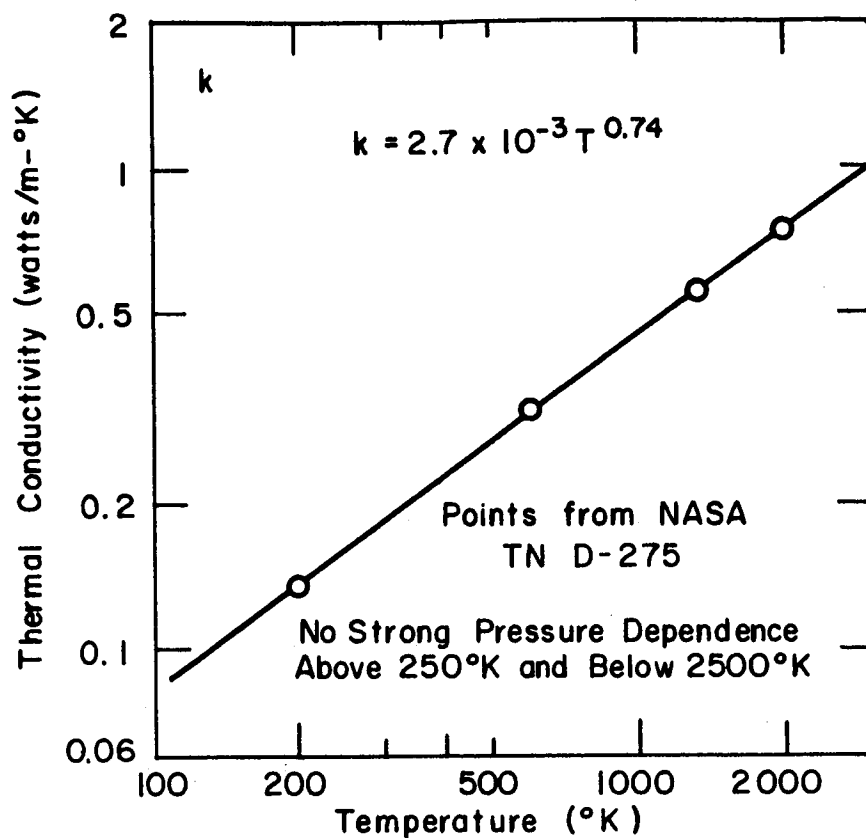
Figure 4.3.4. Thermal Conductivity of Hydrogen
Gas,
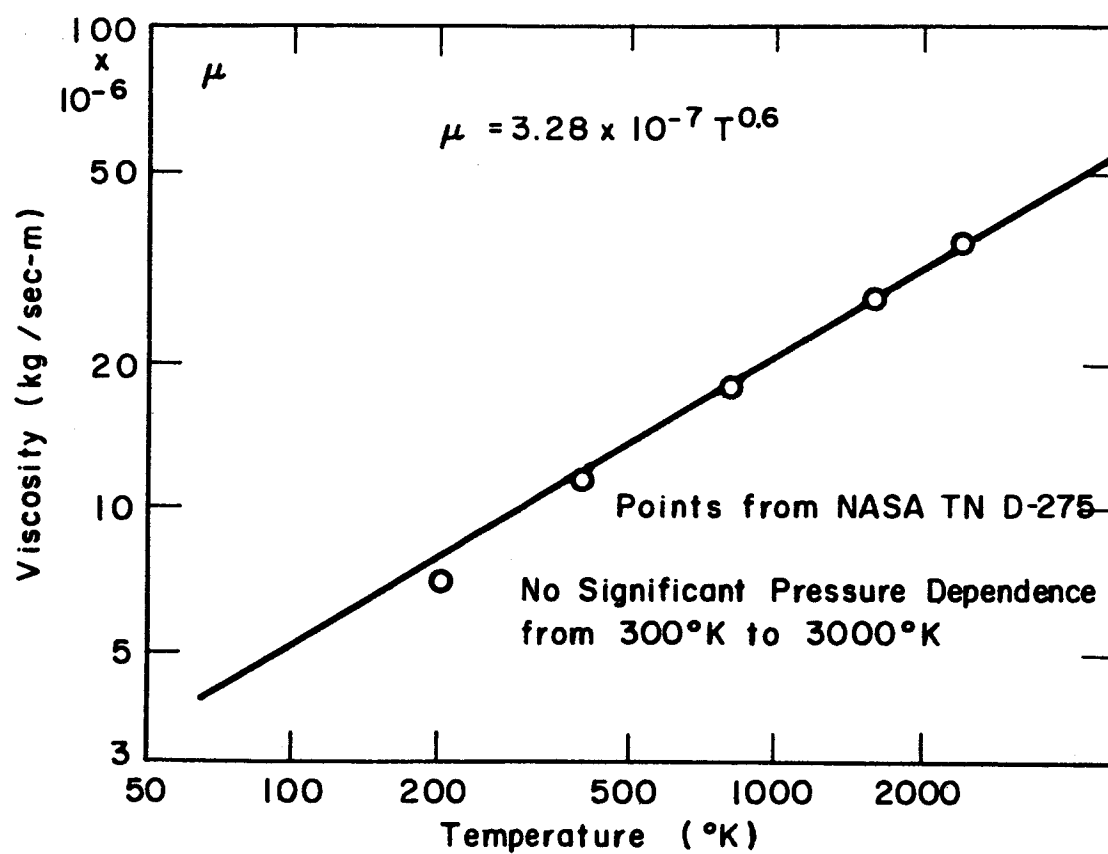
Figure 4.3.5. Viscosity of Hydrogen Gas.

appears rather small. Moreover, there are some very good practical reasons why one might wish to avoid large Mach Numbers. For example, it is shown in Appendix B that the pressure drop across the core increases very rapidly with flow rate for Mach Numbers above about 0.25. Large pressure drops, of course, make the core difficult to support, and therefore complicate design problems.

4.4 Numerical Solution to the Heat Transfer Equations

Eq. (4.3.8) can be rewritten in the form

$$\frac{dT_b}{dx} = \frac{hA}{\omega C_{pH}}(T-T_b) \tag{4.4.1}$$

At any time, t_i, the spatial temperature distribution of hydrogen can be computed using the implicit march out algorithm

$$T_b^{j+1} = T_b^j + \frac{\delta_x Ah^{j+1/2}}{\omega C_{pH}^{j+1/2}}\left[T^{j+1/2}-0.5\left(T_b^j+T_b^{j+1}\right)\right] \tag{4.4.2}$$

where

j = space index

δ_x = space increment (meters)

To avoid confusion, it should be stressed that h^j refers to the heat transfer constant at position j. It does not mean h to the jth power.

For each mesh step from j to $j+1$, the heat transfer coefficient, and thus the gas properties, are evaluated at the average temperature

$$\overline{T}_b^{j+1/2} = 0.5\left(T_b^j+T_b^{j+1}\right) \tag{4.4.3}$$

To obtain the time dependence, we first rewrite the heat flow equation, Eq. (4.3.1), in the differential form

$$\frac{dT}{dt} = \frac{P}{\rho C_{pf}} - \frac{Ah}{\rho V C_{pf}}(T-T_b) \tag{4.4.4}$$

Denoting time by the subscript i ($\delta_t = t_{i+1} - t_i$), Eq. (4.4.4) can be put in the difference form

$$T_{i+1}^{j+1/2} = T_i^{j+1/2} + \frac{\delta t}{\rho(C_{pf})_i^{j+1/2}} \left[\frac{P_{i+1}^{j+1/2} + P_i^{j+1/2}}{2} \right.$$

$$\left. - \frac{Ah_i^{j+1/2}}{2V} \left(\left(T_{i+1}^{j+1/2} + T_i^{j+1/2} \right) - \left(\overline{T}_{b,i+1}^{j+1/2} + \overline{T}_{b,i}^{j+1/2} \right) \right) \right]$$

$$(4.4.5)$$

The fluid flow behavior during startup can now be found by the simultaneous solution of Eqs. (4.4.2) and (4.4.5). Because these equations have a low-order accuracy, small time increments are required. In practice, this restriction is not too severe. Fifty seconds of real time can be simulated in roughly two minutes of IBM-7094 time.

4.5 Fluid Flow Relations in Nozzle

For a given core exit gas temperature and flow rate, the pressure in the core and the thrust are determined by the nozzle. The equations which describe the behavior of a nozzle are discussed in this section. The important assumptions are:

1) Steady-state fluid flow equations can be used to describe the behavior during startup.
2) Perfect gas with constant gas properties
3) Isentropic flow
4) Nozzle throat choked

For the first assumption to be valid, the time lag associated with inertial effects must be much less than the period associated with the time variation of flow rate. For startup times of a few seconds or more, the assumption is quite good.

Because of friction, of course, the isentropic flow equations will give results which differ from experimental results by a few per cent(27). The justification for their use is that they greatly simplify the mathematics.

For startup in outer space, the nozzle will be choked almost from the instant the flow begins. For startup in the atmosphere, the nozzle will choke when the chamber pressure is much greater than the

atmospheric pressure. A typical chamber pressure is 70 atm; hence the nozzle will be choked even far from design pressure. Moreover, it appears that the first generation of nuclear rockets will be used only as upper stages; hence the external pressure will be much less than one atmosphere.
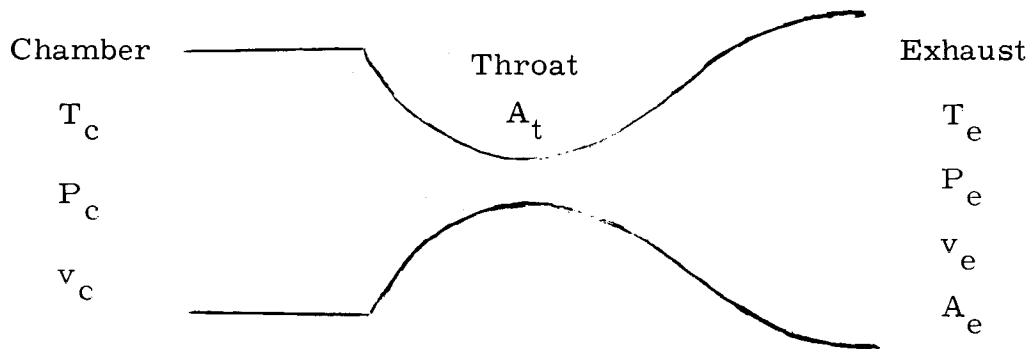
Figure 4.5.1. Schematic Diagram of Nozzle

Let us consider the nozzle shown in Figure 4.5.1, where all symbols are defined in Table 4.5.1. The energy conservation equation on a per unit mass basis has the form

$$v_c^2/2 + h_c + Q = v_e^2/2 + h_e + W \tag{4.5.1}$$

For adiabatic flow with no internal work

$$Q = W = 0 \tag{4.5.2}$$

Making the reasonable assumption that

$$v_c^2 \ll v_e^2 \tag{4.5.3}$$

we find from Eq. (4.5.1) that

$$v_e^2 = 2(h_c - h_e) \tag{4.5.4}$$

or

$$v_e^2 = 2C_p T_c (1 - T_e/T_c) \tag{4.5.5}$$

Table 4.5.1. Symbol Table for Nozzle Equations

A_e area of nozzle exhaust (m^2)

A_t area of nozzle throat (m^2)

C_p heat capacity of hydrogen (joules/(kg-°K))

F thrust (newtons)

g_o acceleration of gravity at sea level (m/sec^2)

h_c enthalpy of hydrogen in chamber (joules/kg)

h_e enthalpy of hydrogen in exhaust (joules/kg)

I specific impulse (sec)

$\underline{M}$ molecular weight of hydrogen

P_c pressure in chamber (n/m^2)

P_e pressure in exhaust (n/m^2)

P_o pressure outside rocket (n/m^2)

P_s stagnation pressure (n/m^2)

P_t pressure in nozzle throat (n/m^2)

Q heat added to system (joules/kg)

R universal gas constant (8.31×10^3 joules/(mole-°K))

T_c temperature of hydrogen in chamber (°K)

T_e temperature of hydrogen in exhaust (°K)

T_s stagnation temperature (°K)

T_t temperature of hydrogen in nozzle throat (°K)

v_c velocity of hydrogen in chamber (m/sec)

v_e velocity of hydrogen in exhaust (m/sec)

v_t velocity of hydrogen in nozzle throat (m/sec)

ω flow rate of hydrogen (kg/sec)

η Carnot efficiency of nozzle

γ gas constant (C_p/C_v)

ρ gas density (kg/m^3)

Using the relationships

$$C_p = \frac{\gamma R}{(\gamma-1)\underline{M}} \qquad (4.5.6)$$

$$\eta = 1 - T_e/T_c \qquad (4.5.7)$$

it follows that

$$v_e = \sqrt{\frac{2\gamma\eta R T_c}{(\gamma-1)\underline{M}}} \qquad (4.5.8)$$

which is the desired expression. The thrust can now be obtained from the equation

$$F = \omega v_e + A_e(P_e - P_o) \qquad (4.5.9)$$

where P_o is the outside pressure.

For efficiencies greater than 0.8, and zero outside pressure, the second term in Eq. (4.5.9) is less than 4% of the total thrust. Therefore, for simplicity, the thrust in this thesis shall be computed using the approximation

$$F = \omega v_e \qquad (4.5.10)$$

A commonly used figure of merit in rocketry is the specific impulse, or thrust per unit "mass," which is defined by the equation

$$I = F/(g_o \cdot \omega) \text{ sec} \qquad (4.5.11)$$

where g_o is the acceleration of gravity at sea level ($g_o = 9.8$ m/sec^2). Combining Eqs. (4.5.10) and 4.5.11), we find that the specific impulse is simply

$$I = v_e/g_o \qquad (4.5.12)$$

A parametric plot of this equation is given in Figure 4.5.2.

Observe, parenthetically, that the constant g_o in Eqs. (4.5.11) and (4.5.12) is completely superfluous. v_e is just as meaningful a figure of merit as I. Moreover, in a strict sense, the thrust per unit flow rate (mass) is v_e, not v_e/g_o. However, specific impulse is so well established that its use is maintained in this thesis.
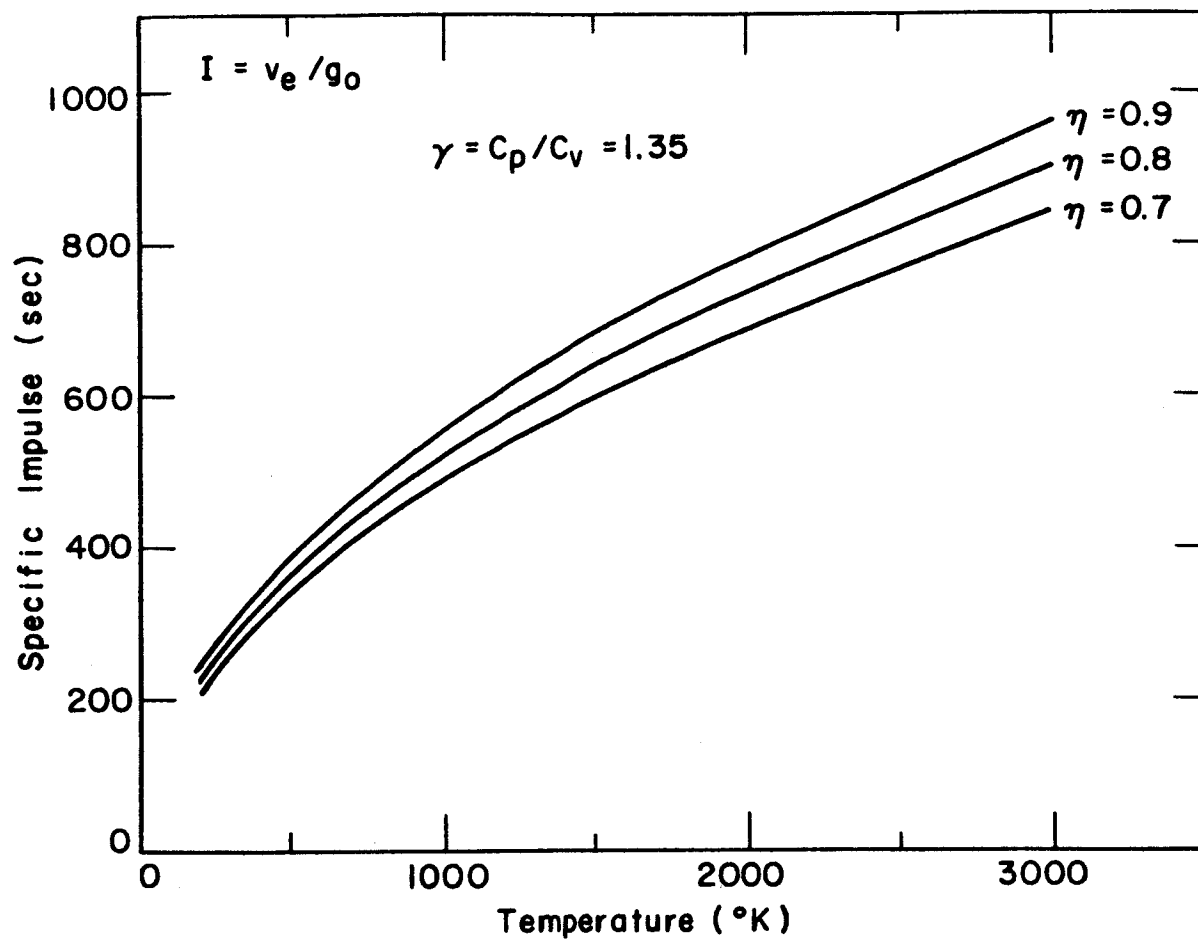
Figure 4.5.2. Specific Impulse for Various Nozzle Efficiencies.

The equation relating the flow rate, ω, to the conditions in the nozzle chamber can be found in the following manner. From a material balance,

$$\frac{\omega}{A_t} = \rho_t v_t \qquad (4.5.13)$$

where the subscript t indicates that the variables are evaluated at the nozzle throat. If we assume that the nozzle throat is choked, the gas velocity in the nozzle is simply

$$v_t = \sqrt{\frac{\gamma R T_t}{\underline{M}}} \qquad (4.5.14)$$

From the perfect gas law

$$\rho_t = \frac{\underline{M} P_t}{R T_t} \qquad (4.5.15)$$

Combining Eqs. (4.5.13)-(4.5.15), the flow rate per unit throat area becomes

$$\frac{\omega}{A_t} = \sqrt{\frac{\gamma \underline{M}}{R}} \frac{P_t}{\sqrt{T_t}} \qquad (4.5.16)$$

For isentropic flow,

$$P_t = P_s \left(\frac{T_t}{T_s}\right)^{\frac{\gamma}{\gamma-1}} \qquad (4.5.17)$$

and

$$T_t = \frac{2}{1+\gamma} T_s$$

where P_s and T_s are the stagnation pressure and temperature, respectively. Placing Eqs. (4.5.17)-(4.5.18) in Eq. (4.5.16), we find that

$$\frac{\omega}{A_t} = \frac{P_s}{\sqrt{T_s}} \left[\frac{\gamma \underline{M}}{R} \left(\frac{2}{\gamma+1}\right)^{\frac{\gamma+1}{\gamma-1}}\right]^{1/2} \qquad (4.5.19)$$

As before, we shall now assume that the Mach Number in the chamber is much less than unity; hence

$$\frac{\omega}{A_t} \cong \frac{P_c}{\sqrt{T_c}} \left[\frac{\gamma M}{R} \left(\frac{2}{\gamma+1} \right)^{\frac{\gamma+1}{\gamma-1}} \right]^{1/2}$$

(4.5.20)

A parametric plot of Eq. (4.5.20) is given in Figure 4.5.3. Notice from Eqs. (4.5.8) and (4.5.20) that the thrust, ωv_e, is directly proportional to the chamber pressure, and independent of temperature.

4.6 Results

Using the model described in the previous sections, a number of "startups" were investigated for a linear increase in power and flow rate. All cases studied were found to have the same general characteristics. The reactivity calculations to be shown in Chapter V are based on a 25-second startup; hence the fluid flow behavior for this particular case will be described in this section. All pertinent information concerning this run is given in Table 4.6.1. These particular constants were chosen to reflect typical numerical values listed in the literature.

Table 4.6.1. Data for Startup Calculation

Ramp time	=	25 seconds
Core length	=	1.25 meters
Void fraction	=	0.3
Channel diameter	=	0.25 cm
Entrance hydrogen temperature	=	140°K
Final exit gas temperature	=	2660°K
Final flow rate	=	240 Kg/sec-m^2 flow area
Final exit pressure	=	70 atm

Figure 4.6.1 shows the spatial core temperature variation during startup for an initial core temperature of 300°K. Observe that during the initial seconds of startup the temperature distribution has the same
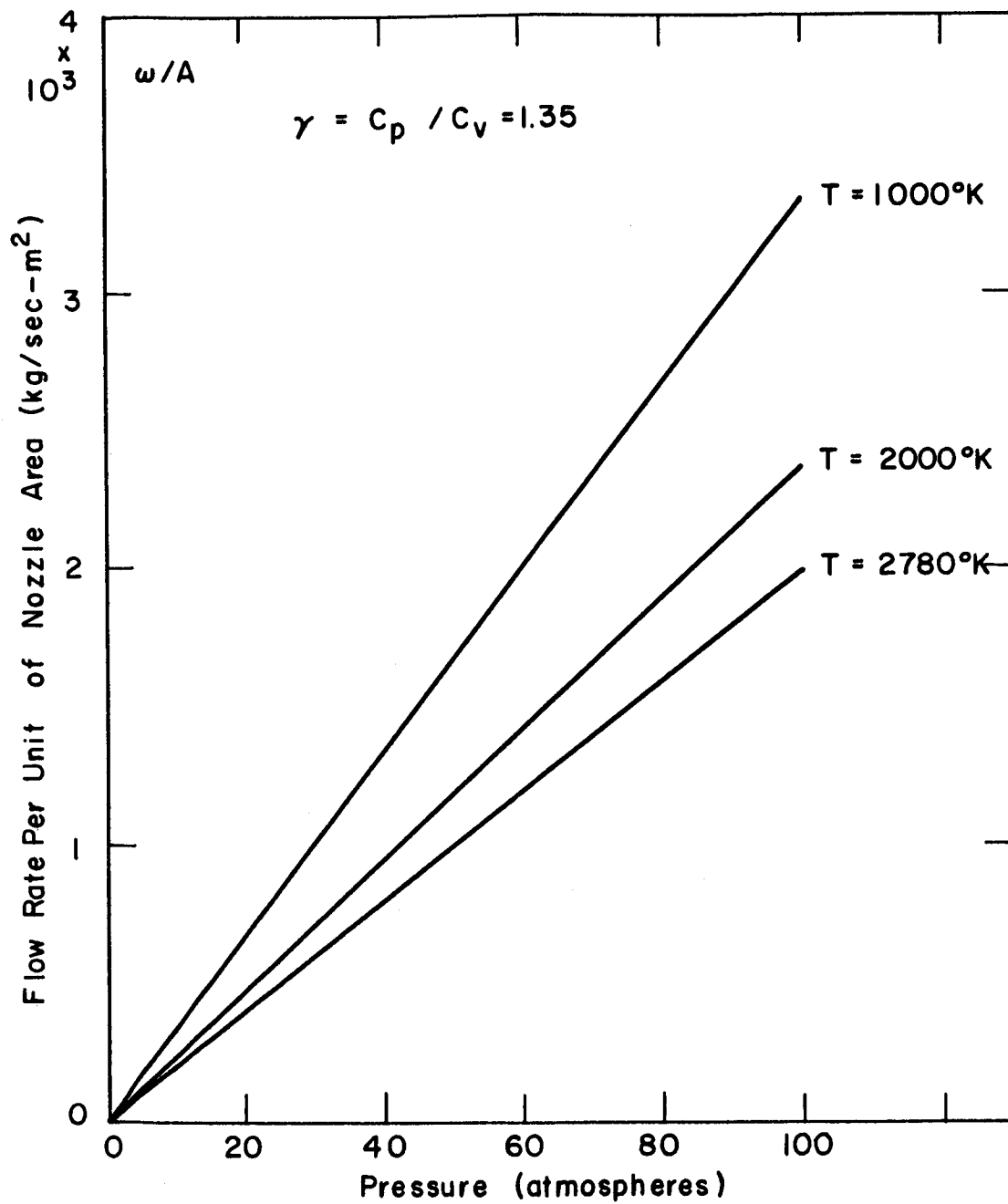
Figure 4.5.3. Hydrogen Flow Rate for Various Chamber Conditions.
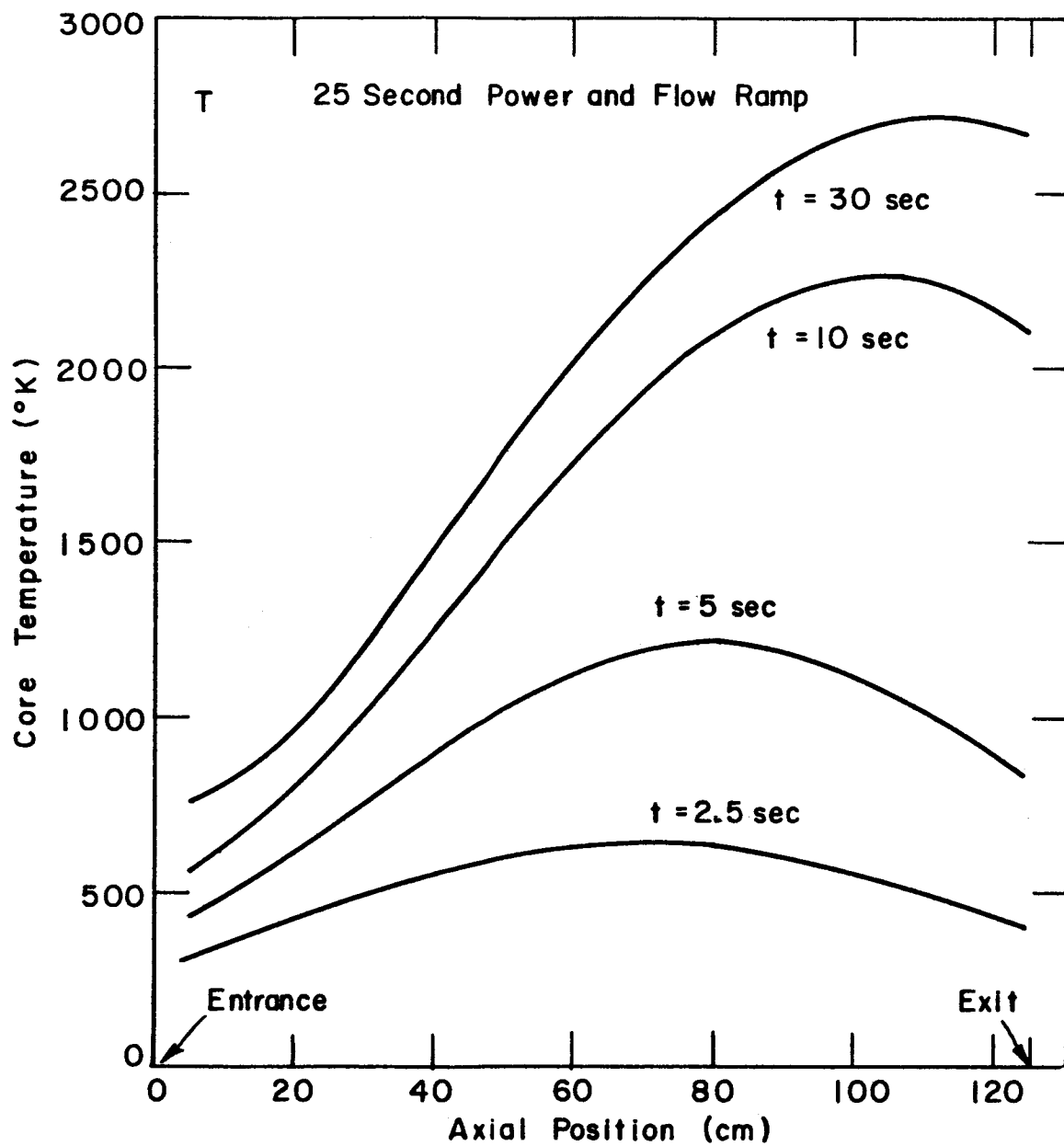
Figure 4.6.1. Core Temperature Distribution During Startup.

general shape as the power distribution, and that the peak of the distribution slowly moves down the core. Note also that the temperature is close to its final value after just 10 seconds, which indicates that the thermal inertia of the core is very small. That is to say, the core temperature quickly follows any change in power or flow rate.

The hydrogen temperature distribution is shown in Figure 4.6.2 for a constant entrance temperature of 140°K. Again, it is clear that the hydrogen temperature is relatively close to its final value after just 10 seconds of operation. From the viewpoint of specific impulse, shown in Figure 4.6.3, a rapid hydrogen temperature rise is highly desirable. On the other hand, a rapid core temperature rise may induce intolerable stress, and perhaps aggravate control problems.

Using the time dependent nozzle chamber pressure, shown in Figure 4.6.4, the hydrogen density distribution in the core can be easily computed. The distribution is shown in Figure 4.6.5. As one would expect, most of the hydrogen in the core is found in the cold entrance region.

The thrust, which is computed by the approximate expression

$$F = \omega v_e \qquad\qquad (4.6.1)$$

is shown in Figure 4.6.6. As previously mentioned, the thrust can be seen to have the same time dependence as the chamber pressure.

4.7 Discussion of Other Possible Startup Schemes

Numerous other linear startups, ranging from 10 seconds to 60 seconds, were investigated. To a fairly good approximation, the results differed only by the time scale factor.

Flow and power increases which differ from a linear time variation, will, naturally, cause the reactor thermal behavior to depart from the results presented in the previous section. Various authors have considered other than linear flow and power increases (28). However, the departures from a linear power and flow variation were not large. Moreover, the resulting core and hydrogen temperatures had approximately the same time profile as those shown in the previous section. It is therefore concluded that the simple linear power and flow

rate rise gives an adequate description of the reactor thermal behavior during startup. This should be all the more true considering that our ultimate interest is in the magnitude of the reactivity variation during startup, not the precise flow behavior.
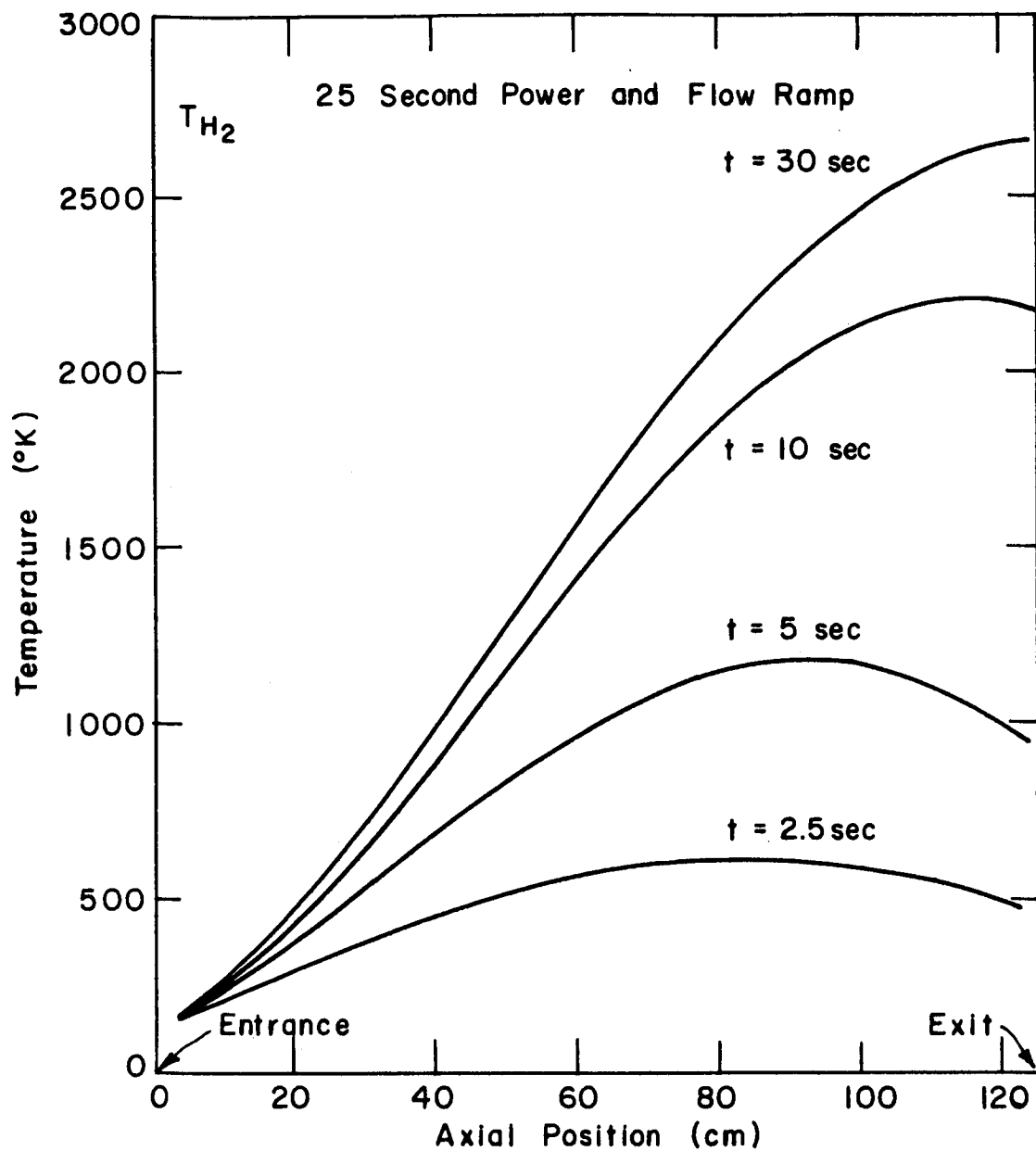
Figure 4.6.2. Hydrogen Temperature Distribution During Startup.
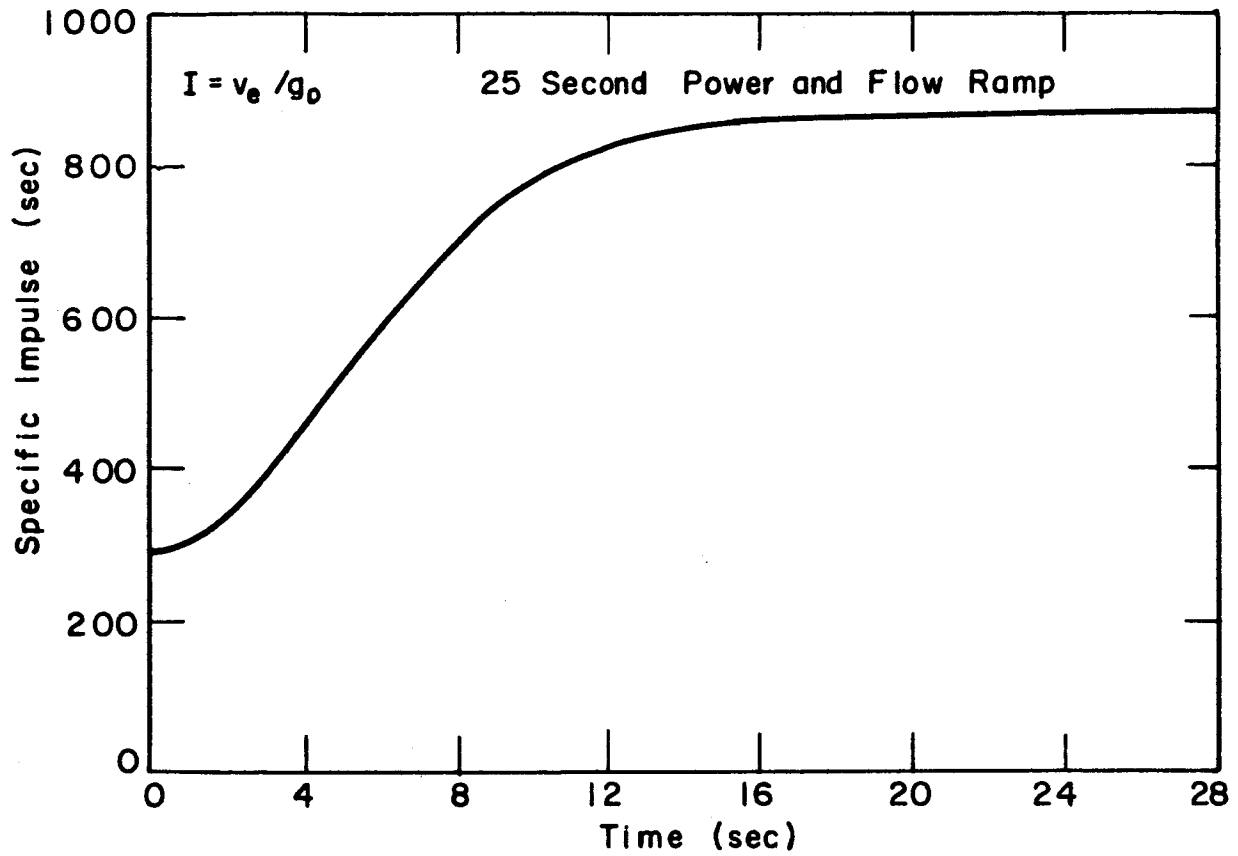
Figure 4.6.3. Specific Impulse During Startup.
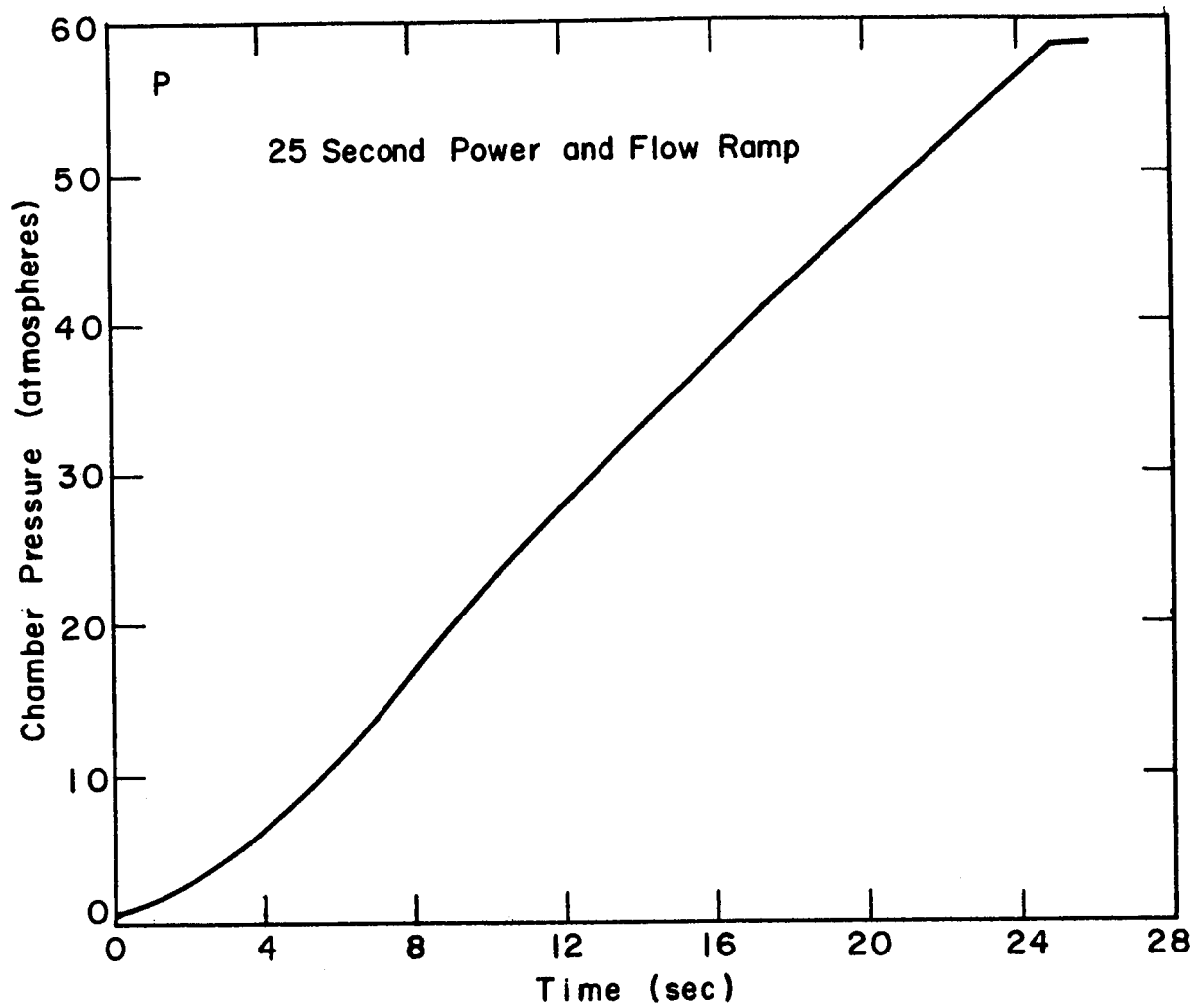
Figure 4.6.4. Nozzle Chamber Pressure During Startup.
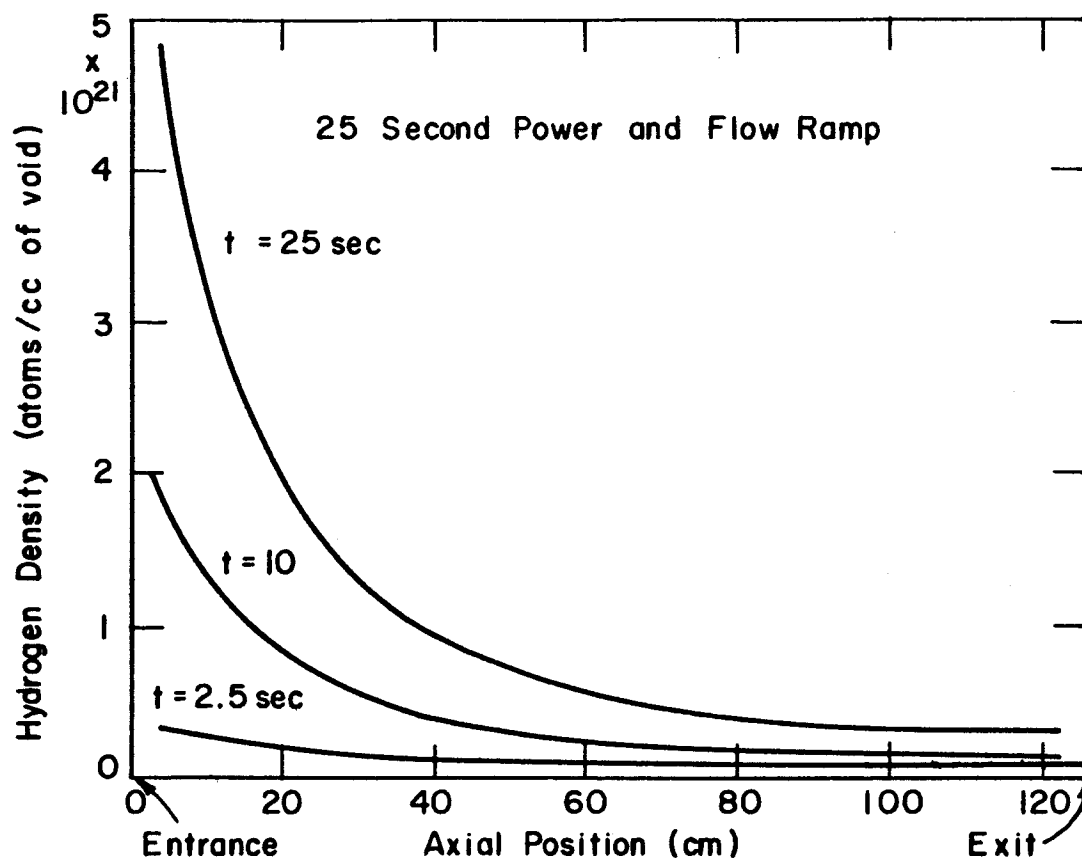
Figure 4.6.5. Hydrogen Density Distribution During Startup.
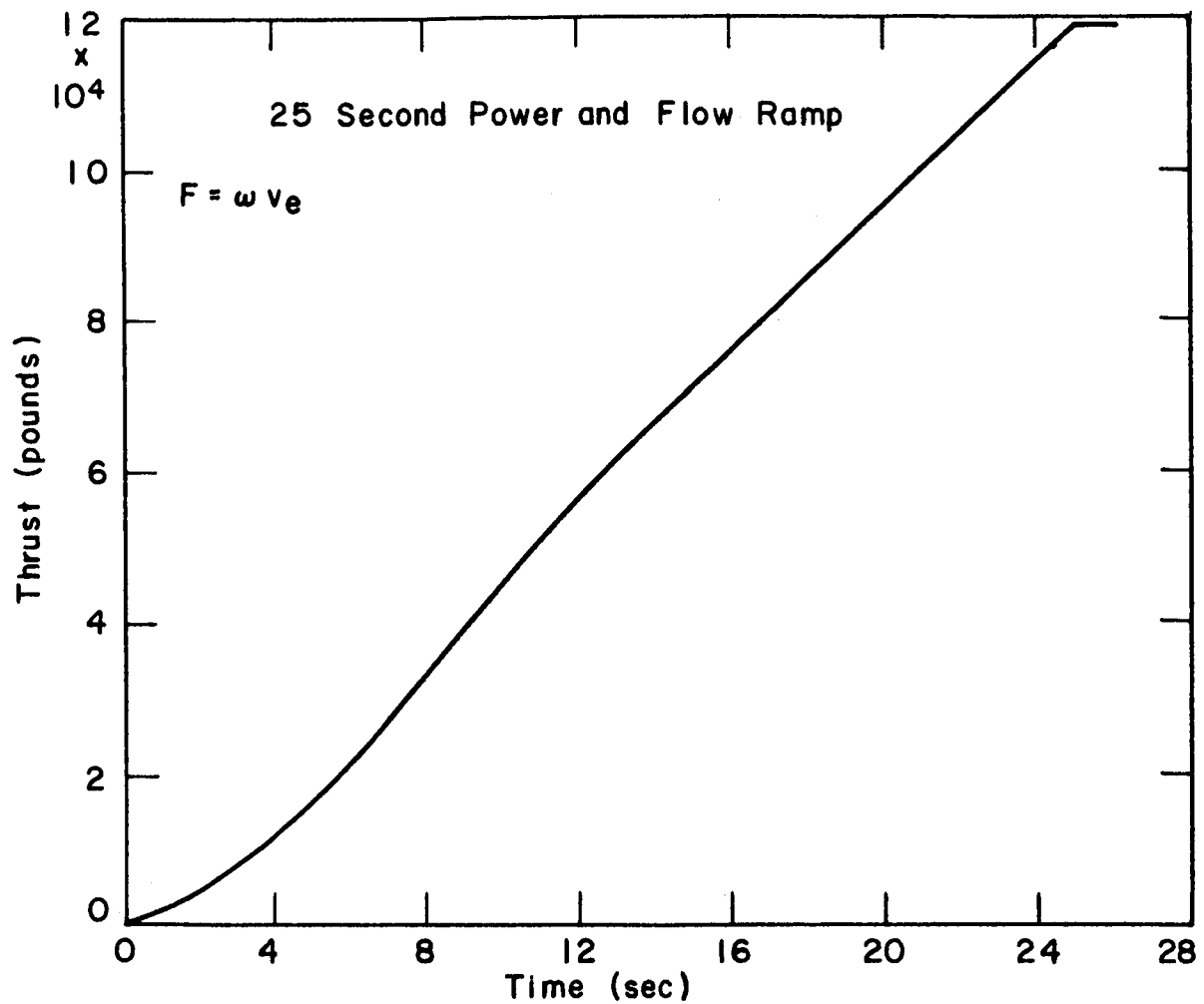
Figure 4.6.6. Rocket Thrust During Startup.

V. REACTIVITY VARIATION DURING STARTUP

5.1 Introduction

In this chapter, the reactivity variations during startup, which are caused by changes in core temperature and hydrogen density, will be computed using the nucleonics model described in Chapter III. The time dependent core properties necessary for this calculation will be obtained from the fluid flow model discussed in Chapter IV. The time dependent reactivity variation will be shown for both a clean and a poisoned core.

In reality, of course, changes in core temperature and hydrogen density are not the only causes of reactivity perturbations. Fuel burnup and xenon buildup also produce reactivity changes, but these changes are exceedingly small for startup times of approximately one minute. It is quite conceivable that fuel expansion is of more significance than either fuel burnup or poison buildup. However, the effect of fuel expansion is not considered because it is very sensitive to the construction and geometry of the reactor core.

It should be made absolutely clear at this point that all "reactivities" discussed in this chapter refer to the change in reactivity induced by changes in core properties. In particular, the reactivity variations brought about by core changes should not be confused with the reactivity necessary to achieve a linear power increase during startup, which shall be discussed in the next chapter.

5.2 Averaging Scheme Used to Obtain Lumped Values of Hydrogen Density and Core Temperature

In order to compute the reactivity at any given time during startup, some sort of spatial average of the core properties must be made because the reactivity model employed has no spatial dependence. One method would be to take a simple volume average of the core properties at each time step, and then compute the reactivity using these average

properties. This procedure is strictly valid only if: the reactivity is a linear function of both core temperature and hydrogen density; all positions in the core have equal importance. Although the reactivity is roughly a linear function of both core temperature and hydrogen density (refer to Chapter III), the neutron importance will certainly vary with position.

The averaging procedure employed in this thesis consists of computing a reactivity using the properties at each mesh point in the core, weighting by the power density at that mesh point, and then averaging the reactivities. In mathematical form,

$$\rho_{average} = \sum_{i=1}^{N} P_i \rho_i \qquad (5.2.1)$$

where:

N = number of equally spaced axial mesh points (twenty)

P_i = normalized power density at axial mesh point i

ρ_i = reactivity calculated using properties at mesh point i

The axial power density, which was shown in Figure 4.3.2, was taken from a multigroup, 2-dimensional diffusion theory calculation (14), and normalized so that

$$\sum_{i=1}^{N} P_i = 1.0 \qquad (5.2.2)$$

The same power distribution was used for all computations.

This averaging procedure is preferable to the simple volume averaging first discussed because:

1) Nonlinearities in the temperature and hydrogen reactivity coefficients are better approximated.
2) A semblance of the relative importance of the different spatial mesh points is introduced.

It is thought, therefore, that within the spirit of a lumped parameter reactivity model, the averaging procedure described by Eq. (5.2.1) should be adequate. This should be all the more true because:

1) The reactivity is roughly a linear function of both hydrogen density and core temperature.

2) The spatial distribution of the importance should not significantly change during startup.

5.3 Reactivity Variation During Startup

The variation in reactivity during startup for various carbon-to-fuel ratios is shown in Figure 5.3.1. All calculations are for the 25-second power and flow ramps discussed in Chapter IV. The important parameters are given in Table 4.6.1. A clear understanding of the reactivity changes can be obtained from Figures 5.3.2 and 5.3.3, which give the average hydrogen density and core temperature, respectively. Observe that the core temperature is close to its maximum value in approximately half the startup period. It is this rapid temperature rise which causes the initial dip in the reactivity profile. As one would expect, the reactivity dip is quite pronounced in thermal cores (C/U $\cong$ 2500), which are more sensitive to temperature changes than epithermal cores (C/U $\cong$ 500). The linear reactivity rise after the initial dip is caused by the smooth hydrogen buildup.

Note that both large and rapid reactivity variations occur during the startup of large, thermal reactors. Such large reactivity changes can be partially subdued by adding a thermal poison to the core. This procedure has the double virtue of:

1) Decreasing the hydrogen reactivity worth by reducing the probability that a thermal neutron will be captured in the fuel. This can be seen by comparing Figures 5.3.4 and 3.8.1.

2) Decreasing the magnitude of the temperature coefficient by hardening the thermal spectrum. See Figures 5.3.5 and 3.8.2.

The time dependent reactivity in a poisoned core is shown in Figure 5.3.6. For this calculation, a 1/v poison was used with a macroscopic cross section equal to 1/4 that of U-235 at 0.025 ev. Although this is a rather large poison concentration, it is obviously of appreciable value in reducing the fluctuations in reactivity during startup.

However, it is important to understand that a poison reduces the fraction
of neutrons leaking out of the core, and consequently the worth of external
control rods. This phenomenon will be discussed in more detail in
Chapter VII.
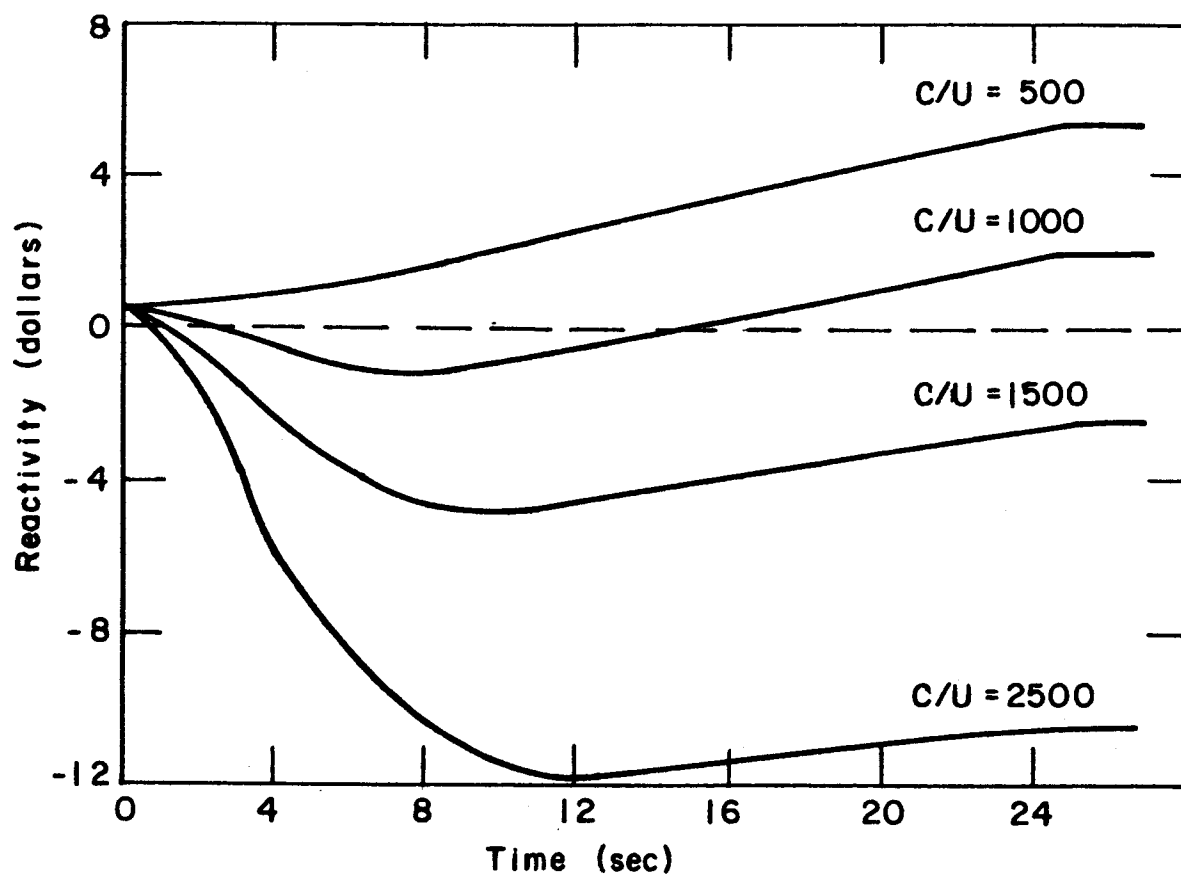
Figure 5.3.1. Reactivity Variation During 25 Second Startup.
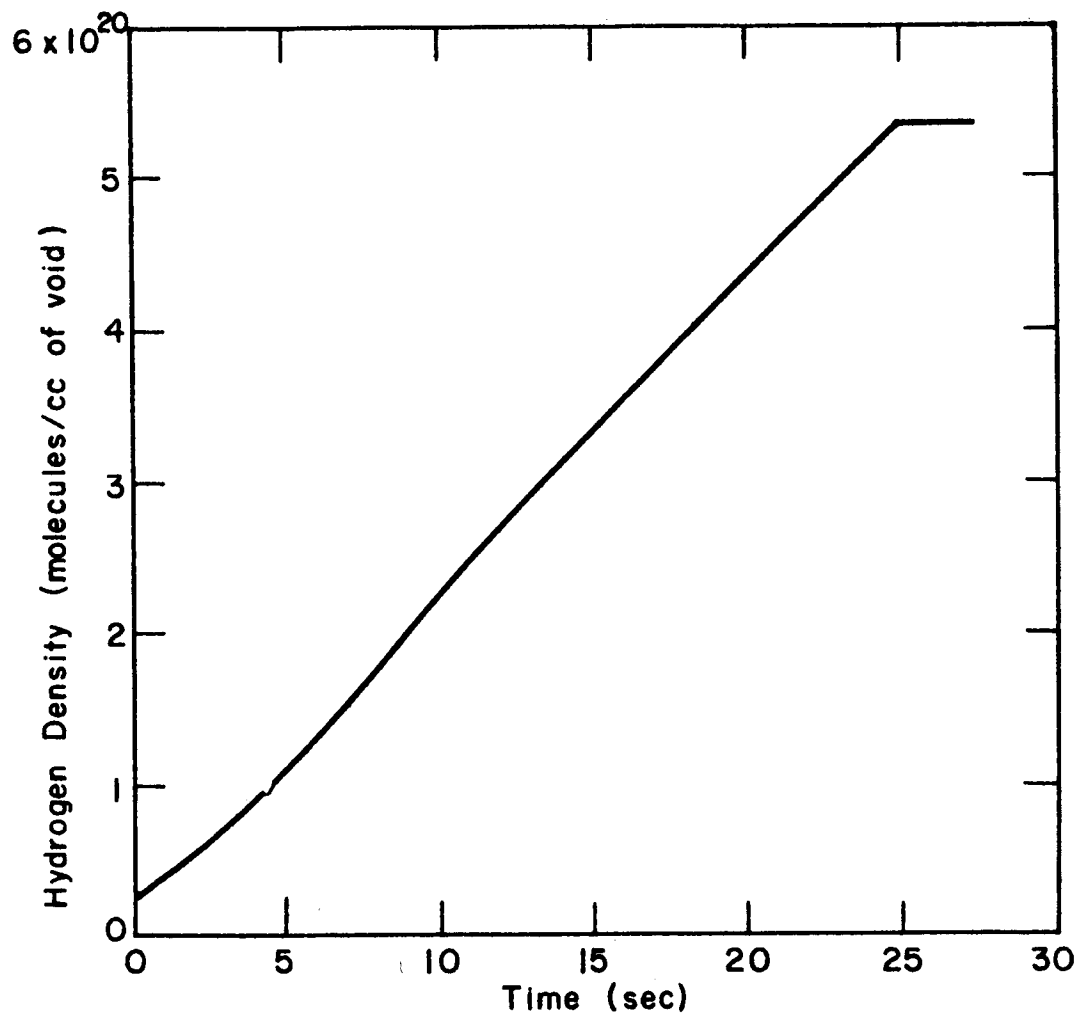
Figure 5.3.2. Average Hydrogen Density in Core During 25 Second Startup.
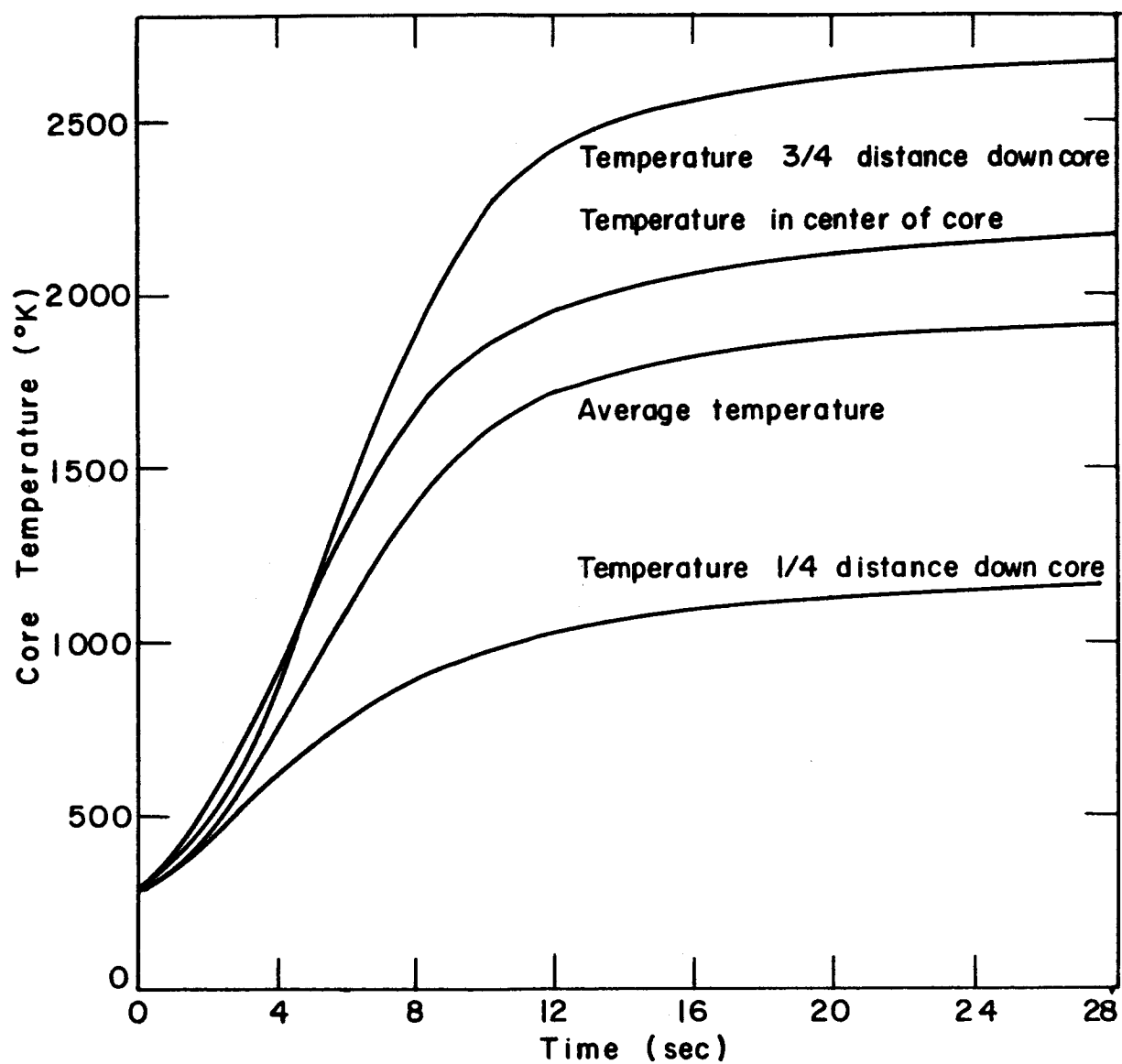
Figure 5.3.3. Core Temperature During Startup.
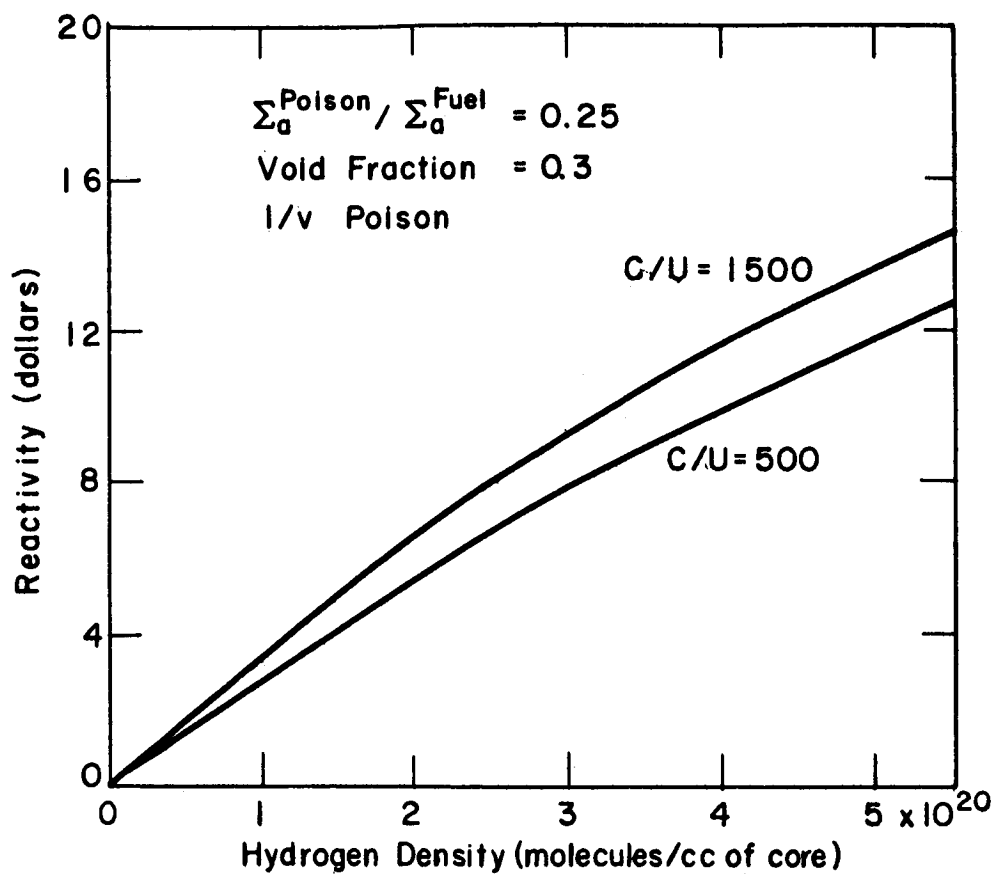
Figure 5.3.4. Reactivity Worth of Hydrogen in a
Poisoned Core.
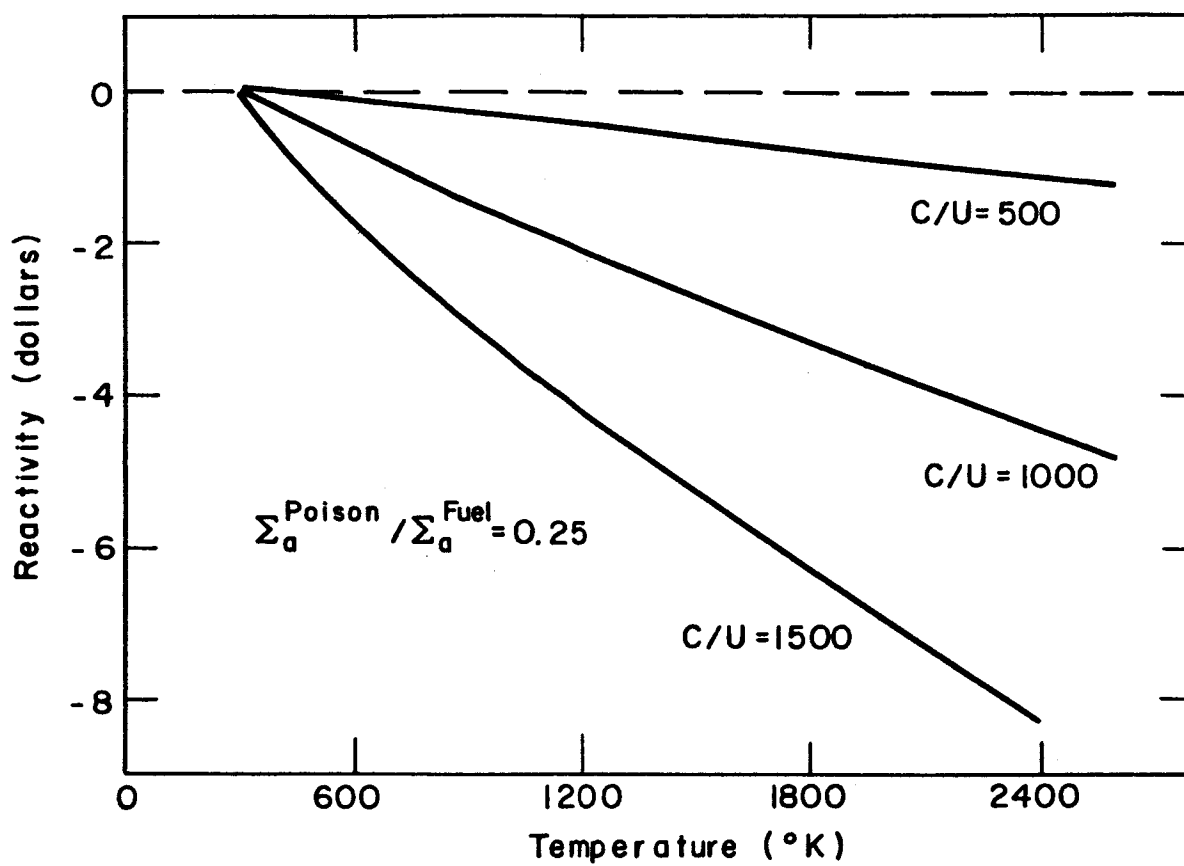
Figure 5.3.5. Reactivity as a Function of Core Temperature in a Poisoned Core.
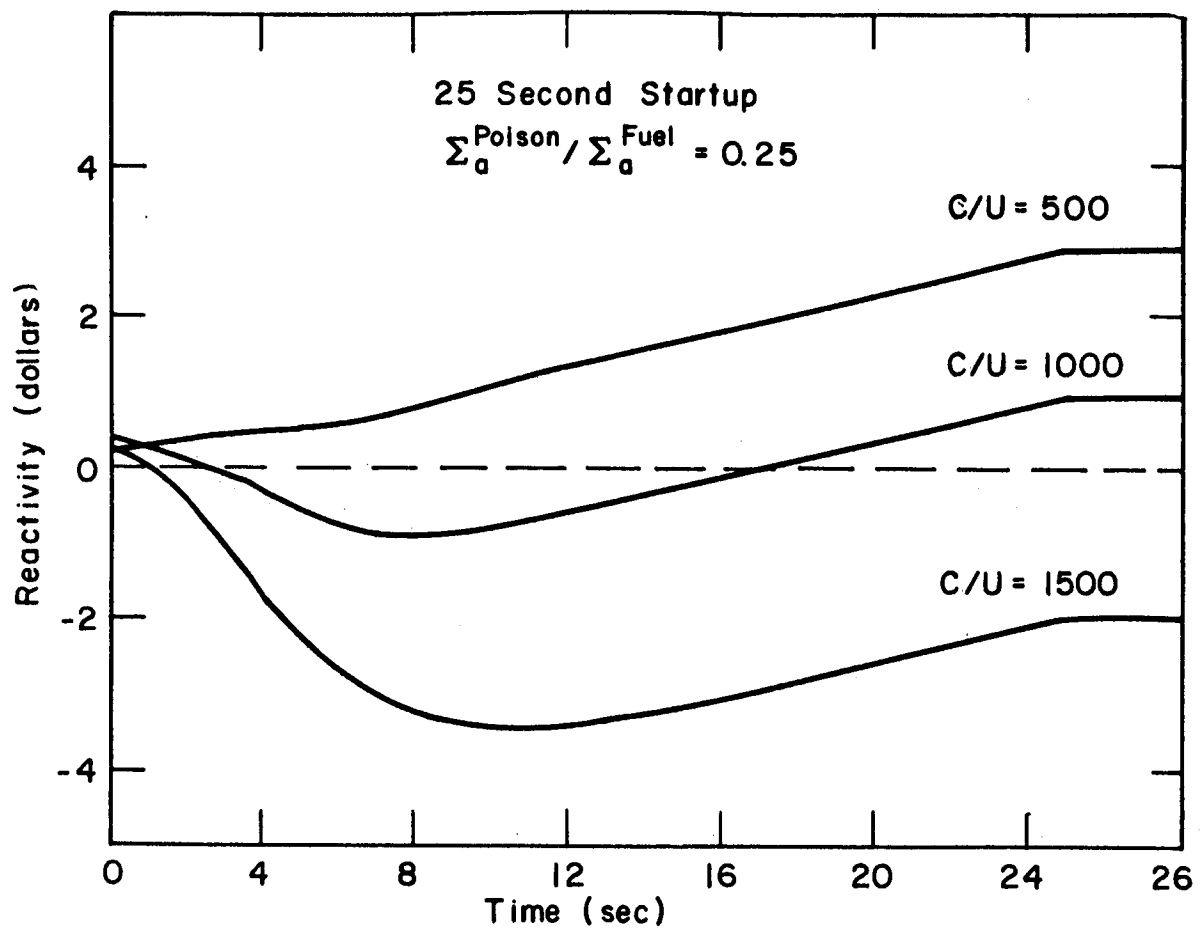
Figure 5. 3. 6. Reactivity Variation During Startup In a Poisoned Core.

VI. ESTIMATE OF REACTIVITY REQUIRED
FOR RAMP POWER RISE

6.1 Introduction

In order to achieve a linear rise in power during startup, the total reactivity of the system must follow a prescribed course, $\rho(t)_{total}$. The total reactivity, or more precisely, the total reactivity variation from equilibrium, is merely the sum of all reactivity perturbations induced by changes in control rod position, core temperature, etc. Therefore, to produce a linear increase in power, the control rods must be adjusted so that

$$\rho(t)_{control\ rods} = \rho(t)_{total} - \rho(t)_{T\ and\ H_2} \qquad (6.1.1)$$

The objective of this section is to estimate the total reactivity $(\rho(t)_{total})$ necessary to produce a linear power increase. With this information, and the results of the previous chapters, the required rod movement can be computed via Eq. (6.1.1). Note that both the rate and magnitude of the required rod movement are measures of the feasibility of a given startup scheme.

6.2 Mathematical Model

For the calculation of the total reactivity, we shall assume:
1) A one energy group kinetics model with six precursor groups gives an adequate representation of the dynamic system. See Appendix D for a discussion of the effect of using less than six precursor groups.
2) The neutron density is a linear function of time for $0 < t < t_o$. For $t > t_o$, the neutron density is constant. See Figure 6.2.1.
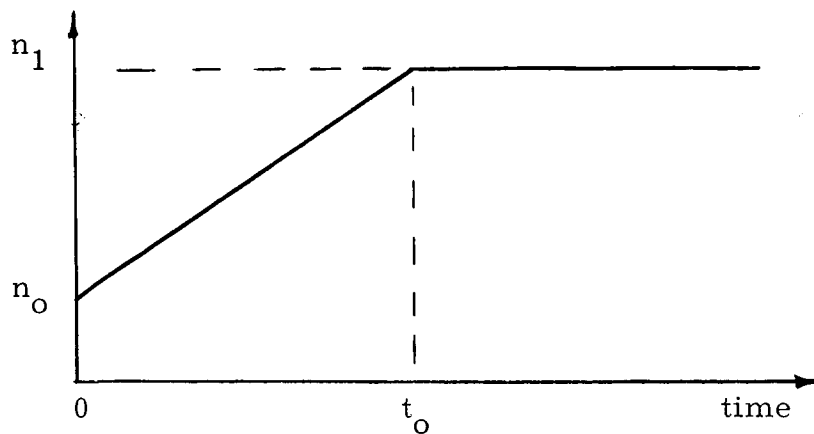
Figure 6.2.1. Neutron Density During Startup

3) The neutron generation time is constant; hence power is
   a linear function of neutron density.

4) The neutron precursors are at equilibrium at $t = 0$.

The above assumptions merit a few remarks. A point kinetics
model should be quite sufficient because the flux shape does not appreci-
ably change during startup; a detailed discussion of flux tilting is given
in Appendix C. The assumption of a constant generation time is not
strictly valid because changes in core temperature alter the fission
cross section, which consequently perturbs the generation time. However,
small changes in the generation time are of little import because a
reactor is rather insensitive to the generation time during delayed critical
operation.

The initial precursor density is, of course, a function of the
manner in which the reactor is brought from the source power range to
the startup power range. It is conceivable that one might wish to bring
the reactor up to the startup power range on an asymptotic period of
only a few seconds. This means that the initial precursor density in the
startup range might well be much less than its equilibrium value. Never-
theless, an equilibrium precursor density will be assumed because the
nature of the power variation from source range to power range is not

known. Observe that this assumption is optimistic in the sense that fewer initial precursors would make the system more sensitive to reactivity variations, hence more difficult to control.

The well-known point kinetic equations have the form

$$\frac{dn}{dt} = \frac{\rho - \beta}{\Lambda} n + \sum_1^6 \lambda_i C_i \qquad (6.2.1)$$

$$\frac{dC_i}{dt} = \frac{\beta_i n}{\Lambda} - \lambda_i C_i \qquad (6.2.2)$$

For $t < t_o$, $n = n_o(1+\gamma t)$; hence

$$\rho(t) = \frac{\gamma}{1 + \gamma t}\left[\Lambda + \sum_1^6 \frac{\beta_i}{\lambda_i}\left(1 - e^{-\lambda_i t}\right)\right] \qquad (6.2.3)$$

where

$$\gamma = \frac{n_1 - n_o}{n_o t_o}$$

For $t > t_o$, $n = n_1$; therefore

$$0 = \frac{\rho - \beta}{\Lambda} n_1 + \sum_1^6 \lambda_i C_i \qquad (6.2.4)$$

$$\frac{dC_i}{dt} = \frac{\beta_i n_1}{\Lambda} - \lambda_i C_i \qquad (6.2.5)$$

Solving these equations, we find that

$$\rho(t) = \frac{\gamma n_o}{n_1} \sum_1^6 \left[\frac{\beta_i}{\lambda_i}\left(e^{-\lambda_i t_o} - 1\right)e^{-\lambda_i t}\right] \qquad (6.2.6)$$

Note from Eq. (6.2.3) that the reactivity is independent of the ramp slope if $t \gg 1/\gamma$.

6.3 Results and Observations

The required reactivity for various power ramps is shown in Figure 6.3.1. The precursor group constants used in these calculations were taken from Keepin (29). There are a number of observations
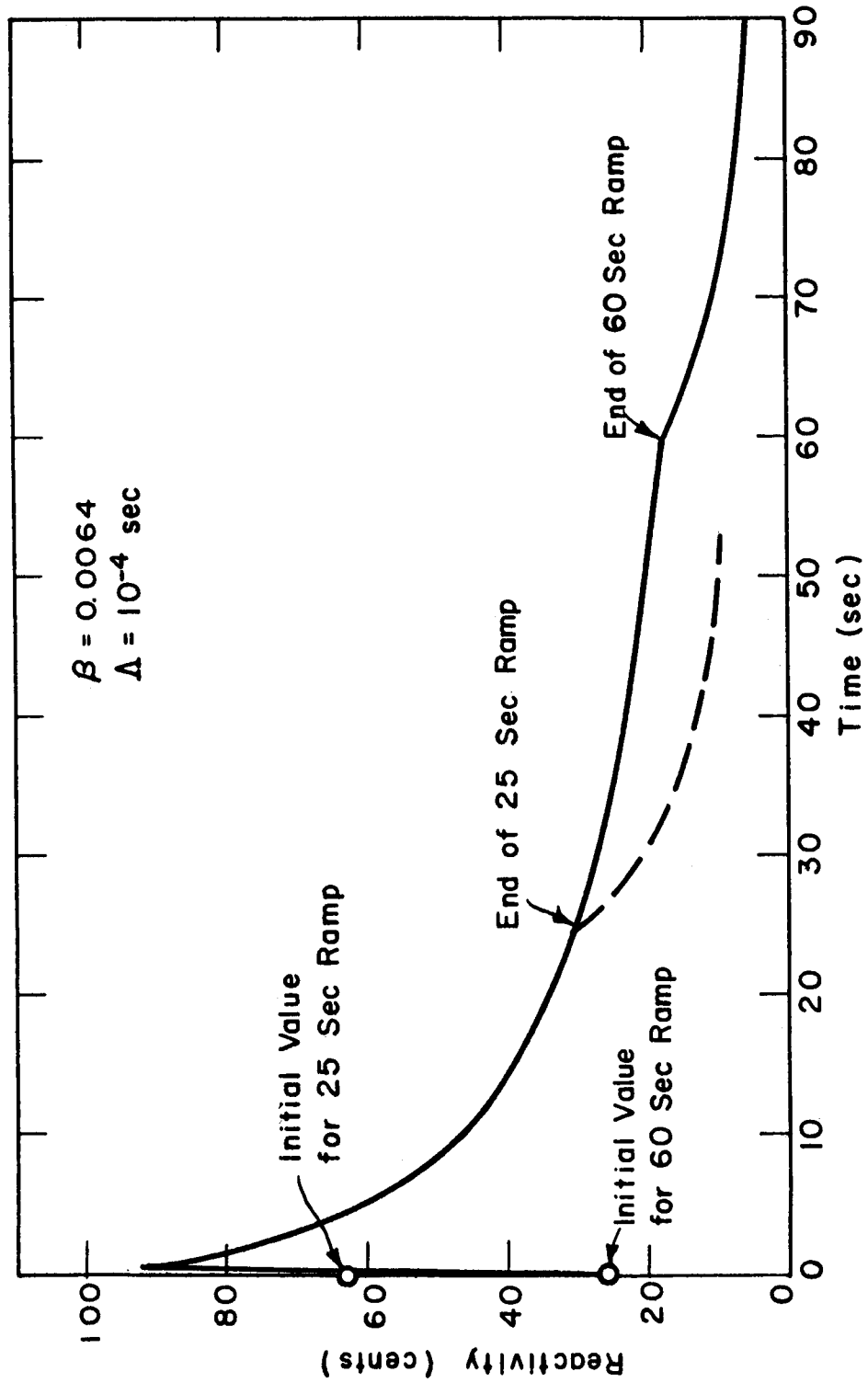
Figure 6.3.1. Reactivity Required for Power Ramp.

one can make on these results.

1) The initial reactivity required is simply $\gamma \Lambda$. Note that this is independent of precursor constants (which it must be because we are starting from equilibrium) and directly proportional to the ramp rate.

2) It is perhaps startling that after a fraction of a second the required reactivity is independent of the ramp rate. In a fast ramp, slightly more neutrons are initially produced than in a slow ramp. These additional neutrons constantly produce more neutrons; hence the production rate for a fast ramp is faster, even though the reactivity is the same.

3) Even after startup has been completed, considerable reactivity (20¢) is needed to bring the precursors up to equilibrium.

4) For generation times less than 10^{-4} seconds, the required reactivity after a fraction of a second is independent of the generation time. This can be seen by observing that the second term on the right-hand side of Eq. (6.2.3) is much larger than the generation time.

6.4 Conclusions

Figure 6.3.2 shows that the total reactivity during the initial moments of startup is uncomfortably close to one dollar (indeed, even greater than one dollar for short ramps). In light of the possible drastic consequences of prompt reactivities (see Chapter VIII), it is perhaps prudent to forgo the demand of a linear power increase during the initial seconds of startup. This appears all the more reasonable considering that nuclear rockets will probably be virgin at launch time; hence the exact reactivity worth of the poison rods and hydrogen propellant will be unknown.

For any approximately linear power rise during startup, it is clear that rapid startups (~30 seconds) require rather large reactivities (~50 cents). However, the reactivity changes induced by variations in hydrogen density and core temperature, which were discussed in the previous chapter, are an order of magnitude larger than 50 cents. This
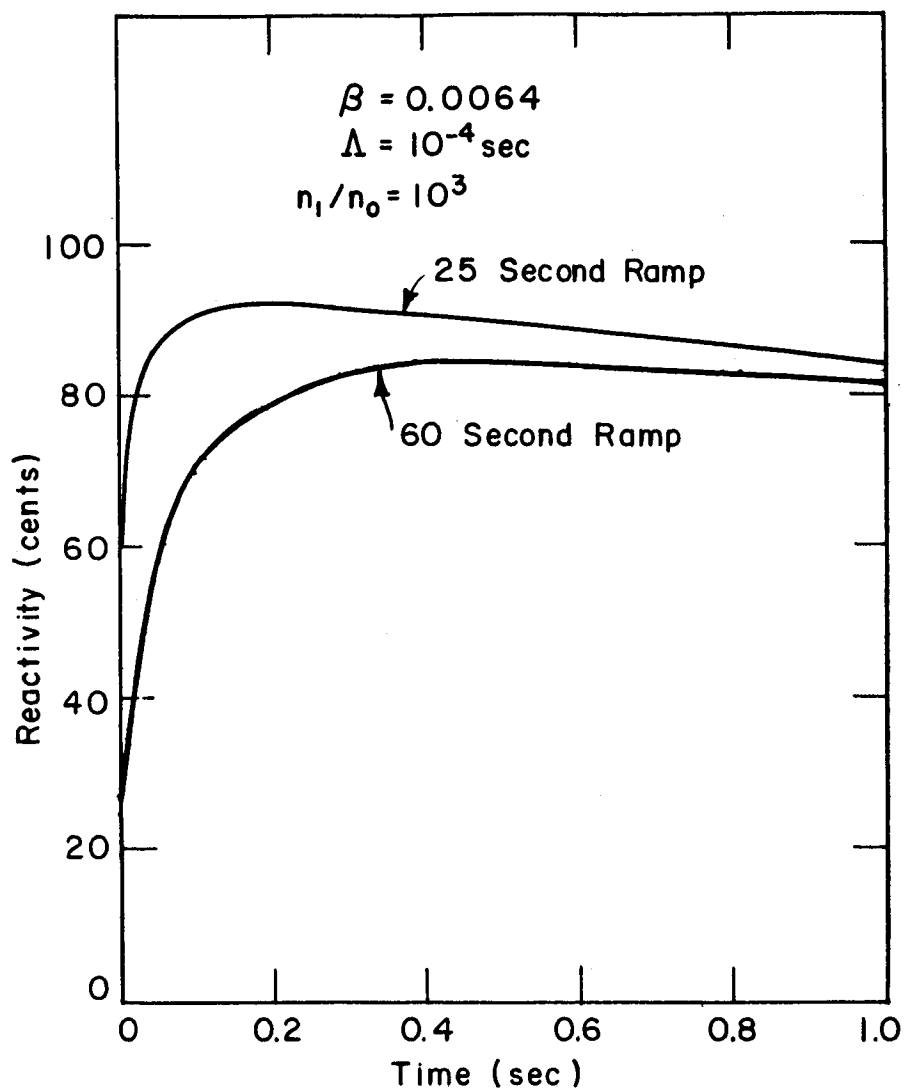
Figure 6.3.2. Initial Reactivity for Power Ramp.

indicates that the control system must have sufficient size to compen-
sate for the large reactivity variations, and sufficient precision to
rapidly increase power without allowing the reactor to become prompt
critical.

VII. ESTIMATE OF CONTROL ROD WORTH

7.1 Introduction

In order to assess the severity of the reactivity perturbations induced by changes in hydrogen density and core temperature, the approximate reactivity worth of the control system must be known. It is clear that the reactor system would be difficult or impossible to control if the induced reactivity perturbations are comparable to or greater than the total worth of the control system.

The two principle methods of reactor control are:

    1) Insertion of poison rods into the core (internal control).

    2) Rotation of control rods in reflector (external control).

The core of nuclear rocket is somewhat inaccessible because it has an extremely high power density (~1 Mw/liter) (13) and temperature (~2800°K). This indicates that an internal control system might be exceedingly difficult to construct and operate. This investigation, therefore, shall be confined to the problem of estimating the worth of exterior control rods.

7.2 Method of Approach

Reflector reactivity control in an intermediate or thermal core can be achieved by placing rotating poison rods in the reflector. See Figure 7.2.1. One side of each rod is coated with a neutron absorber. Reactivity is increased by rotating the poison side away from the center of the core, and decreased by rotating the poison toward the center.

For a given reactor configuration (i.e., dimensions, materials, number of rods, type of poison, etc.), the total worth of an external control system can be found by computing the reactivity change when the rods are turned from the "in" position to the "out" position. However, a detailed calculation of this reactivity change encounters two major difficulties:
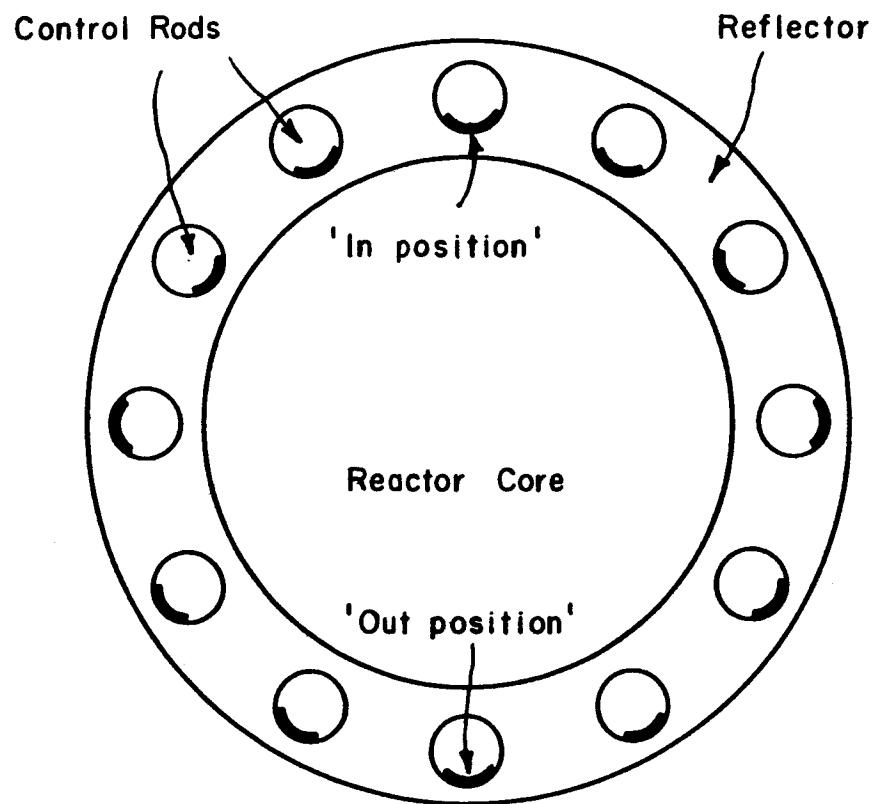
Figure 7.2.1. Top View of Reflector Controlled Reactor.

1) It requires a two-dimensional multigroup transport or diffusion theory calculation, which involves considerable computer time.

2) It requires the knowledge of the number of rods, size of rods, type of poison, thickness of poison, etc.

To simplify the above problems, the following assumptions are made:

1) The reactivity in the original core is approximately equal to the reactivity in a core with the reflector chopped off at the position of the poison. This implies that the approximate worth of a control system can be calculated by merely varying the reflector thickness.

2) The reactivity in the chopped off core can be adequately computed by a one-dimensional model. In other words, it is assumed that the axial leakage can be simulated by a constant buckling term.

The first assumption deserves a few remarks. Although thermal neutrons are readily absorbed in the poison region, fast neutrons can easily pass through. Hence the assumption that the fast flux goes to zero in the poison region is rather crude. However, the assumption is not as bad as it may first appear because the fast neutrons which pass through the poison and thermalize in the reflector have a very low probability of returning to the core. These neutrons, therefore, have only a small influence on reactivity. In any event, it is clear that the proposed model gives a very optimistic estimate, or upper bound, on the control rod worth.

The second assumption, concerning axial leakage, allows the investigation of numerous cases with only a moderate expenditure of computer time. In light of the fact that only differences in reactivity are of interest (i.e., differences in reactivity for various reflector thicknesses), the second assumption should be quite sufficient.

7.3 Outline of Mathematical Model

The reactivity for various reflector thicknesses was calculated using a modified version of the Twenty Grand Code (30). This is a two-dimensional (only the radial dimension was used), multigroup, diffusion theory model using a successive displacement over-relaxation iteration algorithm. Three energy groups, consisting of one fast group and two overlapping thermal groups, were used for all calculations. The cross sections for the various groups were taken directly from Plebuch (14). Briefly, Plebuch obtained the fast group cross sections from the GAM-I fast spectrum code. The thermal cross sections were found by averaging over a Wilkins flux distribution.

7.4 Results

An intermediate, epithermal, and thermal core were investigated. For each carbon-to-fuel ratio, the core size was chosen so that the system was close to critical with a 10-cm radial reflector. In detail, the cases considered were:

1) An intermediate reactor with a carbon-to-U-235 ratio of 100 and a radius of 41.5 cm. The axial leakage was computed assuming a bare core height of 120 cm.

2) An epithermal system with a carbon-to-fuel ratio of 500 and a bare radius of 72.5 cm. The height of the bare core was taken to be 120 cm.

3) A thermal system with $C/U = 2500$ and a bare radius of 89.5 cm. The core height was taken to be 150 cm.

For each case, the reactivity was computed for five different reflector thicknesses. The graphite core and the beryllium reflector were assumed to be operating at 2780°K and 222°K, respectively. The solid fraction was taken to be 0.7 for the core and 0.9 for the reflector. The numerical results are shown in Figure 7.4.1.

It is clear from the results that the worth of an external control system decreases as the reactor becomes larger and more thermal. Note that the control system in the $C/U=100$ core is worth almost twice as much as the control system in the $C/U=500$ core. But the control
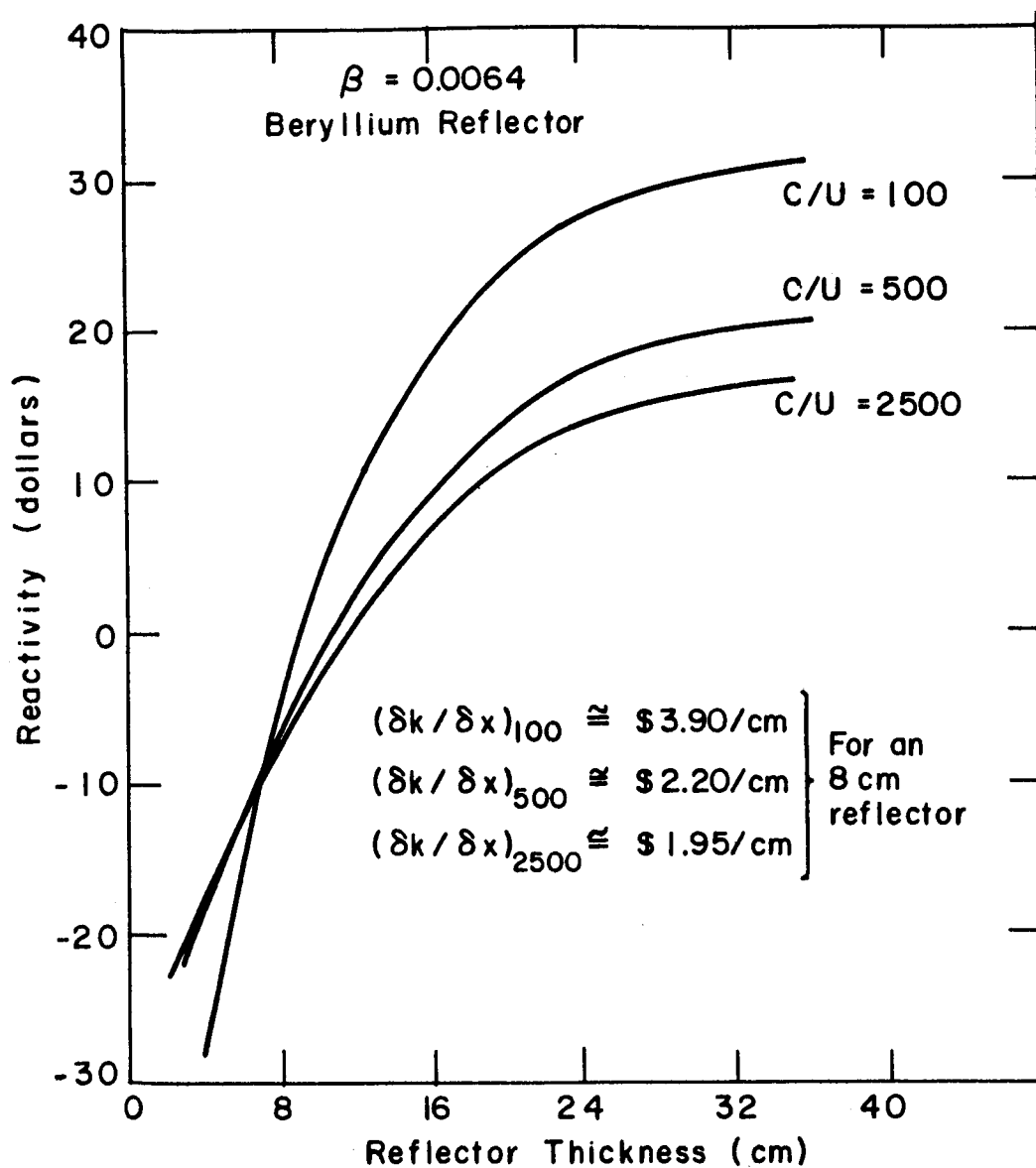
Figure 7.4.1. Effect of Reflector Thickness on Reactivity.

system in the C/U=500 core is only slightly more valuable than the
control system in the C/U=2500 core because the thermal core is longer,
hence has more radial leakage.

The variation in rod worth can be roughly explained in the following
manner. The leakage neutrons from the small core have an energy
spectrum far above the thermal region. A fraction of these neutrons
are thermalized in the cold reflector and scattered back into the core.
Upon returning to the core, the cold neutrons are immediately captured
because of the high fuel density (C/U = 100).

In the case of a thermal core, the neutrons returning from the
reflector are not immediately captured because the density of fuel is
low. In fact, they may be scattered back into the reflector and escape
from the system. Therefore, a reflector on an intermediate core will
tend to have more reactivity value than a reflector on a thermal core.

The above argument does not do complete justice to the complex
physical situation. Other factors are important. As the ratio of carbon
to fuel is varied, the spectrum varies; hence the average value of eta (η)
changes. This, in turn, alters the total fraction of neutrons leaking out
of the system.

It is important to note that all calculations were performed with
no poison (structure, cladding, etc.) in the core. Any poison will reduce
the worth of an external control system by decreasing the thermal utili-
zation, forcing the leakage fraction to decrease.

The reflector worth shown in Figure 7.4.1 was computed for three
fixed core sizes. Such information is of little value if it is highly sensi-
tive to the core dimensions. In order to test the sensitivity of the
reflector worth to the core dimensions, the reflector worth was calcu-
lated for two different core sizes.

Figure 7.4.2 demonstrates the effect of increasing the core height.
As one would expect, an increase in core height increases the reactivity.
Also, an increase in core height increases the external control rod worth
slightly by increasing the radial leakage. However, this effect is almost
·imperceptible for height variations of less than 10 cm.

In a similar manner, an increase in the core radius increases the
reactivity but decreases the control rod worth by decreasing the radial
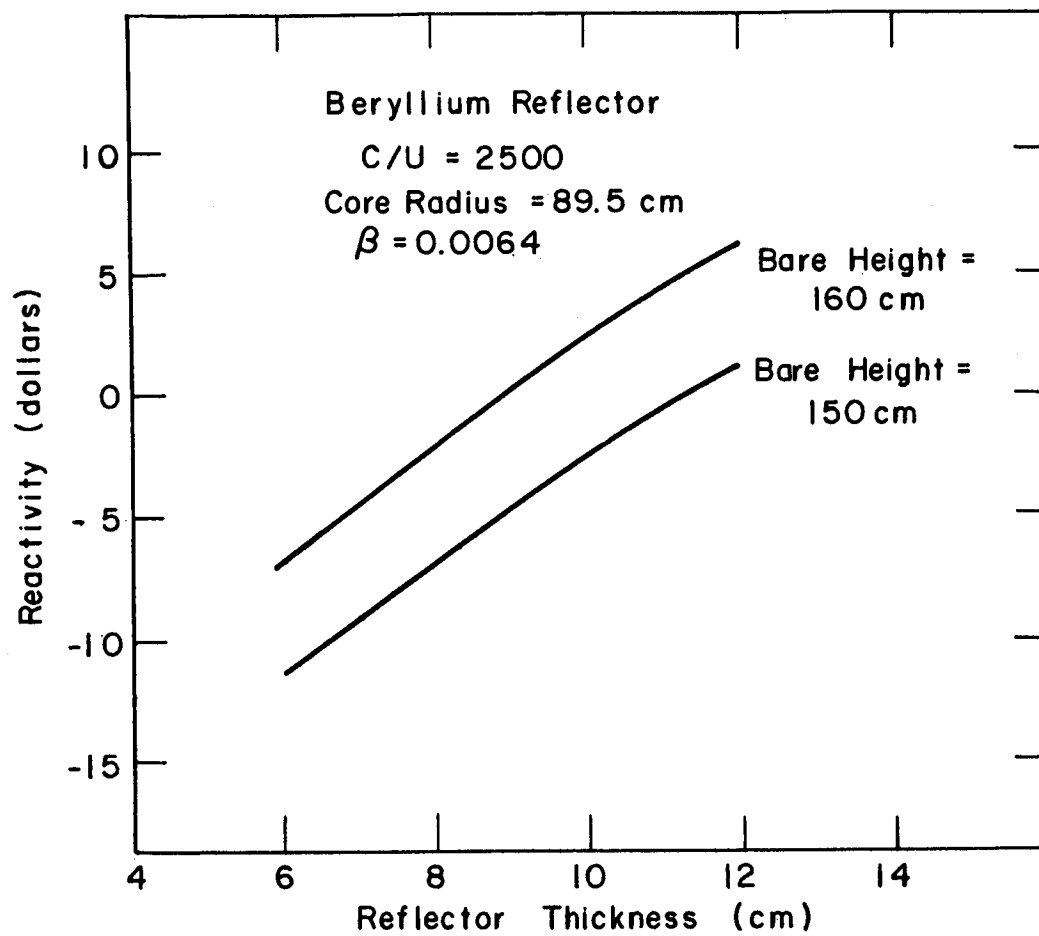
Figure 7.4.2. Effect of Core Height on Reflector Worth.

leakage. This is shown in Figure 7.4.3. Again, the change in control rod worth is insignificant for changes in radius less than 5 cm.

In passing, it is frustrating to observe that larger cores have smaller rod worth, but larger reactivity variations induced by hydrogen and temperature changes (see Chapter V). For example, $25. of control would require a change in reflector thickness of approximately 15 cm in a thermal core (C/U = 2500). Even if such a large reflector control were achievable, the reflector weight would become exorbitant.
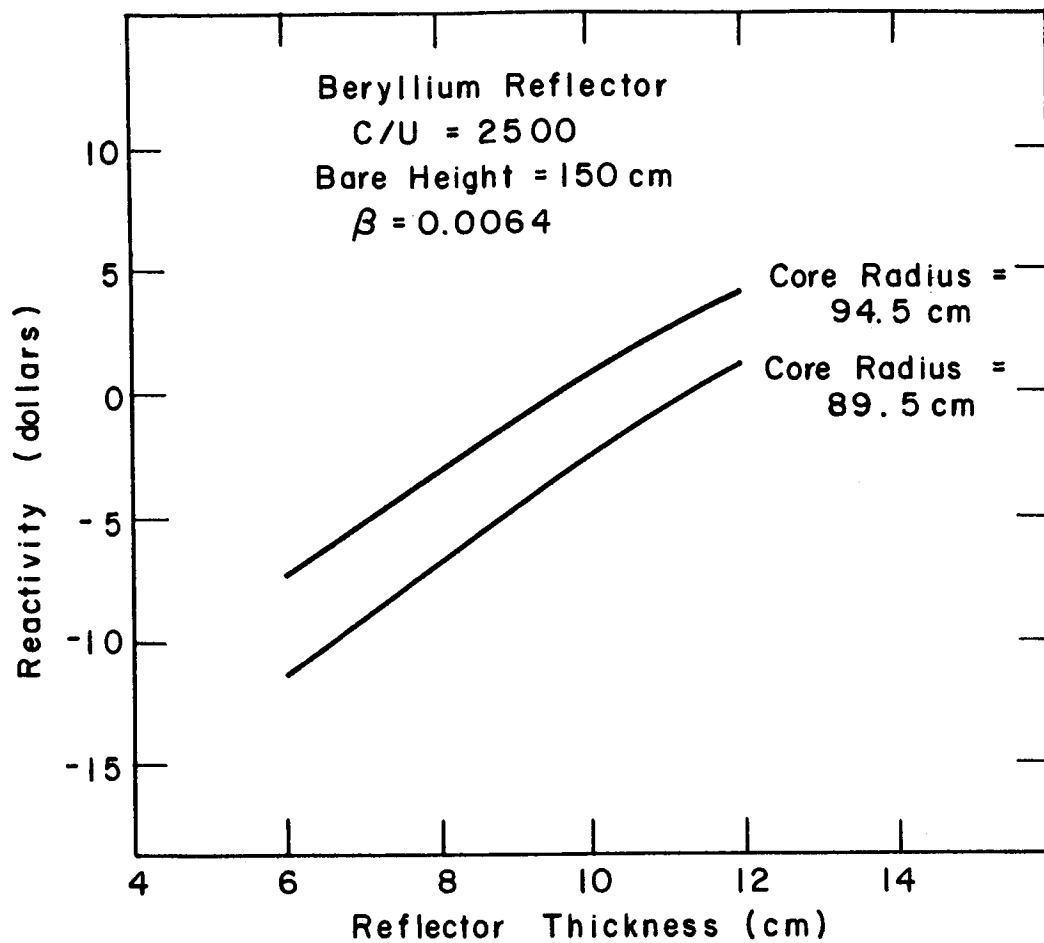
Figure 7.4.3. Effect of Core Radius on Reflector Worth.

VIII. POSSIBLE ACCIDENTS (LARGE EXCURSIONS)

8.1 Objective

In Chapter VI, it was demonstrated that short startups require a total reactivity comparable to one dollar. Due to human error or mechanical failure, there is an outside chance that too much cold hydrogen will enter the core. Clearly, from the graphs of hydrogen worth shown in Chapter III, such an event could lead to reactivities significantly greater than one dollar. The objective of this section is to describe the general behavior of a prompt critical reactor and to assess the severity of prompt reactivities.

8.2 Mathematical Model and Approximations

The well-known one energy group, six precursor groups kinetics model shall be used to simulate prompt excursions. These equations have the form

$$\frac{dn(t)}{dt} = \frac{\rho(t) - \beta}{\Lambda} n(t) + \sum_{1}^{6} \lambda_i C_i(t) \tag{8.2.1}$$

$$\frac{dC_i(t)}{dt} = \frac{\beta_i n(t)}{\Lambda} - \lambda_i C_i(t) \tag{8.2.2}$$

All symbols are defined in Table 8.2.1.

For the analysis of prompt excursions, it is more convenient to deal with power density than neutron density. Assuming constant nuclear properties, the power density, $P(t)$, is given by the expression

$$P(t) = \frac{\epsilon}{\nu} (\nu v \Sigma_f) n(t) \tag{8.2.3}$$

or

$$P(t) = \frac{\epsilon}{\nu \Lambda} n(t) \tag{8.2.4}$$

Table 8.2.1. Symbols for Kinetic Equations

$C_i(t)$ Precursor density for group i (cm^{-3})

$C_i'(t)$ Modified precursor density defined by Eq. (8.2.7)

$n(t)$ Neutron density (cm^{-3})

$P(t)$ Power density (watts/cc)

v Neutron velocity (cm/sec)

β Total delayed neutron fraction

β_i Delayed neutron fraction for group i

ϵ Energy released per fission (joules)

Λ Generation time (sec)

λ_i Delay constant for group i (sec^{-1})

ν Prompt neutrons per fission

$\rho(t)$ Reactivity

Σ_f Macroscopic fission cross section (cm^{-1})

where $\epsilon/\nu = 1.2 \times 10^{-11}$ joules for U-235

If Eqs. (8.2.1) and (8.2.2) are multiplied by the constant $\epsilon/\nu\Lambda$, we obtain

$$\frac{dP(t)}{dt} = \frac{\rho(t) - \beta}{\Lambda} P(t) + \sum_{1}^{6} \lambda_i C_i'(t) \qquad (8.2.5)$$

$$\frac{dC_i'(t)}{dt} = \frac{\beta_i P(t)}{\Lambda} - \lambda_i C_i'(t) \qquad (8.2.6)$$

where

$$C_i'(t) = \frac{\epsilon}{\nu\Lambda} C_i(t) \qquad (8.2.7)$$

Note that the above equations have exactly the same form as Eqs.(8.2.1-2). The only differences are that the neutron density has been replaced by the power density, and the actual precursor density has been replaced by a constant multiple of itself.

It should be mentioned that Eqs. (8.2.1-2), or (8.2.5-6) are some-times not valid for the analysis of very large bursts. This question has been discussed at length by both Henry (31) and Gyftopoulos (32). In very crude terms, if the neutron flux shape changes significantly during the burst, the one energy group space independent model is invalid, or more precisely, the variables lose their physical meaning. In Appendix C it is demonstrated that, for a slab graphite moderated reactor with a width of 1 meter, large spatial cross section variations (in a dynamic sense) cause a quite small variation in the flux shape. Hence it appears that a space independent kinetics model should be reasonably accurate for graphite moderated nuclear rockets. In any event, in this investigation, as in many other calculations of large excursions, the objective is to obtain the characteristic behavior of the system rather than precise numerical data.

8.3 Reactivity Expression and Shutdown Mechanism

The total reactivity, $\rho(t)$, which appears in Eq. (8.2.1), is assumed to be of the form

$$\rho(t) = a + bt - S \int_0^t P(t')\, dt' \qquad (8.3.1)$$

The first two terms in Eq. (8.3.1), $a+bt$, act as a "drive" or "source" for the excursion. For example, the prompt burst resulting from a reactivity step of two dollars ($1.00 = 0.0064) would be obtained by setting $a = 0.0128$ and $b = 0$.

The shutdown term in Eq. (8.3.1),

$$\rho(t)_{\text{shutdown}} = -S \int_0^t P(t')\, dt' \qquad (8.3.2)$$

gives the reactivity feedback caused by an increase in fuel temperature, or energy content. Note that we have made a reasonable assumption that

the shutdown mechanism is instantaneous. For a nuclear rocket core, this assumption is quite good because the fission energy is deposited directly into the moderating material (carbon). Therefore, a power surge will almost instantaneously affect the thermal neutron spectrum, and thus the average thermal cross sections.

The shutdown coefficient, S, can be determined in the following manner. From Eq. (8.3.2), it is clear that S is merely the reactivity change per joule per cc of fission energy. Hence, for constant material properties, S can be expressed in terms of the temperature coefficient as

$$S = \frac{-10^4 \, \beta \, \frac{d\rho}{dT} \, (\text{¢}/\,^\circ K)}{C_p(\text{joules}/\text{kg-}^\circ K) \, \rho_o(\text{kg}/\text{m}^3)} \tag{8.3.3}$$

Note that ρ_o in the above equation is the material density, which should not be confused with $\rho(t)$, the reactivity.

The final expression for the shutdown reactivity is obtained by combining Eqs. (8.3.2) and (8.3.3). Therefore,

$$\rho(t)_{\text{shutdown}} = \frac{10^4 \, \beta \, \frac{d\rho}{dT}}{C_p \rho_o} \int_0^t P(t') \, dt' \tag{8.3.4}$$

For a given physical system, the constants in the above equation can be readily computed. With this information, and the reactivity input, $a + bt$, the reactor behavior during an excursion can be found by the simultaneous solution of Eqs. (8.2.5), (8.2.6), and (8.3.4).

8.4 Validity of Shutdown Model

The proposed shutdown mechanism is valid only if all the fission energy remains in the fuel during the burst. In other words, the heat transfer time constant must be much larger than the neutronic reactor period.

For prompt bursts, the reactor period is

$$T_{\text{neutronic}} \cong \frac{\Lambda}{\rho - \beta} \text{ seconds} \tag{8.4.1}$$

The time constant associated with heat transfer (see section 4.3) is given by the expression

$$T_{\text{heat transfer}} = \frac{\rho_o V C_p}{hA} \text{ seconds} \tag{8.4.2}$$

where:

C_p = heat capacity of core (joules/(kg-°K))

h = heat transfer coefficient (watts/(m^2-°K))

V/A = fuel volume to surface area ratio (m)

ρ_o = density of core (kg/m^3)

Using the numerical values listed in Table 8.4.1, which should adequately reflect the properties of a graphite nuclear rocket reactor during a large excursion, it is found that

$$T_{\text{neutronic}} = 0.031 \text{ seconds} \tag{8.4.3}$$

$$T_{\text{heat transfer}} = 0.238 \text{ seconds} \tag{8.4.4}$$

Table 8.4.1. Data for Time Constant Calculations

Neutronic Data

$$\Lambda = 10^{-4} \text{ seconds}$$

$$\rho = 1.5 \text{ dollars}$$

$$\beta = 0.0064$$

Heat Transfer Data

$$\rho_o = 1.7 \times 10^3 \text{ kg/}m^3$$

$$C_p = 2.0 \times 10^3 \text{ joules/(kg-°K)}$$

$$A/V = \frac{2 \times \text{void fraction}}{r_o(1\text{-void fraction})} = \frac{0.6}{1.2 \times 10^{-3}(0.7)} = 0.715 \times 10^3 \text{ m}^{-1}$$

$$h = 2 \times 10^4 \text{ watts/(}m^2\text{-°K)}$$

If these values are characteristic, the original assumption of no heat transfer is clearly permissible. It should be understood that there is nothing sacrosanct about the data given in Table 8.4.1. In particular, it is difficult to justify the value of the heat transfer coefficient, h, because of its strong dependence on flow rate and temperature. It is thought, however, that the above choice of h is pessimistic (i.e., too large numerically).

8.5 Reactor Behavior for Step Reactivity Insertions

The dynamic behavior of a reactor for step reactivity ($a > \beta$) insertions is easy to describe. In rough terms, after the reactivity input the power density rapidly increases until the shutdown integral, Eq. (8.3.2), reduces the reactivity to below prompt critical. The power density then quickly decreases until it reaches dynamic equilibrium with the precursor groups.

The magnitude of the burst can be approximated in the following manner. Let E be the energy released during the burst. From Eq. (8.3.1),

$$E = \int_0^{t_f} P(t') \, dt' \tag{8.5.1}$$

or

$$E = \frac{a - \rho_f}{S} \tag{8.5.2}$$

where the subscript f denotes the final value, or value after the burst is completed. The final reactivity, or reactivity immediately following the initial burst, is easy to compute. From Eq. (8.2.5), the reactivity can be seen to be very close to one dollar at the peak of the burst. By symmetry, the total reactivity variation during the burst is merely twice the change from the beginning to the peak, or $2(a-\beta)$. Therefore, the final reactivity is

$$\rho_f = a - 2(a-\beta) \tag{8.5.3}$$

or

$$\rho_f = 2\beta - a \tag{8.5.4}$$

Placing Eq. (8.5.4) back into Eq. (8.5.2), the expression for energy release becomes

$$E = 2(a-\beta)/S \tag{8.5.5}$$

The final power level, P_f, can be obtained in an analogous manner. From Eqs. (8.2.5) and (8.5.4),

$$P_f \cong \frac{\Lambda \sum_1^6 \lambda_i (C_i')_f}{a - \beta} \tag{8.5.6}$$

An approximate value of $(C_i')_f$ can be found by integrating Eq. (8.2.6) over the entire burst. This yields

$$(C_i')_f \cong \frac{2\beta_i(a-\beta)}{\Lambda S} \tag{8.5.7}$$

Placing this equation into Eq. (8.5.6), the expression for the final power density becomes

$$P_f \cong \frac{2 \sum_1^6 \lambda_i \beta_i}{S} \tag{8.5.8}$$

There are a number of interesting observations that one can make on the previous set of equations. First, note from Eq. (8.5.4) that the final reactivity is a reflection of the initial reactivity around β. For example, if the initial reactivity is $1.50, the final reactivity is $.50; if the initial reactivity is $2.00, the final value is $0.00. It is perhaps surprising that the energy release, given by Eq. (8.5.5), is independent of the generation time. Moreover, it is almost startling that the final power density is independent of both the generation time and the step reactivity input.

The numerical solution to Eqs. (8.2.5) and (8.2.6) is shown in Figures 8.5.1 and 8.5.2 for reactivity steps of $1.50 and $2.00. The constants employed in these calculations are listed in Table 8.5.1. Observe that the previous predictions about the final power density and reactivity are correct. Also, these figures graphically demonstrate
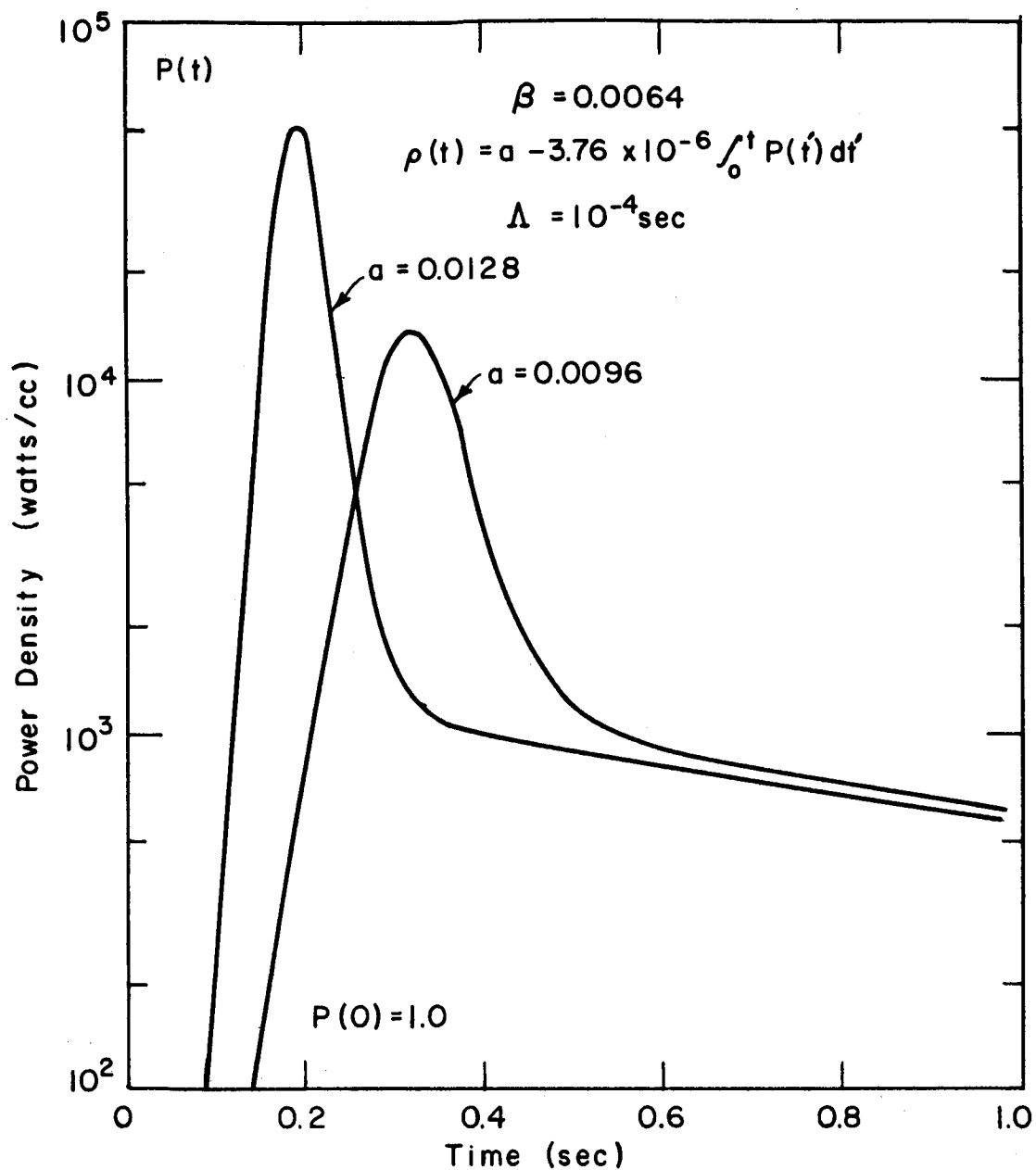
Figure 8.5.1. Power Profile for Step Reactivity Insertions.
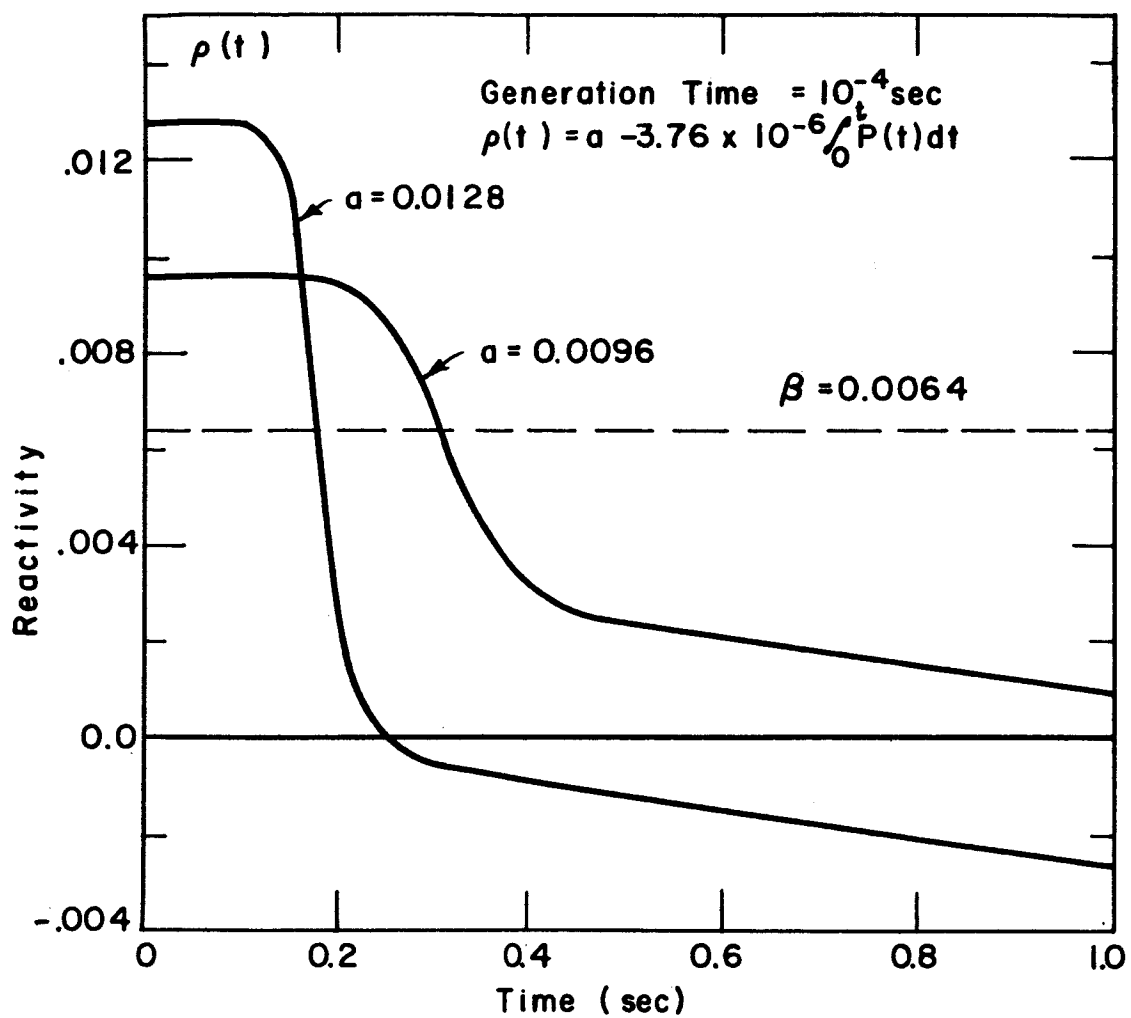
Figure 8.5. 2. Reactivity Variation for Step Reactivity Insertions.

Table 8.5.1. Data for Prompt Excursions Calculations

$$\beta = 0.0064$$

$$\Lambda = 10^{-4} \text{ sec}$$

$$\rho_o = 1.7 \times 10^3 \text{ kg/m}^3$$

$$C_p = 2 \times 10^3 \text{ joules/(kg-°K)}$$

$$\frac{d\rho}{dT} = -0.2 \text{¢/°K}$$

that reactivity steps of the order of two dollars cause a catastrophe of the first magnitude. For example, a two-dollar step causes the power density to reach the intolerable value of 56 Mw/liter in less than 0.2 seconds even when the initial power is only 1 watt/cc.

8.6 Reactor Behavior for Ramp Reactivity Insertions

In practice, reactivity variations usually have much more of a linear nature than a step nature. In this section we shall discuss reactor behavior for various linear reactivity insertions. Unfortunately, analytic approximations are rather cumbersome for ramp reactivity variations; hence we shall adhere to numerical results. The interested reader should see Soodak (33) for a complete discussion of many analytic approximations.

In one sense, ramp reactivity insertions are not as severe as step insertions. That is to say, there is a finite interval before the reactivity ramp reaches prompt critical. If the ramp is not too large, this time delay may permit the control system to partially negate the excursion. This general argument is demonstrated in Figure 8.6.1 for a ramp of one dollar per second. Observe that for approximately the first 0.8 seconds, the power variation is less than one order of magnitude.

In another sense, a ramp insertion is more dangerous than a step input. In the previous section it was demonstrated that a reactivity step caused a single power burst, followed by a slow decay in power. In contrast, a ramp insertion causes a series of power peaks, with an
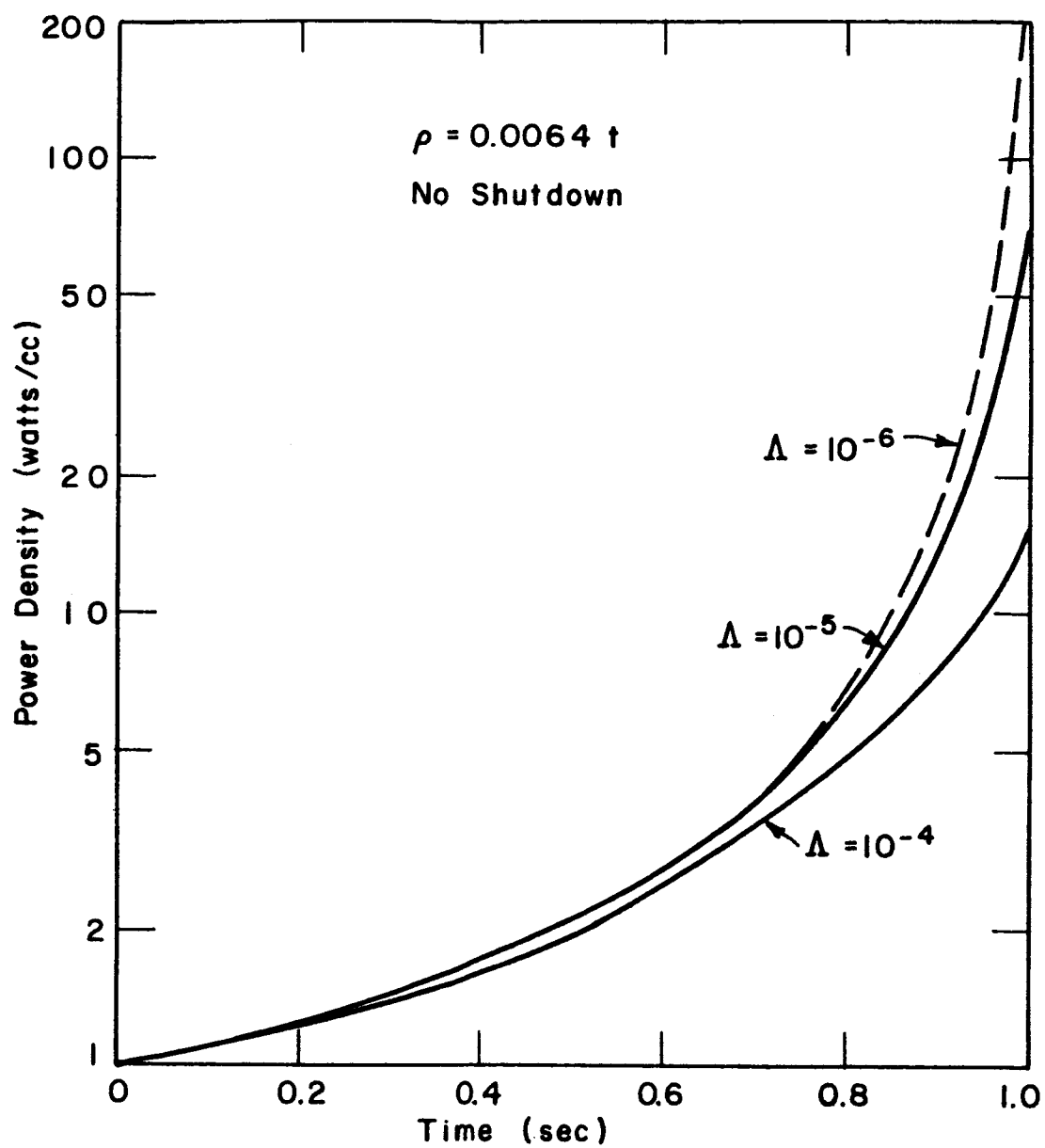
Figure 8.6.1. Reactor Response for a One Dollar per Second Reactivity Insertion.

appreciable energy release in each peak. This is shown in Figures 8.6.2 and 8.6.3 for a ten dollar per second ramp. However, at this point it should be stressed that the model employed is not strictly valid after the first one or two peaks. Many other variables enter the picture which are not included in the model, such as energy loss to coolant and control system feedback.

A few more observations can be made on Figure 8.6.2. As one would expect, a decrease in the generation time causes the initial burst to occur quicker and the oscillations to be damped out faster. But the energy release in the initial burst is greater for longer generation times.

From Eq. (8.3.1), the energy release can be expressed as

$$E = \frac{bt - \rho(t)}{S} \tag{8.6.1}$$

Hence one would expect the energy release to vary roughly as the reciprocal of the shutdown coefficient. Figure 8.6.4 shows that this is indeed the case. It is also clear from this figure that a change in the shutdown coefficient alters the position of the power peaks, but the effect is small.

8.7 Observations

Fundamentally, the prompt critical excursions discussed in this chapter are large because the shutdown coefficient for graphite moderated rocket reactors is rather small. From an accident analysis viewpoint, of course, it would be highly desirable to have a large shutdown coefficient. However, a rocket reactor with a large shutdown coefficient will also have an excessive reactivity variation during startup. In other words, one must accept a rather small shutdown coefficient in order to avoid excessive reactivity variations during normal startup.

It is clear from the results of this chapter that reactivities appreciably above prompt critical should be strictly avoided. This implies that the control system must be both fast and sensitive in order to counterbalance an inadvertent insertion of liquid hydrogen in the core.
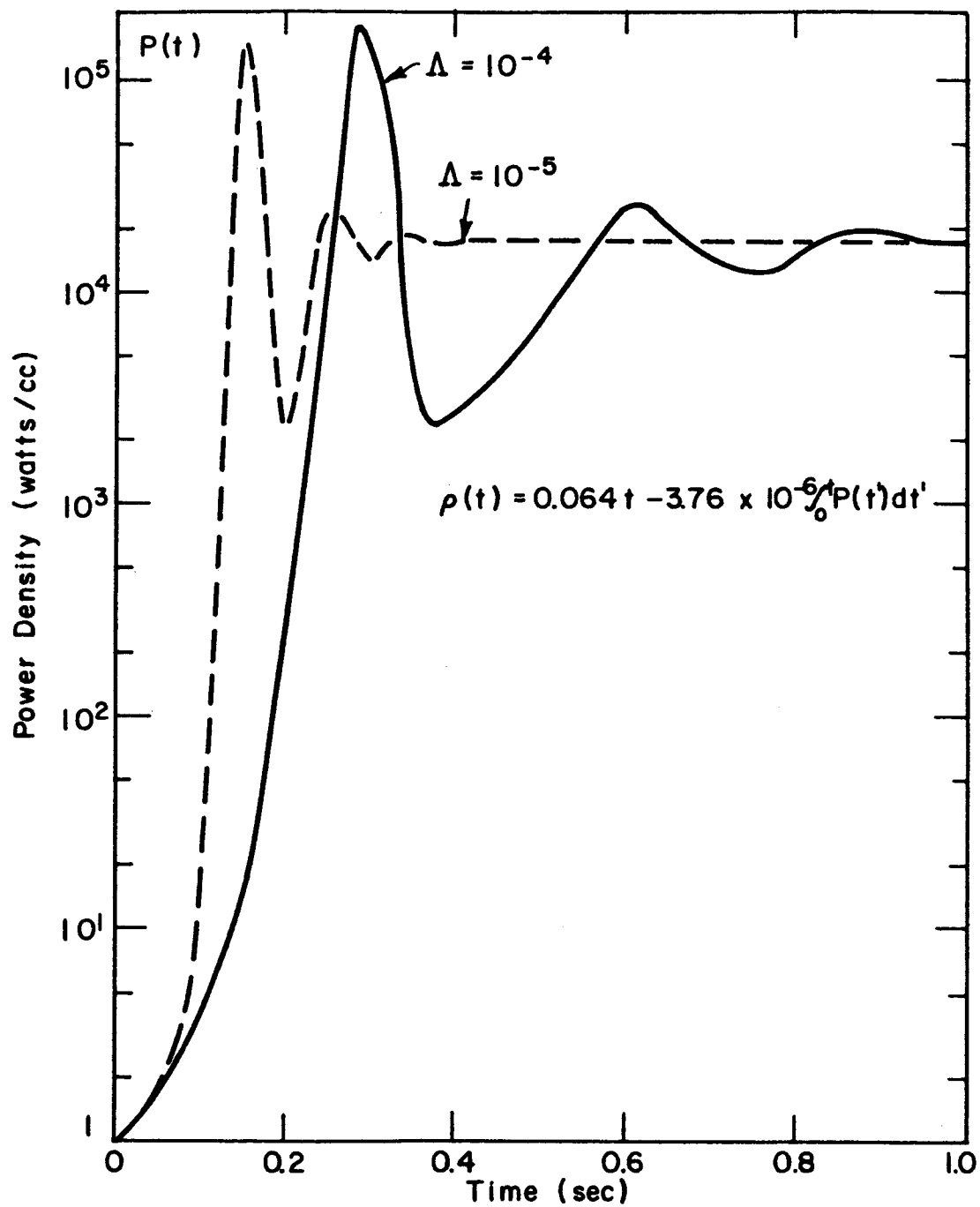
Figure 8.6.2. Effect of Generation Time on Burst Profile.

$$\rho(t) = 0.064 - 3.76 \times 10^{-6} \int_0^t P(t') \, dt'$$

$$\beta = 0.0064$$
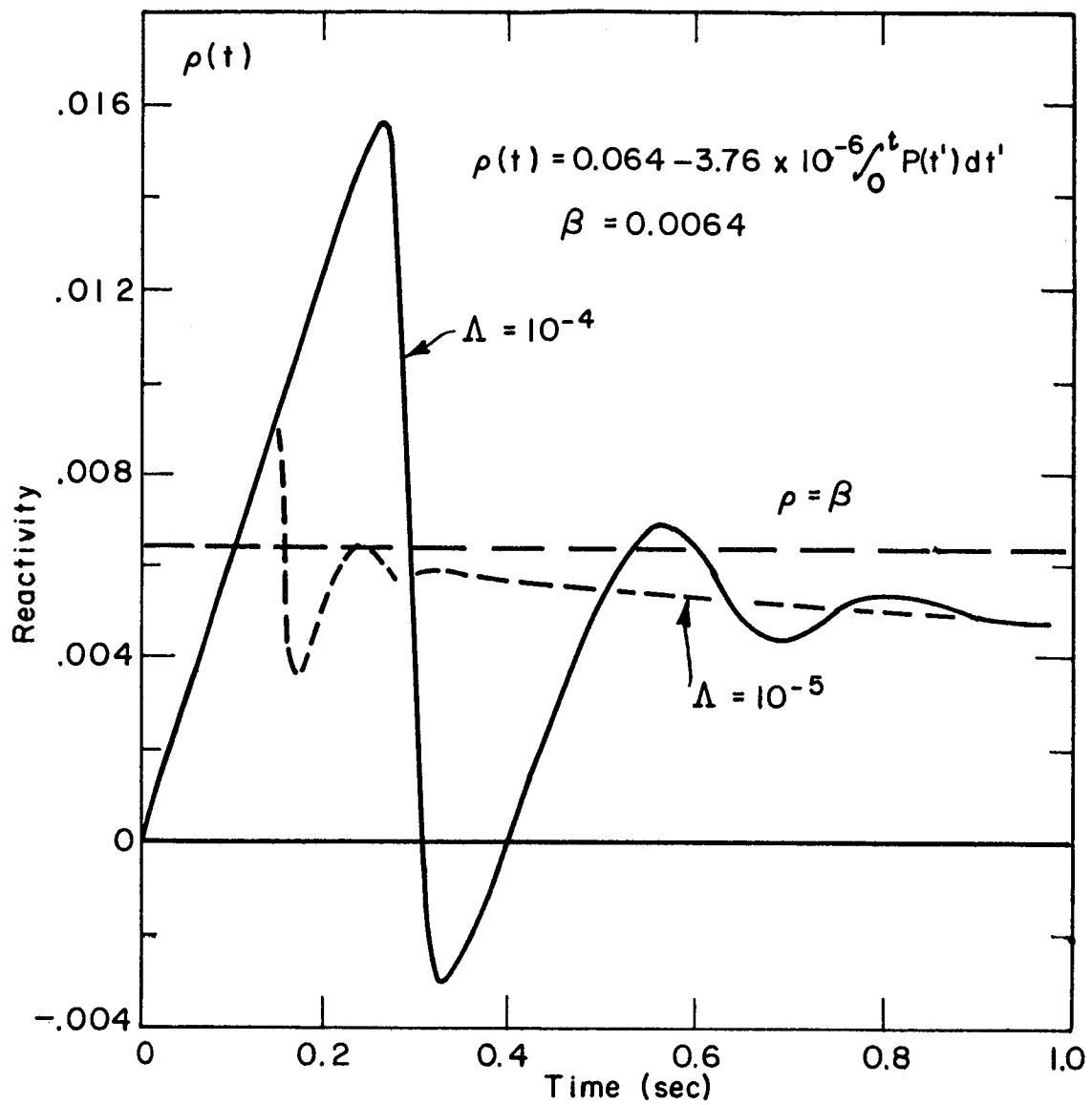
Figure 8.6.3. Reactivity Variation for a Ten Dollar Per Second Reactivity Insertion.
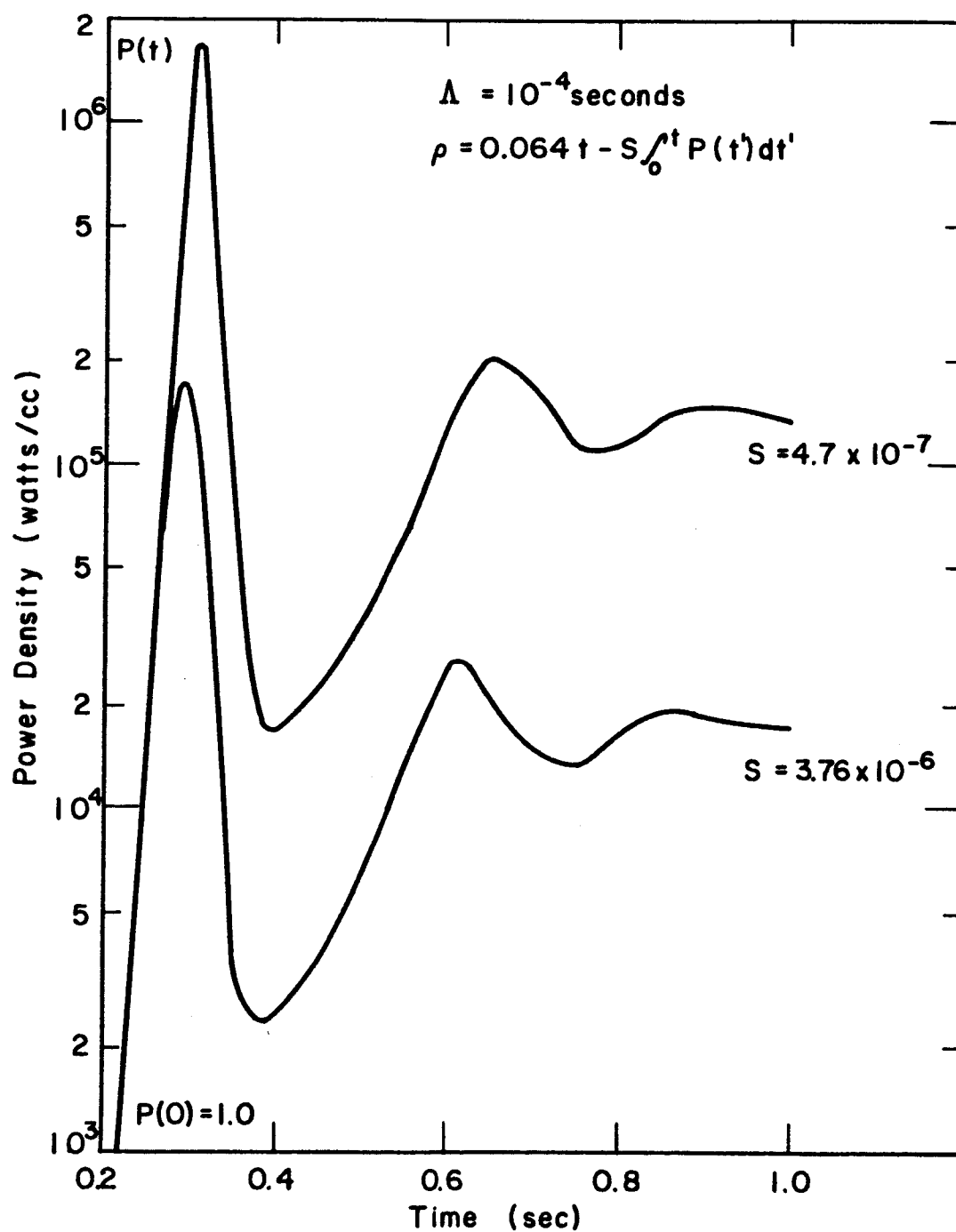
Figure 8.6.4. Reactor Behavior for Various Shutdown
Coefficients.

IX. CONCLUSIONS

In summarizing one's work, it is always tempting to draw conclusions which overlap the actual area of investigation. In this section we will merely point out the problem areas which appear rather serious. The final judgment on the feasibility of thermal nuclear rockets will be left for other investigators.

First, it is of paramount importance to rigorously prevent an excessive amount of cold hydrogen from entering the core during startup. An event of this nature would lead to a prompt critical burst too rapid to control in either a small or large nuclear rocket.

Excluding the above problem, no serious nuclear difficulties were found for the startup of small, intermediate spectrum ($C/U = 125 - 250$) nuclear rockets. Essentially, these small cores pose few problems because:

1) Changes in core temperature have very little effect on reactivity.
2) A normal amount of hydrogen does not induce an excessive reactivity variation.
3) The external control rods can easily supply the reactivity necessary for startup with a wide error margin.

Larger, more thermal cores ($C/U \cong 2500$), were found to be quite sensitive to changes in hydrogen density and core temperature. Because hydrogen density and core temperature vary rapidly during startup, large reactivity fluctuations are induced in thermal cores. These large reactivity variations might be permissible if the control system has sufficient reactivity control to quickly override all unwanted reactivity changes. However, as one might expect, the external control rods in large thermal cores were found to be worth considerably less than the external rods in intermediate cores.

The effect of temperature and hydrogen on reactivity can be reduced by placing a thermal poison in the core, but this procedure has the adverse side effect of reducing the worth of the external control rods by reducing the neutron leakage. It therefore appears that external control of large thermal cores is, at best, marginal.

X. SUGGESTIONS FOR FURTHER WORK

10.1 Introduction

Five suggestions for possible research topics are listed on the following pages. These topics are in the general area of nuclear rockets, but are not confined to nuclear rocket startup.

10.2 External Control Rods

The method put forth in this thesis for estimating external rod worth is rapid, but very crude. On the other hand, a detailed two-dimensional, multigroup calculation involves considerable computer time. This is especially true in view of the fact that pronounced flux depressions are present in the poison region. Perhaps there exists a reasonably fast computational model with sufficient accuracy for survey calculations lying somewhere between these two extremes.

In connection with the above study, it might be of interest to investigate the relative merit of different control poisons (e.g., boron, hafnium, cadmium).

10.3 Other Methods of Reactivity Control

In order to obtain greater reactivity control, large cores may require additional means of control. An obvious method would be to use internal poison rods. A more sophisticated approach might consist of adding a thermal poison to the hydrogen coolant before it enters the core. Note that such a scheme has the great virtue of instantaneously negating the large hydrogen reactivity worth.

10.4 Xenon and Samarium Poison

Because nuclear rockets have extremely high power densities, fission poisons build up rapidly. It appears conceivable that fission poisons could cause considerable trouble in a large, thermal nuclear

rocket. A complete treatment of this problem should include both an estimate of the absolute poison and an analysis of the possibility of severe xenon oscillation.

10.5 Core-Reflector Interface Problems

The thermal flux in a nuclear rocket has a large gradient in the vicinity of the core-reflector interface. This, of course, is caused by the large variation in material properties between the core and reflector. It might be of interest to see how well a diffusion theory model handles such a system by comparing the results of diffusion and transport theory calculations.

10.6 Space Dependent Reactor Kinetics

In the last few years there has been considerable interest in the validity of the space independent reactor dynamics equations. A comparison of nuclear rocket startup using space dependent and independent kinetics models might be very interesting. In any event, nuclear rocket startup, which requires large reactivities and power variations, would furnish a practical test problem for a space dependent kinetics calculation.

APPENDIX A
THERMAL STRESS

A1. Introduction

One of the major factors to be reckoned with in designing rocket cores is thermal stress, which may limit power density, channel size, etc. In order to obtain a reasonable approximation to the limits imposed, the stress model described in the next section was set up.

A2. Mathematical Model

Assumptions:

1) Thermal stress in a large graphite matrix can be adequately approximated by considering only a "unit cell" which consists of one flow channel and surrounding graphite. See Figure A2.1.
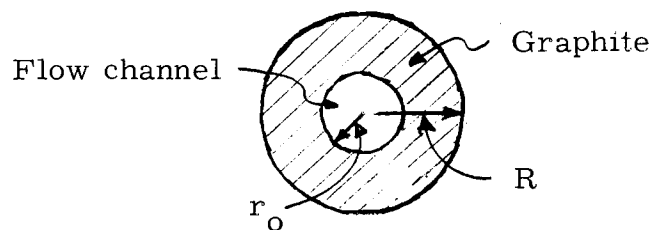
Figure A2.1. Unit Cell

The outer radius of the cell, R, is determined by the relationship

$$\text{void fraction} = \frac{\pi r_o^2}{\pi R^2} .$$

2) Flat power distribution in each cell. This should be an excellent assumption because the sizes involved are much smaller than the neutron mean free path.

Table A2.1. Symbol Table for Thermal Stress

E	Young's modulus (newtons/m^2)
H	Power density (w/m^3 of fuel)
k	Thermal conductivity (watts/m-°K)
r	Radius variable (m)
r_o	Inner radius of fuel element (m)
R	Outer radius of unit cell (m)
T	Temperature (°K)
α	Coefficient of thermal expansion (°K^{-1})
ν	Poisson's ratio
σ	Stress (newtons/$meter^2$)
$\sigma_{\theta\theta}$	Azimuthal stress (n/m^2)
σ_{rr}	Radial stress (n/m^2)
σ_{zz}	Axial stress (n/m^2)

3) $\left(\dfrac{\partial T}{\partial r}\right)_R = 0$. The symbols are defined in Table A2.1. This is merely a statement of the fact that all the heat is removed through the inner channel.

4) The core is free to expand in the axial and radial direction. Therefore, neglecting the pressure of hydrogen gas, a reasonable set of boundary conditions is $(\sigma_{rr})_{r_o} = (\sigma_{rr})_R = 0$.

5) Constant thermal properties. Thermal properties do vary significantly with temperature ([26]); yet the fractional variation is not very large if the range of temperature variation is only about 100°K at about 2500°K.

6) A time independent elastic thermal stress model is adequate. The stress relaxation rate is very high in a high temperature rocket core. However, for rapid thermal loading (startup $\cong$ 25 sec), the stress approaches the pessimistic value calculated by elastic theory.

From the well-known heat flow equation

$$k\nabla^2 T = k/r \frac{\partial}{\partial r}\left(r \frac{\partial T}{\partial r}\right) = -H \tag{A2.1}$$

the temperature rise, $T(r)$, in the graphite is given by

$$T(r) = \frac{H}{2k}\left[R^2 \ln(r/r_o) - 0.5(r^2 - r_o^2)\right] \tag{A2.2}$$

The equations for thermal stress are (<u>34</u>)

$$\frac{1}{r^2}\frac{d}{dr}\left(r^3 \frac{d\sigma_{rr}}{dr}\right) = -\frac{\alpha E}{1-\nu}\frac{dT}{dr} \tag{A2.3}$$

$$\sigma_{\theta\theta} = \sigma_{rr} + r\frac{d\sigma_{rr}}{dr} \tag{A2.4}$$

$$\sigma_{zz} = \nu(\sigma_{rr} + \sigma_{\theta\theta}) - \alpha ET - C \tag{A2.5}$$

The constant C is determined so that

$$\int_{r_o}^{R} r\sigma_{zz}(r)\,dr = 0 \tag{A2.6}$$

It can be shown that the final expression for axial stress is merely (<u>35</u>)

$$\sigma_{zz} = \sigma_{rr} + \sigma_{\theta\theta} \tag{A2.7}$$

The solution of Eq. (A2.3) for σ_{rr} with the previously stated boundary conditions and temperature distribution gives (<u>34</u>)

$$\sigma_{rr}(r) = \frac{\alpha EH}{16k(1-\nu)r^2}\left[\frac{r^2 - r_o^2}{R^2 - r_o^2}\left(4R^4 \ln\frac{R}{r_o} - 3R^4 + 4r_o^2 R^2 - r_o^4\right)\right.$$

$$\left. + 2R^2 r^2\left(1 - 2\ln\frac{r}{r_o}\right) - 2r_o^2(R^2 + r^2) + r^4 + r_o^4\right] \tag{A2.8}$$

From this expression, the azimuthal and axial stress can be easily obtained from Eqs. (A2.4) and (A2.7), respectively.

A3. <u>Results of Stress Calculations</u>

Numerical solutions to the above equations are shown on the following pages. The constants used in these calculations are given

Table A3.1. Thermal Stress Constants

$E = 6.8 \times 10^9$ newtons/meter^2 (10^6 psi)

$\alpha = 10^{-5}$ °K^{-1}

$\nu = 0.25$

$k = 34.4$ (watts/m-°K)

$H = 1.75 \times 10^6$ watts/liter

in Table A3.1. Note that the stress is a linear or inverse function of α, E, H, and k; hence if other constants are used, the resulting stress can be obtained by merely multiplying by the appropriate ratio.

Figure A3.1 gives the radial distribution of $\sigma_{rr}(r)$, $\sigma_{\theta\theta}(r)$ and $\sigma_{zz}(r)$. Note that the axial stress is largest and that its peak occurs at the inside radius. Physically, this results from the fact that the inside region of the tube is relatively cold; hence it tends to contract relative to the outside portion of the tube. From Figures A3.2 and A3.3, it can be seen that if one uses a void fraction of 0.3 and a channel radius of 0.125 cm (which you might wish to do for fluid flow reasons), the maximum axial stress (2.2×10^6 n/m^2) and temperature rise (32°K) are rather low. The tensile breaking strength of graphite is roughly 2×10^7 n/m^2 (26), which is 10 times larger than the stress in the above example. If the above estimate of tensile strength is correct, it appears that thermal stress in the fuel is not of critical importance for power densities in the range of 2 Mw/liter and channel diameters in the region of 0.25 cm.
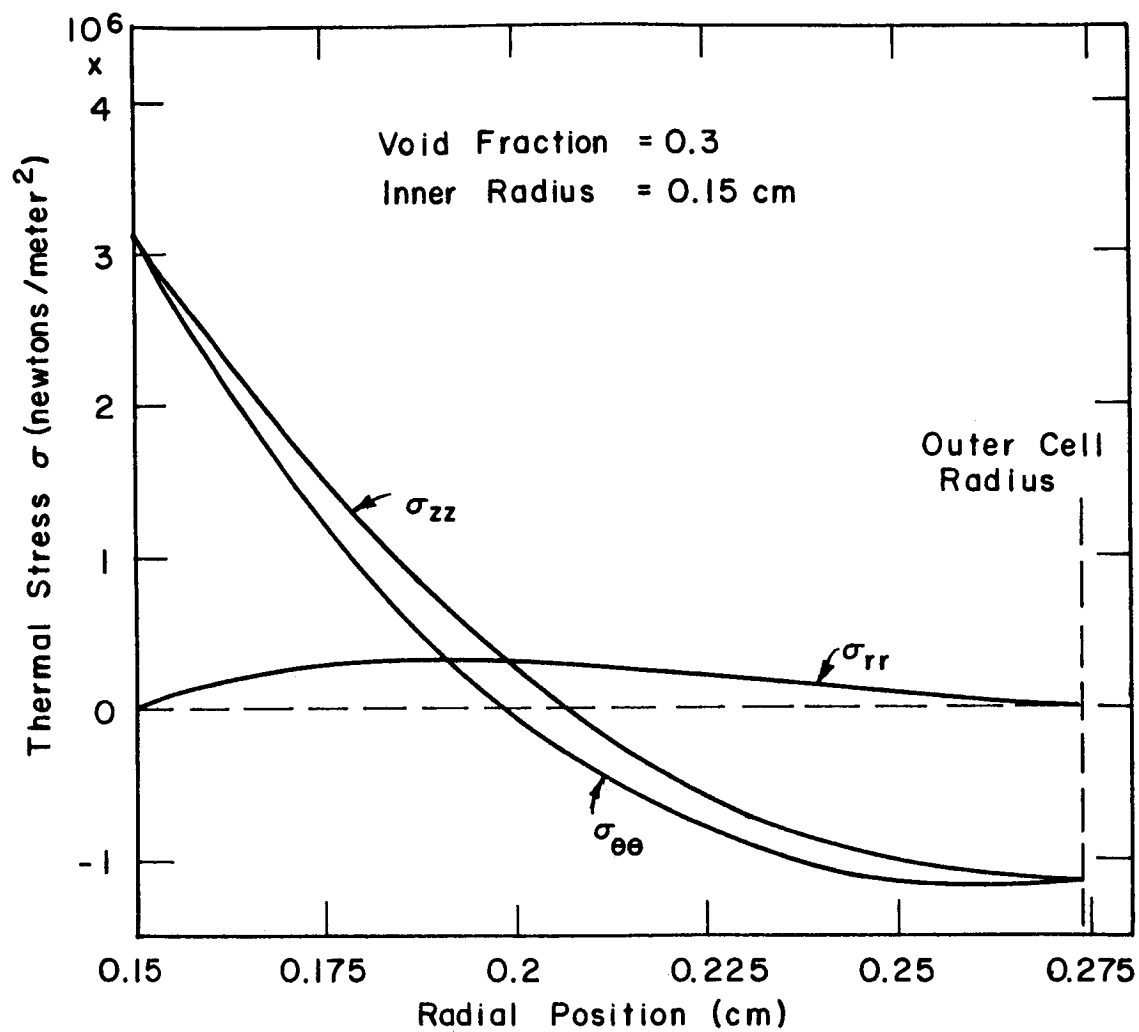
Figure A3.I. Stress Distribution in Unit Cell.
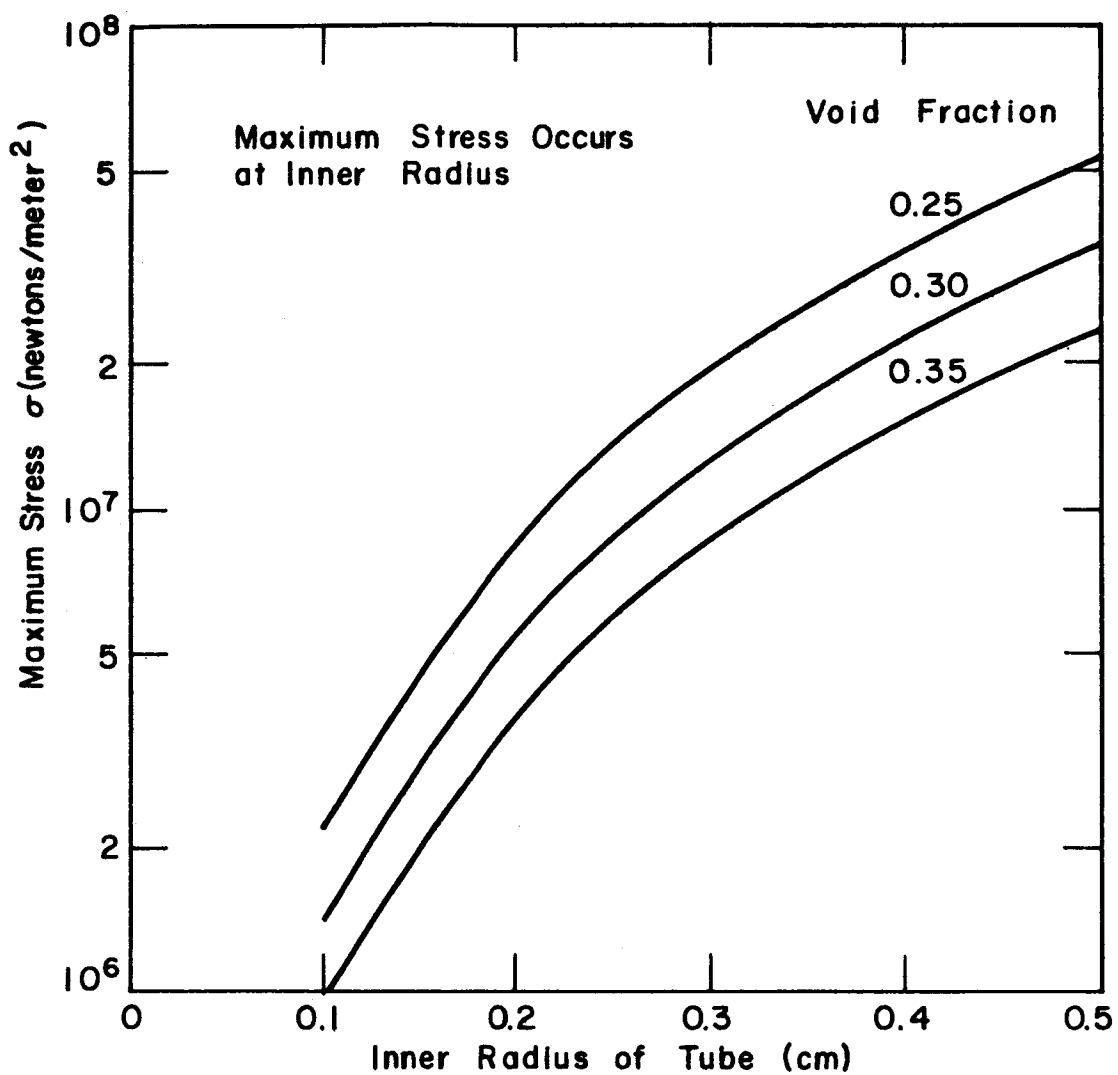
Figure A3.2. Maximum Thermal Stress in Unit Cell.
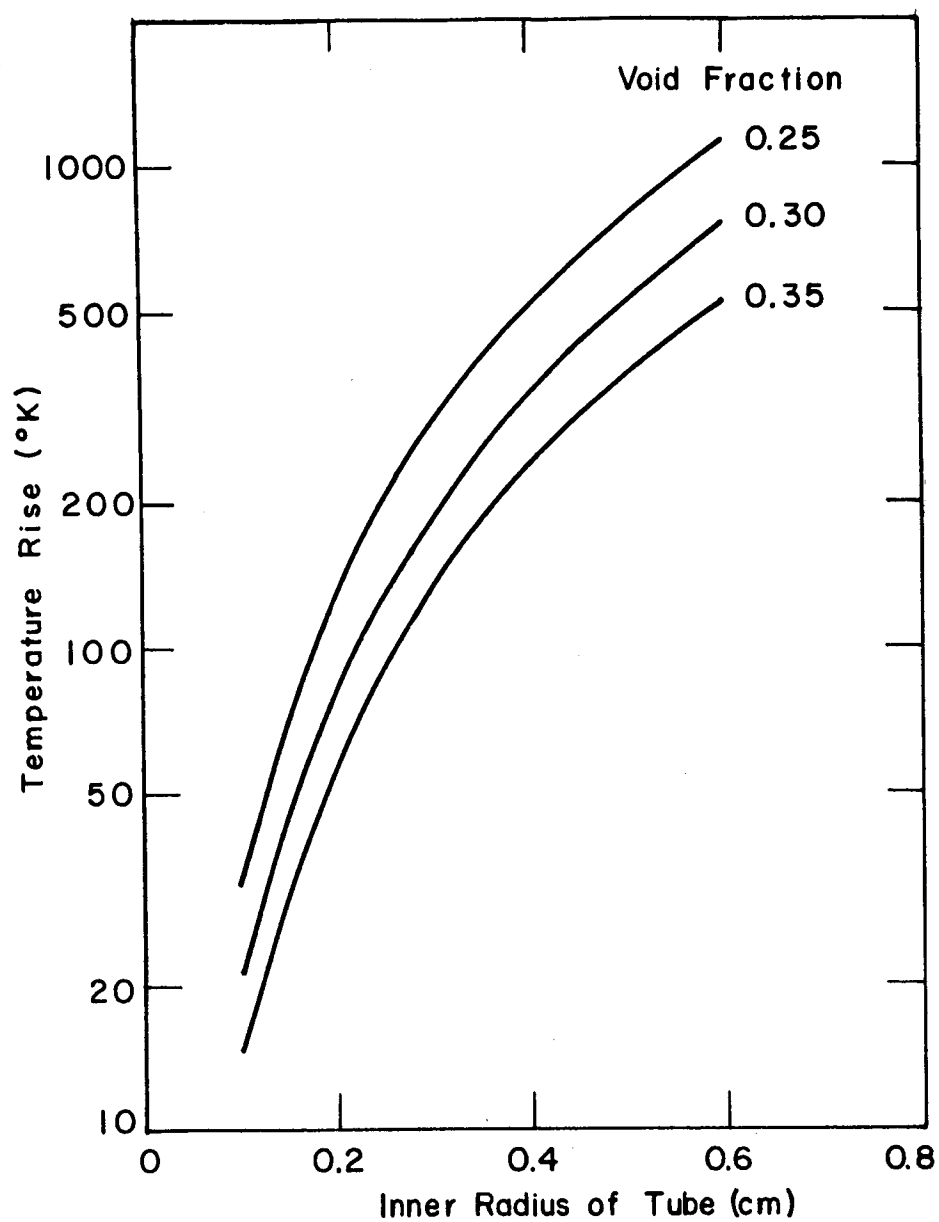
Figure A3.3. Maximum Temperature Rise in Unit Cell.

APPENDIX B
PARAMETRIC STUDY USING SIMPLIFIED FLUID FLOW EQUATIONS

B1. Objective

In order to obtain a rough feeling for the sensitivity of the fluid flow and heat transfer equations to the various core parameters, such as channel diameter, core length, etc., a parametric investigation was performed using a simplified fluid flow model. The equations comprising this model shall be listed, but not derived. A thorough discussion is given in the Course Notes for Course Number 22.27 at M.I.T.(36).

B2. Major Assumptions

The mathematical model is based on the following assumptions:

1) Steady-state operation.
2) No radial dependence. That is to say, all variables are a function of axial position only.
3) Flat power distribution (i.e., $H(x) = H_o$).
4) Constant hydrogen heat capacity (C_p) and heat capacity ratio (γ).
5) Hydrogen obeys perfect gas law.
6) Reynolds Analogy valid approximation (27).
7) Entrance Mach Number much less than unity.
8) The product of fluid velocity and friction factor increases linearly from core entrance to core exit.

Perhaps the largest error is introduced by assuming a flat power distribution, although the error introduced by other assumptions is also significant. In particular, the assumption of constant heat capacity is of questionable validity because the heat capacity varies by a factor of approximately 1.4 over the temperature range of interest (26).

Considering the severity of these assumptions, the model should not be expected to yield precise numerical results. However, the general behavior and sensitivity of the system should be adequately portrayed by this model.

B3. Mathematics of Fluid Flow Model

A schematic diagram of a rocket core is shown in Figure B3.1. Subscripts 1 and 2 designate the entrance and the exit region, respectively.
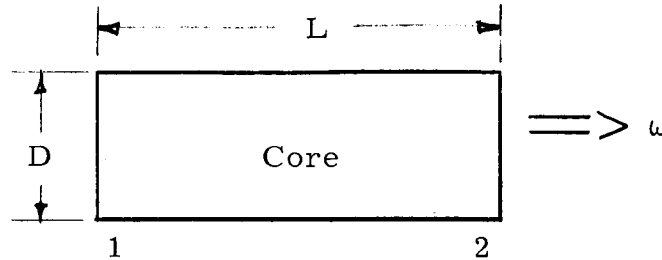
Figure B3.1. Schematic Diagram of Core

For a given core configuration, flow rate, entrance temperature and pressure, the entrance Mach Number, M_1, can be found from the expression

$$M_1 = \frac{\omega}{AP_{01}} \sqrt{\frac{RT_{01}}{\gamma \underline{M}}} \tag{B3.1}$$

where M_1 is assumed to be much less than unity. All symbols are defined in Table B3.1. If the exit stagnation temperature, T_{02}, is known, the exit Mach Number can now be computed using the implicit equation

$$M_2^2 = M_1^2 \left(\frac{T_{02}}{T_{01}}\right) \frac{\left[1+\gamma M_2^2(1+f_2 L/d)\right]^2}{1 + \frac{\gamma - 1}{2} M_2^2} \tag{B3.2}$$

where the exit friction factor, f_2, is found using the approximation

$$f = 0.046/(Re)^{0.2} \tag{B3.3}$$

Table B3.1. Symbols for Parametric Equations

A	total void area (m^2)
C_p	heat capacity of hydrogen (joules/kg-°K)
D	diameter of core (m)
d	diameter of fluid flow channel (m)
f	friction factor
L	length of core (m)
M	Mach Number
$\underline{M}$	molecular weight of gas (kg/kg-mole)
P	pressure (n/m^2)
P_0	stagnation pressure (n/m^2)
R	universal gas constant (joules/(kg-mole-°K))
Re	Reynolds number
T	temperature of hydrogen (°K)
T_0	stagnation temperature of hydrogen (°K)
T_w	wall temperature (°K)
ω	flow rate (kg/sec)
γ	gas constant for hydrogen (C_p/C_v)
ρ	density of hydrogen (kg/m^3)

It should be remarked that Eq. (B3.2) is valid only when $T_{02} \gg T_{01}$, which is the region of interest.

Using the exit Mach Number computed by Eq. (B3.2), the exit stagnation pressure is obtained from the equation

$$P_{02} = P_{01} \frac{\left[1 + \frac{\gamma-1}{2} M_2^2\right]^{\frac{\gamma}{\gamma-1}}}{1 + \gamma M_2^2(1+f_2 L/d)} \tag{B3.4}$$

The only remaining unknown variable is the maximum wall temperature, T_w. Using the Reynolds Analogy between heat and momentum transfer, it can be shown that

$$T_w = T_{02} + (T_{02}-T_{01}) \frac{2}{4f_2 L/d} \tag{B3.5}$$

The maximum wall temperature will obviously occur at the core exit because the power density is assumed to be spatially independent.

Using the fact that T_{02} is much greater than T_0 for all practical systems, it can be seen from Eq. (B3.5) that T_w is roughly a linear function of T_{02}. Therefore, a very effective but costly procedure for decreasing the wall temperature is merely to decrease the exit gas temperature. More will be said along these lines in the next section.

B4. Results and Observations

For all calculations, the following parameters are assumed fixed:
1) Flow rate
2) Inlet pressure
3) Inlet temperature
4) Exit stagnation temperature

Note that for a given core configuration (i.e., dimensions), the four parameters listed above completely determine the behavior of the system.

Figures B4.1 – B4.5 demonstrate how certain variables change as the core configuration is varied. All pertinent numerical information is listed in Table B4.1. The data is applicable to rocket systems with a thrust of approximately 445,000 newtons (100,000 lb).

Table B4.1. Data for Parametric Calculations

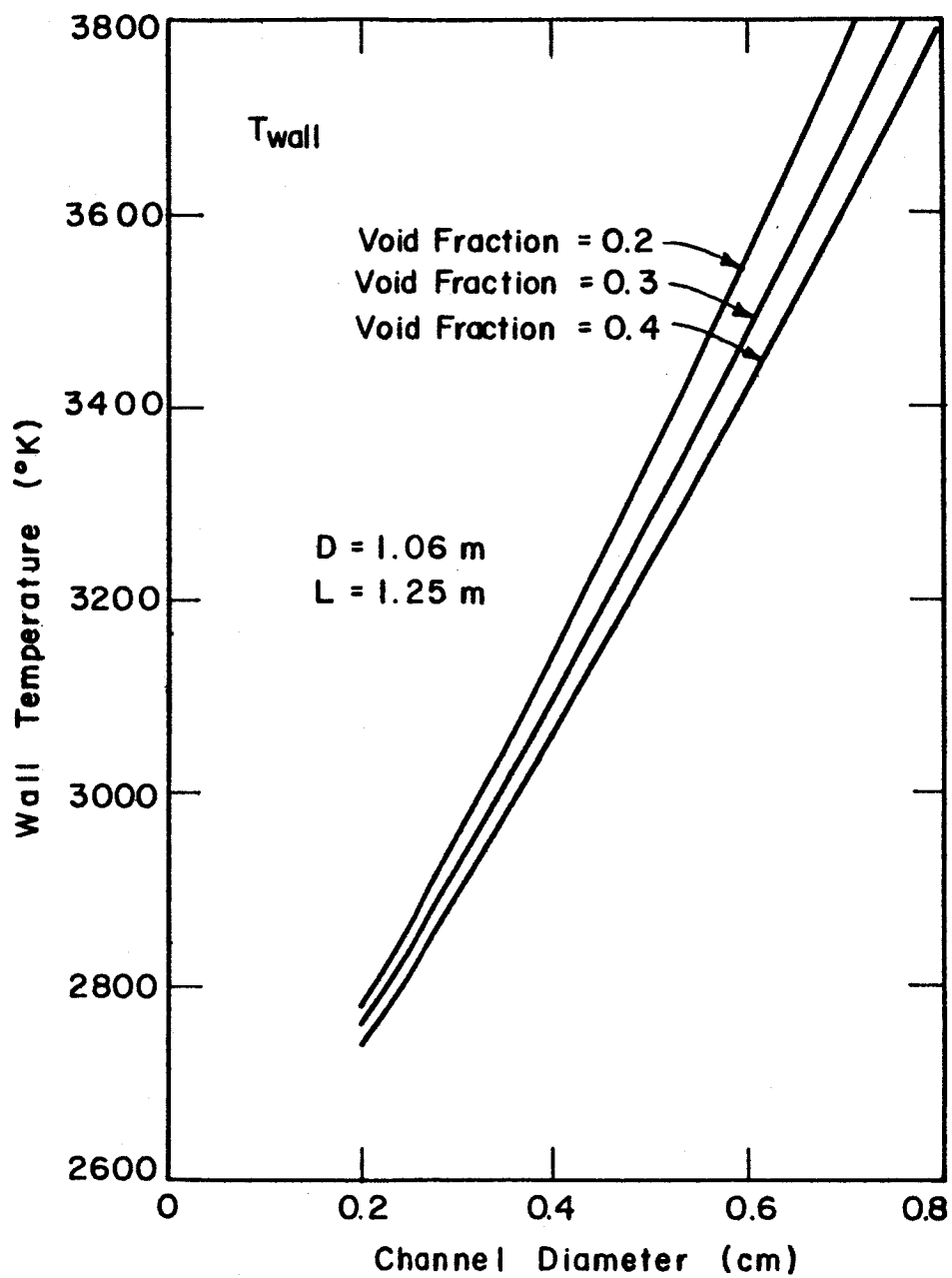|		
Flow rate	=	50 kg/sec
Entrance H_2 temperature	=	140°K
Exit H_2 stagnation temperature	=	2500°K (4500°R)
Inlet pressure	=	70 atm
Void fraction	=	0.3 (unless otherwise indicated)
Heat capacity of H_2	=	1.6×10^4 joules/(kg-°K)
Gas constant (γ) for H_2	=	1.35
Reactor power	=	1888 Mw

Figure B4.1. Maximum Wall Temperature as a Function
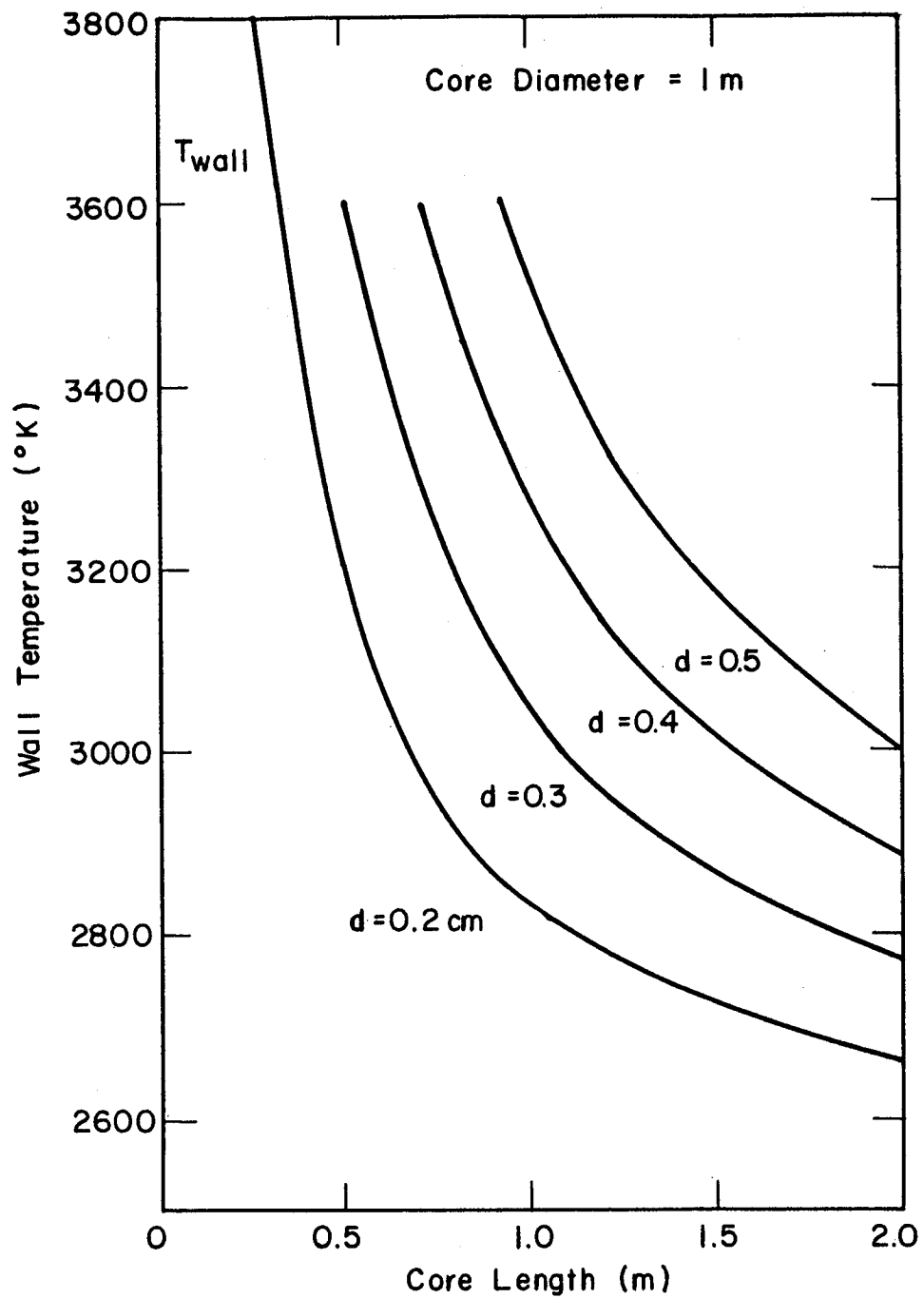of Channel Diameter.

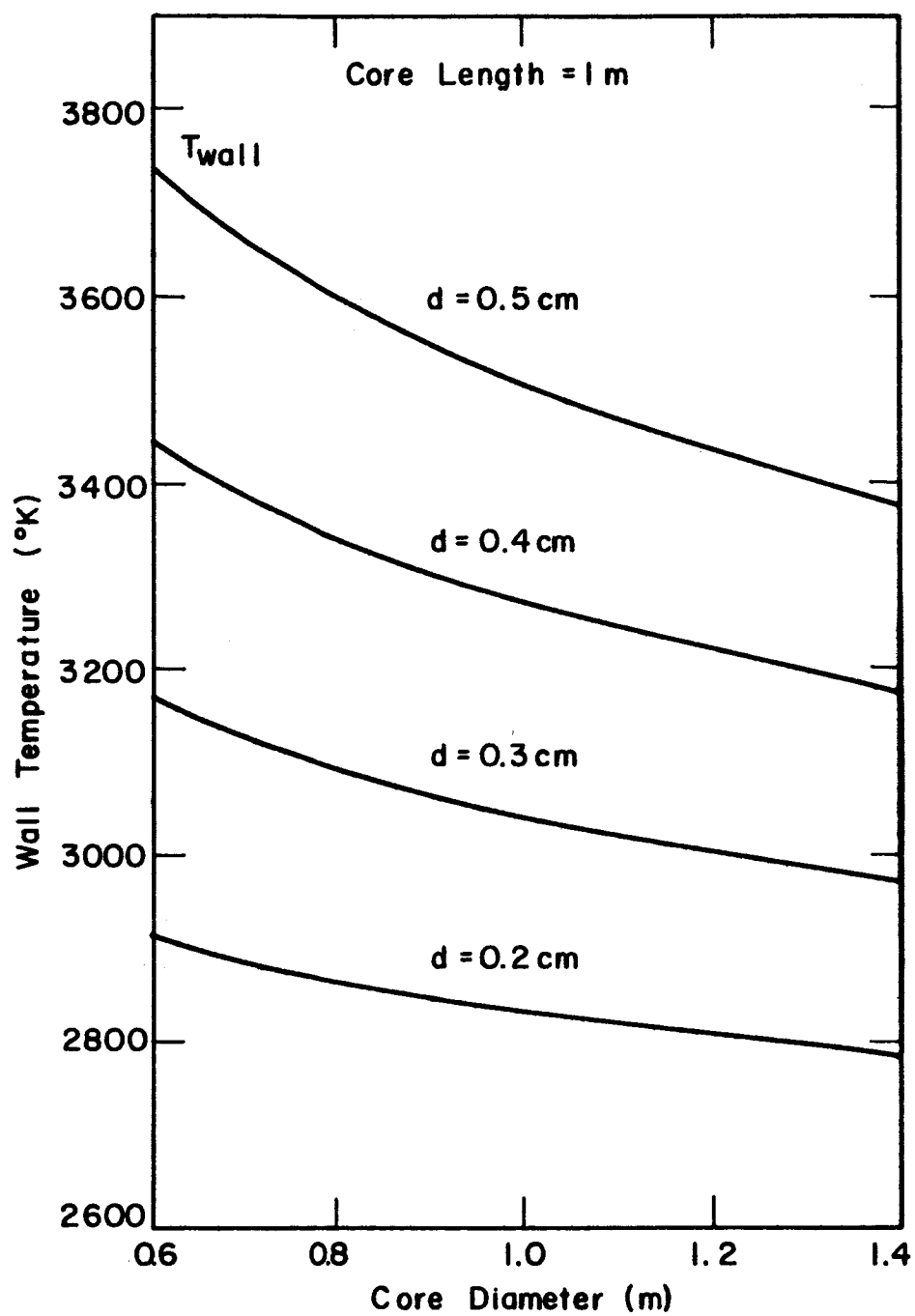Figure B4.2. Maximum Wall Temperature as a Function
of Core Length.

Figure B4.3. Maximum Wall Temperature as a Function of Core Diameter.
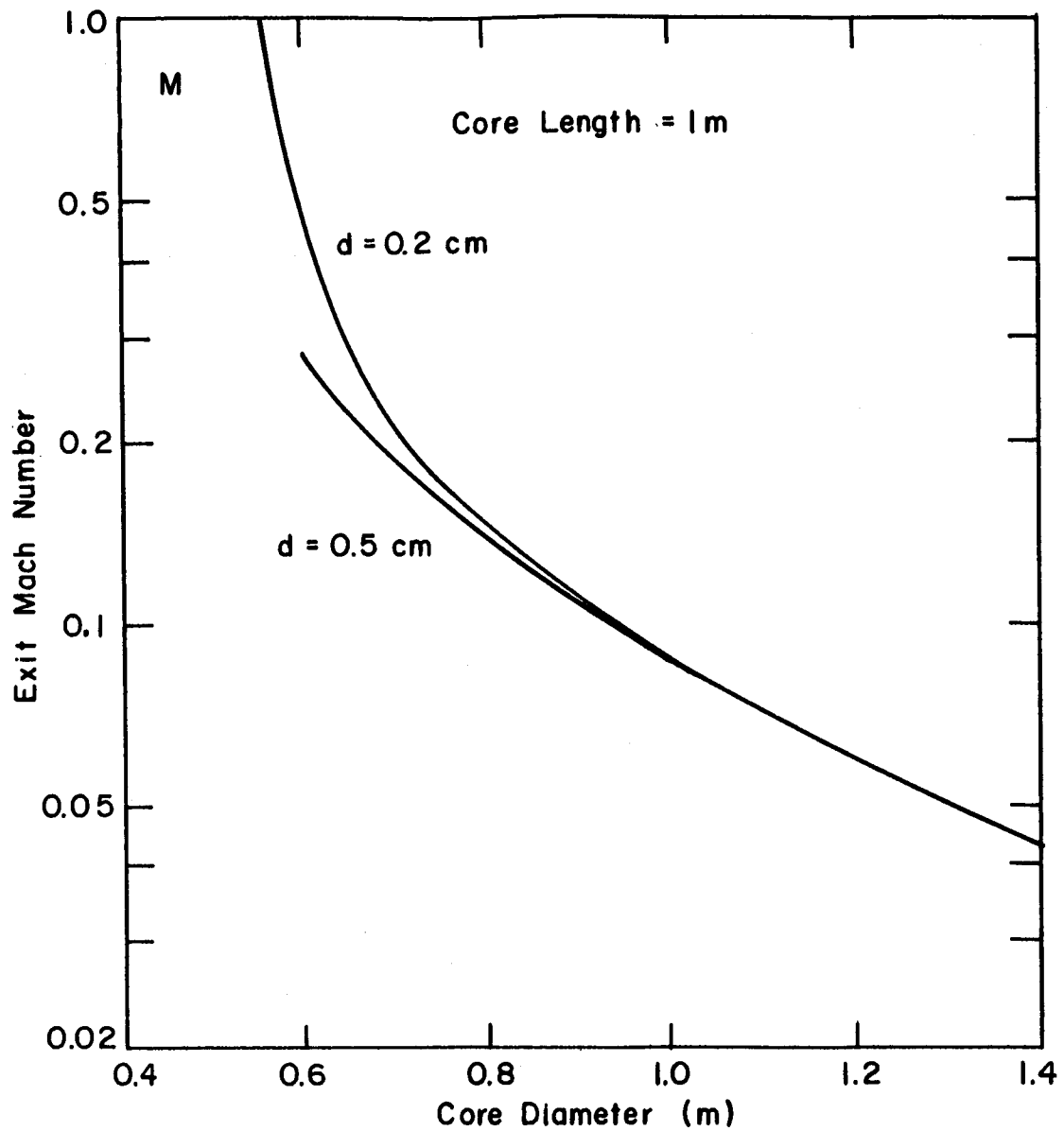
Figure B4.4. Exit Mach Number as a Function of Core Diameter.
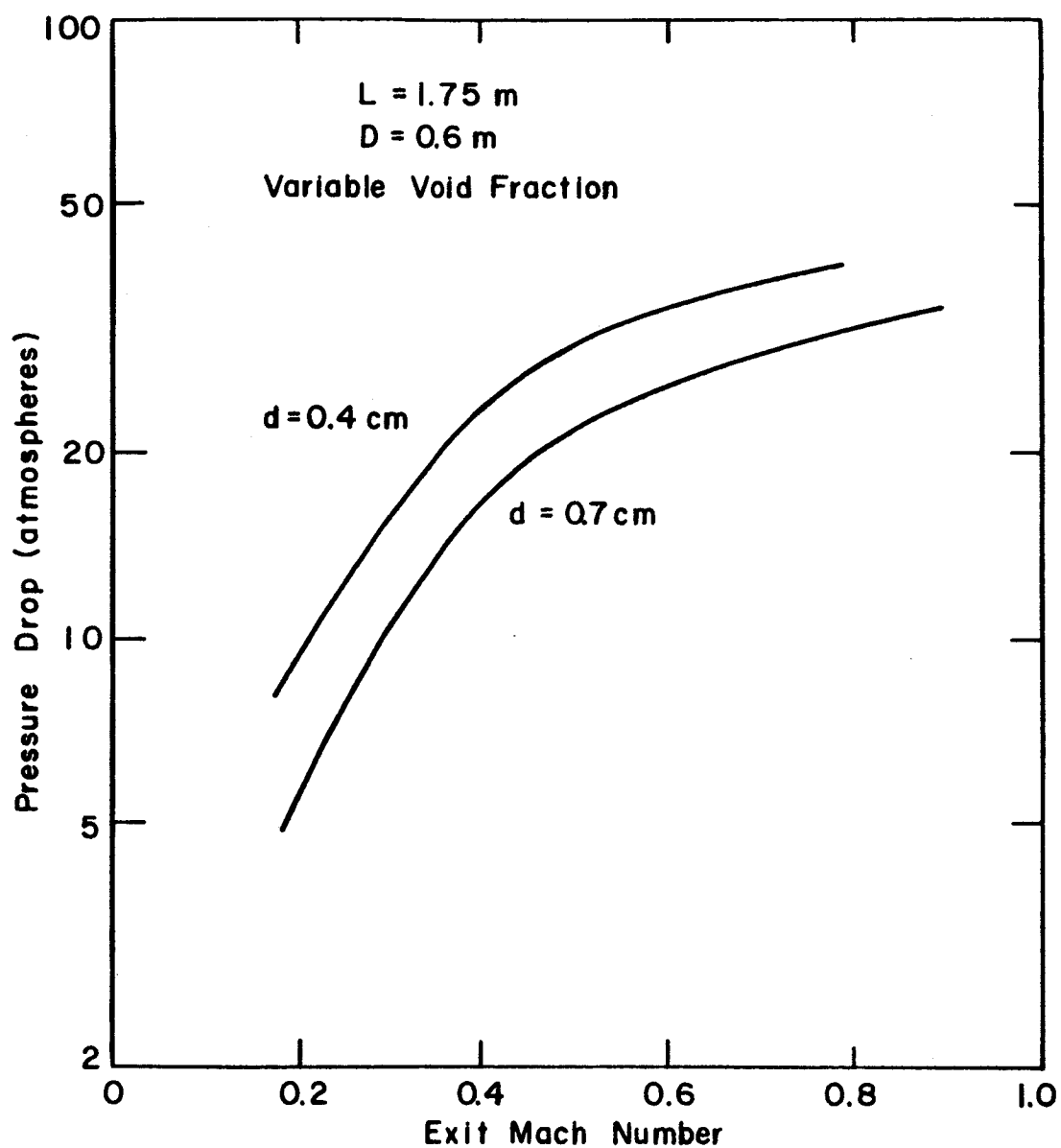
Figure B4.5. Pressure Drop as a Function of Exit Mach Number.

Perhaps the most striking result of this parametric study is shown in Figure B4.1, which gives the maximum wall temperature as a function of the channel diameter. Considering material limitations, it is clear that very small flow channels are absolutely essential in order to get the heat out of the core. For example, if the maximum permissible wall temperature is assumed to be 2900°K (5220°R), the channel diameter must be less than 0.3 cm.

By increasing the core length, the maximum wall temperature can be significantly decreased. This is demonstrated in Figure B4.2. However, the wall temperature is much more sensitive to channel size than to core length.

At first glance, the wall temperature might also be expected to significantly decrease with increasing core diameter for a constant flow rate and void fraction. Figure B4.3 shows that this variation is rather small. Essentially, the reason for this behavior is that the reduced flow per channel in the larger diameter cores causes the heat transfer coefficient to decrease.

For a given total flow rate, a decrease in the core diameter causes an increase in the entrance and exit Mach Numbers. This is pictured in Figure B4.4. Note, from Figure B4.5, that high exit Mach Numbers induce large pressure drops. This is especially true for exit Mach Numbers greater than about 0.2.

It is interesting to observe that for a constant exit Mach Number, or pressure drop, the flow rate can be increased by increasing the pressure. Mathematically,

$$M = \frac{v}{c} = \frac{v\rho}{c\rho} = \frac{w}{\rho A} \sqrt{\frac{M}{\gamma RT}} = \frac{w}{P} \cdot \frac{1}{A} \sqrt{\frac{RT}{\gamma M}} \qquad (B4.1)$$

Hence for a given Mach Number and temperature, the flow rate through the core is a linear function of the pressure.

APPENDIX C
FLUX TILTING

C1. Introduction

In the fluid flow model described in Chapter IV, the fuel and hydrogen temperature distributions were calculated under the assumption that the spatial power distribution does not vary with time. However, this assumption is not clearly valid because the properties of the core vary considerably with position during startup.

In order to assess the magnitude of flux variation, we shall employ a simple, one energy group, diffusion theory model in slab geometry. The spatial variation in nuclear properties shall be simulated by varying $\nu(x)$.

Assuming that the nuclear parameters D, Σ_a, and Σ_f are constant,

$$D\nabla^2\phi(x) + (\nu\Sigma_f - \Sigma_a)\,\phi(x) = 0 \tag{C1.1}$$

Letting $\nu = \nu_o(1 + 0.0064\,\delta k(x))$,

$$\nabla^2\phi(x) + \left[\frac{\nu_o(1 + 0.0064\,\delta k)\,\Sigma_f - \Sigma_a}{D}\right]\phi(x) = 0 \tag{C1.2}$$

where δk is the infinite medium reactivity variation in units of dollars.

C2. Results

Equation (C1.2) is solved numerically by the method of successive displacements for a given reactivity distribution, $\delta k(x)$. ν_o is varied to keep the system critical. The results are shown in Figures C2.1 - C2.2. All appropriate constants are listed in Table C2.1.
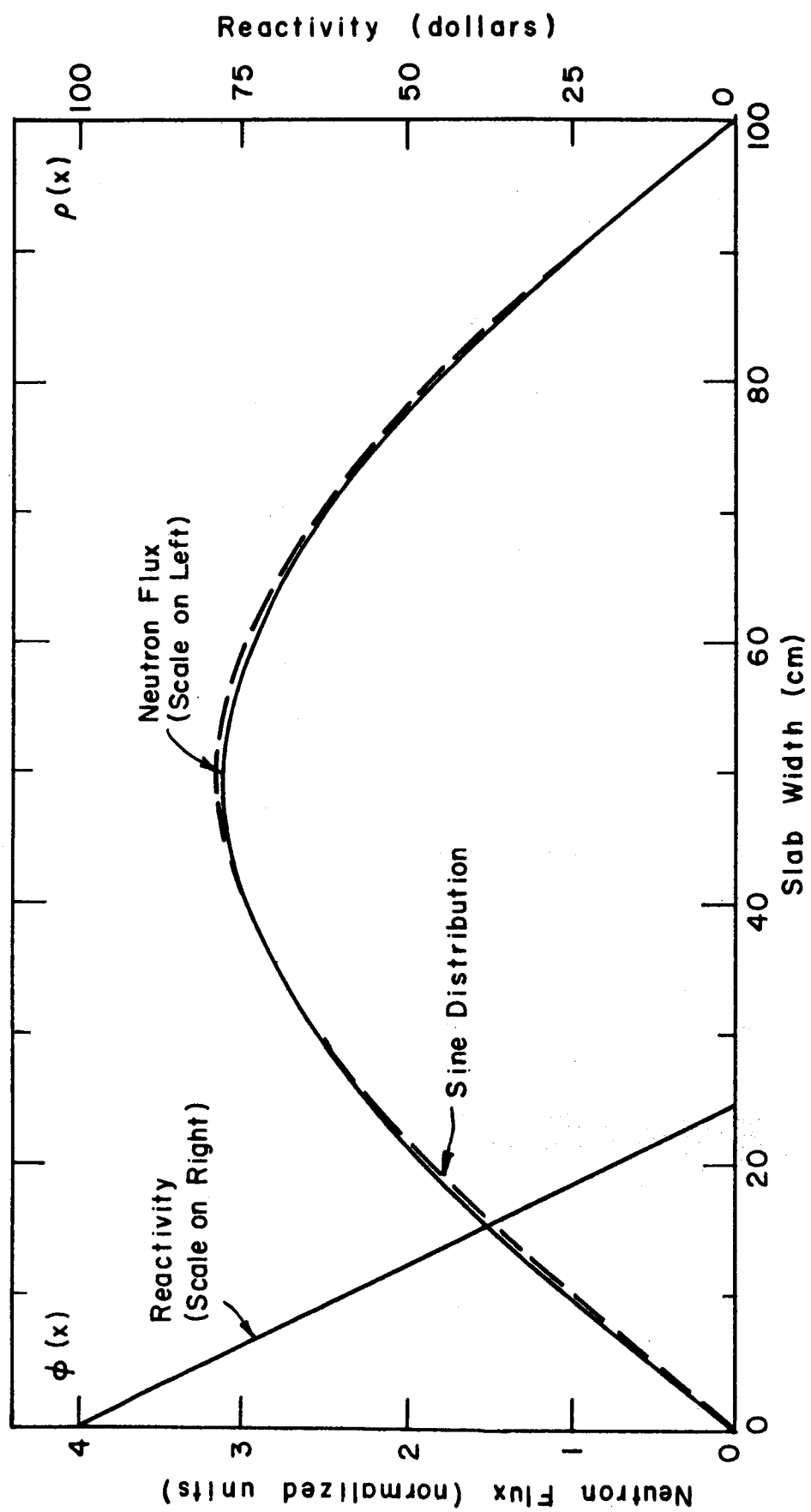
Figure C2.I. Effect of Reactivity Spike on Flux Shape.
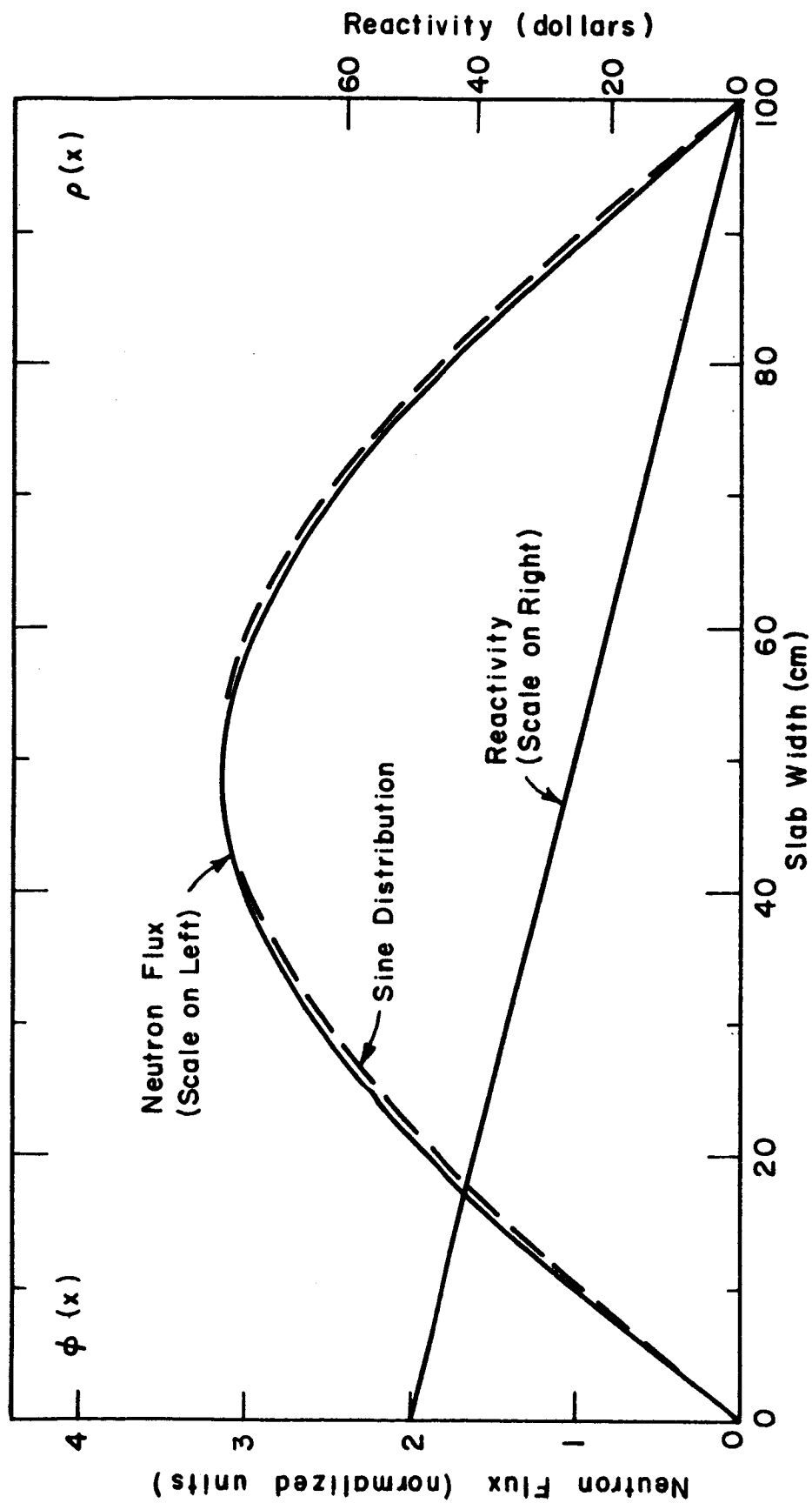
Figure C2.2. Effect of Space Dependent Cross Sections on Flux Shape.

Table C2.1. Data for Flux Tilt Investigation

$\Sigma_f = 0.0011 \text{ cm}^{-1}$ $D = 1.49 \text{ cm}$

$\Sigma_a = 0.00132 \text{ cm}^{-1}$ $L = 100 \text{ cm}$

$\phi(0) = \phi(L) = 0$

C3. Observations on Results

Although the spatial variation in reactivity is extremely large, the flux perturbation is not excessive. This indicates that the assumption of a time invariant spatial power distribution is probably permissible.

The model employed should simulate the effect of a temperature gradient relatively well. Temperature changes alter thermal group properties, which is in essence what is altered when $\delta k(x)$ is varied.

The effect of hydrogen is essentially a fast group phenomenon; hence the model is of questionable applicability. However, Plebuch has shown that the flux tilt caused by hydrogen is quite small (14).

APPENDIX D
PRECURSOR CONSTANTS IN THE KINETIC EQUATIONS

D1. Introduction

A number of kinetic models using 2 or 3 delayed neutron groups have been proposed for the study of nuclear rocket startup (37). The objective of this appendix is to delineate the effect of using less than six precursor groups in the kinetic equations.

D2. Choice of Parameters

There are numerous ways to reduce the six precursor group kinetic model to a fewer group model. The three most widely used methods are examined below.

Consider the kinetic equations in the form

$$\frac{dn}{dt} = \frac{\rho - \beta}{\Lambda} n + \sum_1^6 \lambda_i C_i \qquad (D2.1)$$

$$\frac{dC_i}{dt} = \frac{\beta_i n}{\Lambda} - \lambda_i C_i \qquad (D2.2)$$

where: Λ = generation time

ρ = reactivity

β_i = decay fraction for group i

β = total decay fraction

The well-known inhour formula can easily be shown to be

$$\frac{\rho}{\omega} = \Lambda + \sum_1^6 \frac{\beta_i}{\omega + \lambda_i} \qquad (D2.3)$$

where ω is the reciprocal of the period. For a one precursor group model, the inhour equation is simply

$$\frac{\rho}{\omega} = \Lambda + \frac{\overline{\beta}}{\omega + \overline{\lambda}} \qquad (D2.4)$$

144

where $\bar{\beta}$ and $\bar{\lambda}$ are the appropriate one group constants. It appears reasonable to demand that the one group model have the same asymptotic period as the six group model. Therefore, setting the right-hand side of Eq. (D2.3) equal to the right-hand side of Eq. (D2.4),

$$\frac{\bar{\beta}}{\omega + \bar{\lambda}} = \sum_1^6 \frac{\beta_i}{\omega + \lambda_i} \tag{D2.5}$$

$\bar{\beta}$ and $\bar{\lambda}$ can be easily obtained from the above equation in certain limiting cases.

D3. Large Reactivities ($\omega \gg \lambda_i$)

Expanding Eq. (D2.5) and keeping only constant and linear terms, we find

$$\bar{\beta}\left(1 - \frac{\bar{\lambda}}{\omega}\right) \cong \sum_1^6 \beta_i\left(1 - \frac{\lambda_i}{\omega}\right) \tag{D3.1}$$

$\bar{\beta}$ and $\bar{\lambda}$ are determined by matching first- and second-order terms in Eq. (D3.1). Therefore, the one group constants suitable for large burst calculations are:

$$\bar{\beta} = \sum_1^6 \beta_i \tag{D3.2}$$

$$\bar{\lambda} = \frac{\sum_1^6 \lambda_i \beta_i}{\sum_1^6 \beta_i} \tag{D3.3}$$

D4. Small Reactivities ($\omega \ll \lambda_i$)

Again, Eq. (D2.5) is expanded in a two-term power series. This yields the relationship

$$\frac{\bar{\beta}}{\bar{\lambda}}\left(1 - \frac{\omega}{\bar{\lambda}}\right) \cong \sum_1^6 \frac{\beta_i}{\lambda_i}\left(1 - \frac{\omega}{\lambda_i}\right) \tag{D4.1}$$

The one group constants for small reactivities are now obtained by matching corresponding terms in Eq. (D4.1). Therefore,

$$\bar{\beta} = \frac{\left[\sum\left(\frac{\beta_i}{\lambda_i}\right)\right]^2}{\sum\frac{\beta_i}{\lambda_i^2}} \tag{D4.2}$$

$$\bar{\lambda} = \frac{\sum\left(\frac{\beta_i}{\lambda_i}\right)}{\sum\left(\frac{\beta_i}{\lambda_i^2}\right)} \tag{D4.3}$$

where, for simplicity, the summation limits have been omitted.

D5. Intermediate Reactivities

In the case of large reactivities, it was assumed that $\omega \gg \lambda_i$; and for small reactivities it was assumed that $\omega \ll \lambda_i$. These restrictions are rather binding because the fastest precursor group has a half-life of 0.179 seconds (U-235), and the slowest group has a half-life of 54.5 seconds. What is needed is a one group model which is approximately valid over the entire frequency range. This can be obtained by requiring that Eq. (D2.5) be satisfied in the limits $\omega \to \infty$ and $\omega \to 0$. For $\omega \to \infty$, Eq. (D2.5) reduces to

$$\bar{\beta} = \sum \beta_i \tag{D5.1}$$

Setting $\omega = 0$ in Eq. (D2.5), and using the above value of $\bar{\beta}$,

$$\bar{\lambda} = \frac{\sum \beta_i}{\sum\left(\frac{\beta_i}{\lambda_i}\right)} \tag{D5.2}$$

D6. Characteristic Results

In order to get a feeling for the relative merits of the different schemes, the response in the time domain was computed for various reactivity insertions. The results are given in Figures D6.1 - D6.4. The precursor group constants employed in these calculations are given in Table D6.1. The six group constants were taken from Keepin (29).

The two and three group constants were computed in the same spirit as the one group constants. For the two group computation, the initial six groups were divided into two segments, each containing three groups. A one group approximation was then calculated for each segment. Likewise, the three group constants were obtained by dividing the initial six groups into three segments, and calculating a one group approximation for each segment.

D7. Conclusions

It is clear from the preceding graphs that a one group model gives poor results for moderate reactivity insertions. Notice from Figure D6.1 that the one fast group model is off by almost an order of magnitude after 10 seconds for a reactivity step of 50 cents. However, for very large bursts, such as the ten dollar per second reactivity ramp shown in Figure D6.4, a one fast group model yields excellent results.

A two group model is a substantial improvement over a one group model; yet the percentage error for moderate reactivity insertions can be rather large even in the two group model.

Perhaps the most important conclusion that can be drawn from these results is that accurate computations involving reactivities in the region of 50-100 cents require the use of three or more precursor groups. From a practical viewpoint, this is almost equivalent to recommending the use of a six precursor group model because three and six group models do not differ significantly in complexity.

Table D6.1. Precursor Constants for Uranium-235

	Large Reactivities	Intermediate Reactivities
1 Group	$\beta = 0.0064$	$\beta = 0.0064$
	$\lambda = 0.43525$	$\lambda = 0.07851$
2 Groups	$\beta_1 = 0.0028096$	$\beta_1 = 0.0028096$
	$\lambda_1 = 0.065727$	$\lambda_1 = 0.03875$
	$\beta_2 = 0.0035904$	$\beta_2 = 0.0035904$
	$\lambda_2 = 0.72441$	$\lambda_2 = 0.3984$
3 Groups	$\beta_1 = 0.0016064$	$\beta_1 = 0.0016064$
	$\lambda_1 = 0.02882$	$\lambda_1 = 0.02586$
	$\beta_2 = 0.003808$	$\beta_2 = 0.003808$
	$\lambda_2 = 0.24907$	$\lambda_2 = 0.2025$
	$\beta_3 = 0.0009856$	$\beta_3 = 0.0009856$
	$\lambda_3 = 1.817$	$\lambda_3 = 1.566$

- -

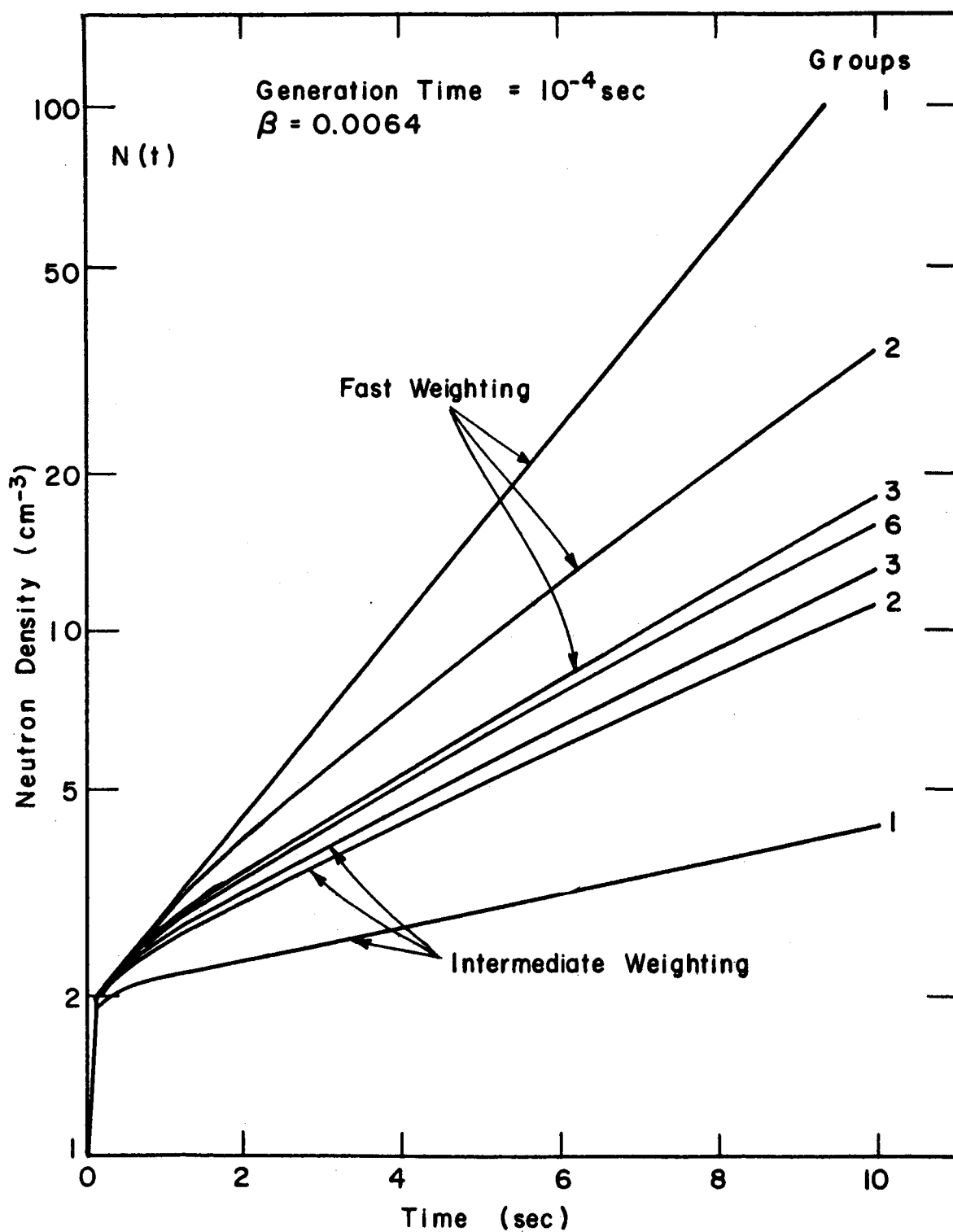|	Large Reactivities	Intermediate Reactivities
6 Groups (From Keepin (29))	$\beta_1 = 0.0002432$	$\lambda_1 = 0.0127$
	$\beta_2 = 0.0013632$	$\lambda_2 = 0.0317$
	$\beta_3 = 0.0012032$	$\lambda_3 = 0.115$
$\beta = .0064$	$\beta_4 = 0.0026048$	$\lambda_4 = 0.311$
	$\beta_5 = 0.0008192$	$\lambda_5 = 1.4$
	$\beta_6 = 0.0001664$	$\lambda_6 = 3.87$

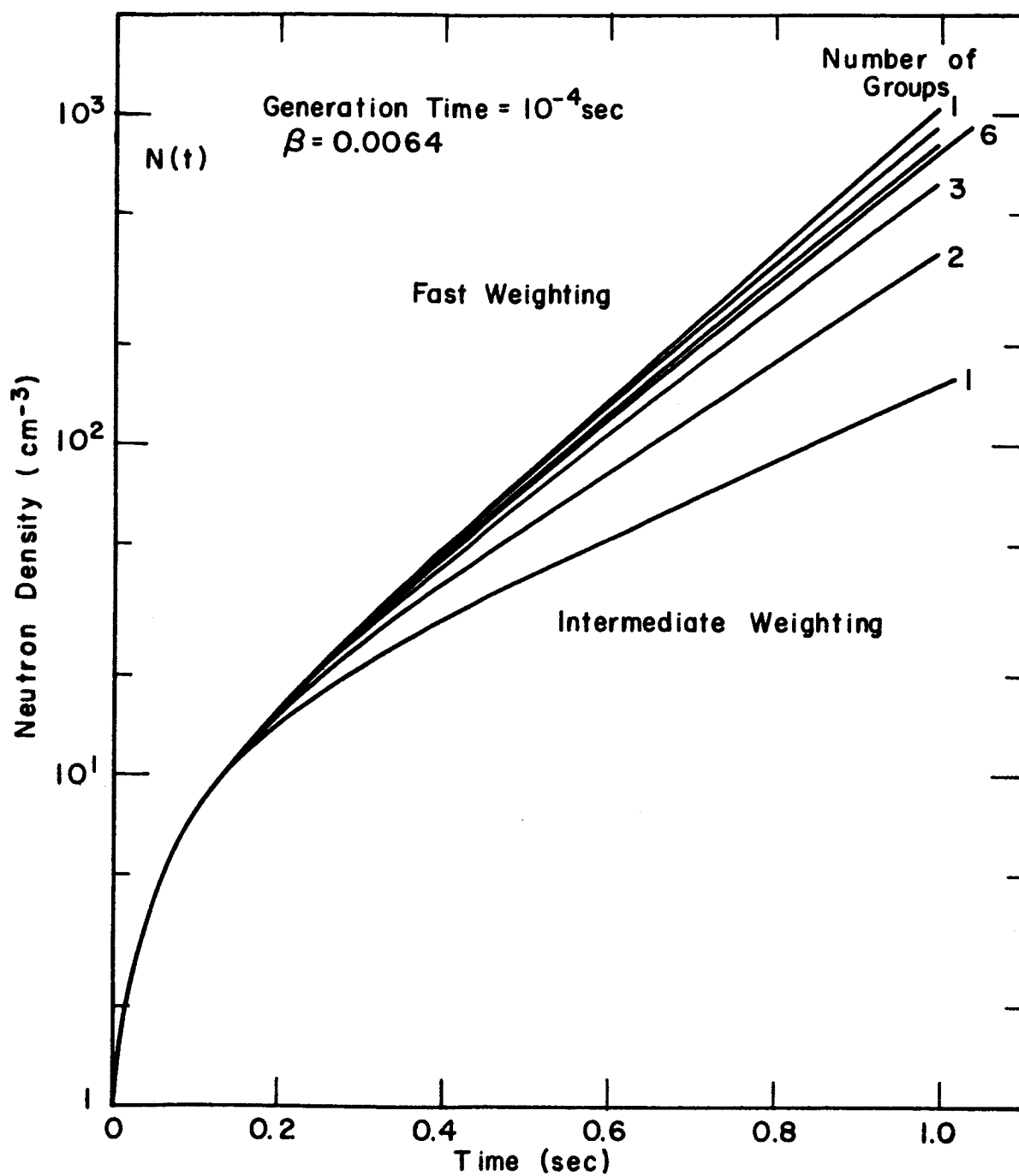Figure D6.1. Reactor Behavior for Fifty Cent Reactivity Step.

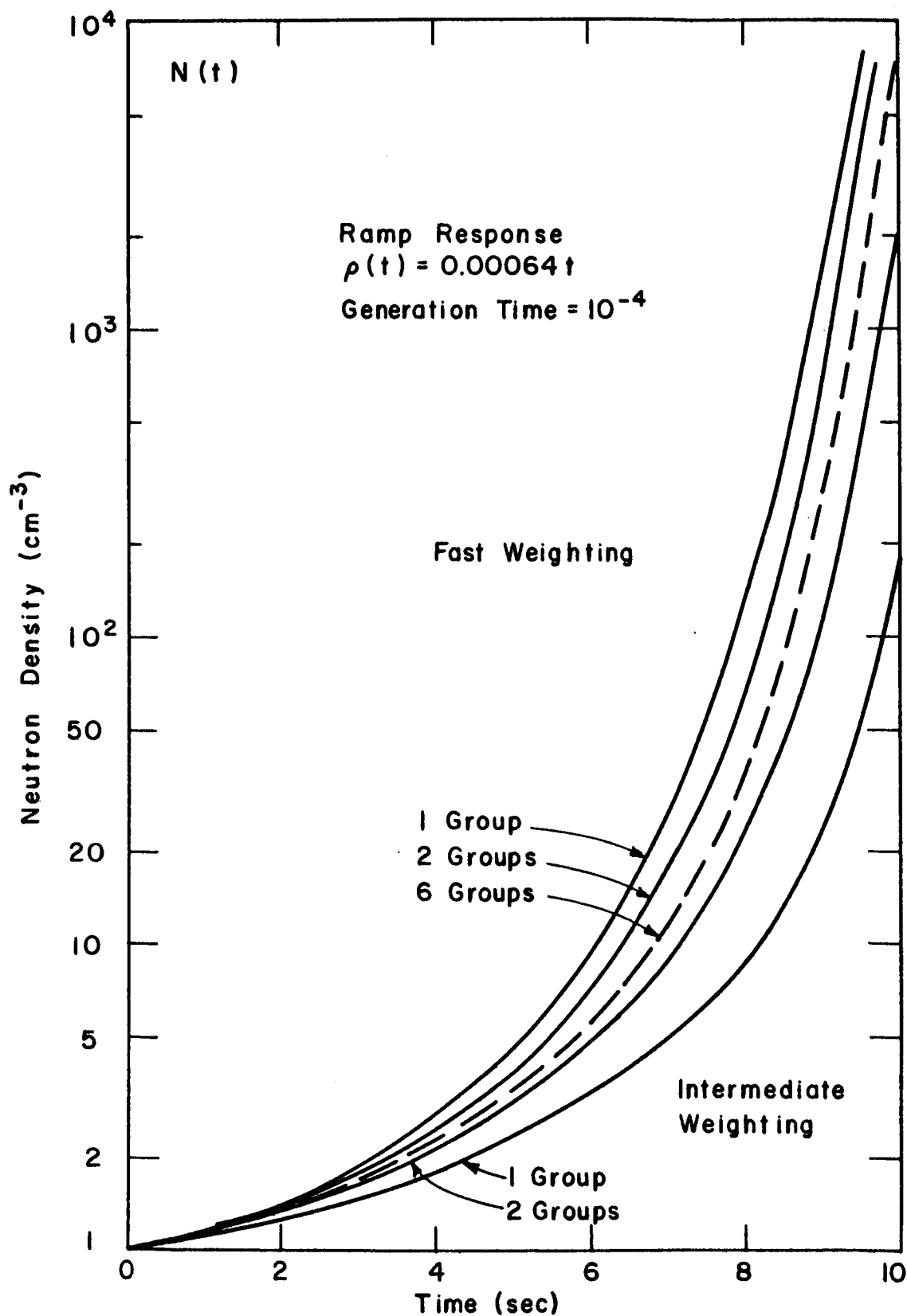Figure D6. 2. Reactor Behavior for a One Dollar Reactivity Step.

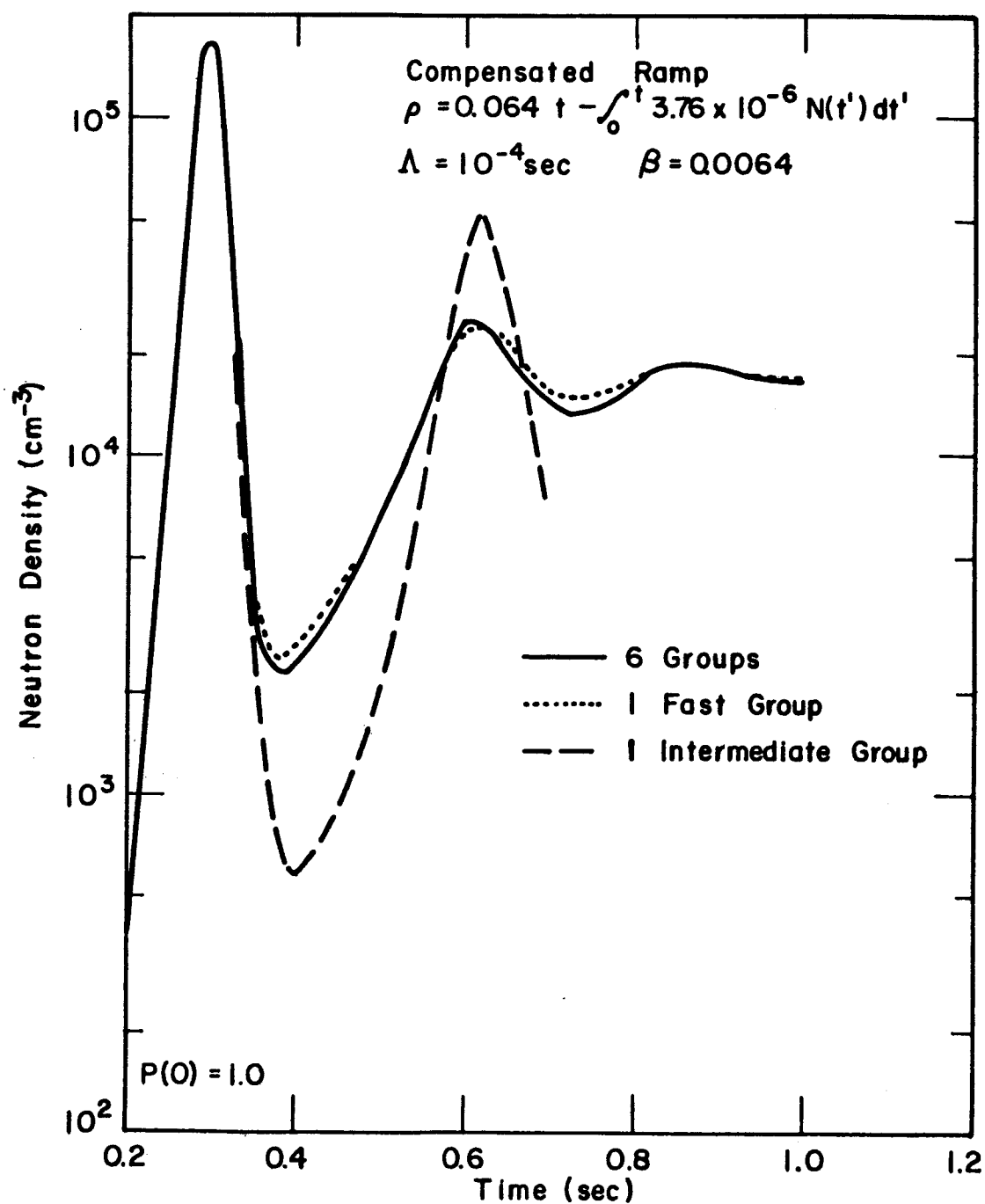Figure D6.3. Reactor Response for a Ten Cent Per Second Reactivity Insertion.

Figure D6. 4. Reactor Response for a Ten Dollar Per
Second Reactivity Insertion.

APPENDIX E
NUMERICAL SOLUTION TO THE KINETIC EQUATIONS

E1. Introduction

A rapid numerical solution to the kinetic equations is described in the following sections. This method was used to solve all kinetic problems discussed in Chapter VIII and Appendix D.

E2. Statement of Problem

In most numerical march-out procedures, the time step must be chosen so that the fractional change in the function is small for each time step. Therefore, if the function changes many orders of magnitude in the region of interest, many time steps are required.

It is well known that large positive reactivities cause the neutron density in a reactor to rapidly increase. More specifically, the neutron density profile is usually exponential in character during large excursions, and may traverse several orders of magnitude in a fraction of a second.

The approach presented in this section rapidly solves kinetic problems involving large reactivities. It offers no advantage over present methods for small reactivities.

E3. Derivation of March-out Algorithm

Consider the one energy group kinetic equations

$$\frac{dn}{dt} = \frac{\rho - \beta}{\Lambda} n + \sum_{1}^{G} \lambda_i C^i \qquad (E3.1)$$

$$\frac{dC^i}{dt} = \frac{\beta_i n}{\Lambda} - \lambda_i C^i \qquad (E3.2)$$

with G precursor groups. $-\omega_j n(t)$ is added to both sides of Eq. (E3.1), and then integrated. Hence,

$$n_{j+1} = e^{\omega_j h} \left[n_j + \int_0^h d\xi \left\{ \frac{\rho(\xi) - \rho_j}{\Lambda} n(\xi) e^{-\omega_j \xi} + \sum_1^G \lambda_i \left(C^i(\xi) - C^i_j \frac{n(\xi)}{n_j} \right) e^{-\omega_j \xi} \right\} \right]$$

(E3.3)

where: h = mesh width

  j = time index

$$\omega_j = \frac{\rho_j - \beta}{\Lambda} - \frac{1}{n_j} \sum_1^G \lambda_i C^i_j$$

In a similar manner, $-\gamma^i_j C^i(t)$ is added to both sides of Eq. (E3.2), and then integrated. Therefore,

$$C^i_{j+1} = e^{\gamma^i_j h} \left[C^i_j + \int_0^h d\xi \, e^{-\gamma^i_j \xi} \left\{ \frac{\beta_i}{\Lambda} \left(n(\xi) - \frac{n_j}{C^i_j} C^i(\xi) \right) \right\} \right]$$

(E3.4)

where

$$\gamma^i_j = \frac{\beta_i n_j}{\Lambda C^i_j} - \lambda_i$$

Clearly, ω_j and the γ^i_j's are merely approximations to the instantaneous period at time mesh j for the neutron density and precursor densities, respectively.

To evaluate the integrals in Eqs. (E3.3) - (E3.4), the first approximations

$$n(\xi) \cong e^{\omega_j \xi} n_j$$

(E3.5)

$$C^i(\xi) \cong e^{\gamma^i_j \xi} C^i_j$$

(E3.6)

are placed in the integrals, and the integration is performed using the trapezoidal rule. This leads to the final march-out algorithm

$$n_{j+1} = e^{\omega_j h} \left\{ n_j \left(1 + \frac{h}{2\Lambda} \left\{ \rho_{j+1} - \rho_j \right\} \right) + \sum_1^G \lambda_i C^i_j \left[\frac{e^{\left[h\left(\gamma^i_j - \omega_j \right) \right]} - 1}{\gamma^i_j - \omega_j} - h \right] \right\}$$

(E3.7)

$$C_{j+1}^i = e^{\gamma_j^i h} \left[C_j^i + \frac{n_j \beta_i}{\Lambda} \left\{ \frac{e^{h\left(\omega_j - \gamma_j^i\right)} - 1}{\omega_j - \gamma_j^i} - h \right\} \right] \qquad \text{(E3.8)}$$

The variable time step, h, is determined by the requirement that the first approximation for n_{j+1}, Eq. (E3.5), agree with the second approximation within a prescribed tolerance.

E4. Characteristic Running Times

Using six precursor groups, a prompt critical burst covering 20 orders of magnitude requires approximately 2-4 seconds of IBM-7094 time. A temperature shutdown term adds a few seconds to the above time estimate. These running times compare quite favorably with those quoted in the literature (38).

The error in n(t), obtained by comparison with a rigorous analytic computation, is considerably less than 1% for problems involving constant reactivities. Although error analysis has not been performed for variable reactivity problems, it appears, from varying the convergence criterion, that the error is still considerably less than 1%.

APPENDIX F
CONVERSION FACTORS

The list below contains physical constants and conversion factors useful for changes between the mks and English system of units.

Constants

$$N_o = 6.025 \times 10^{26}/(kg\text{-}mole)$$

$$R_o = 8317 \text{ joules}/(kg\text{-}mole\text{-}°K)$$

$$k = 1.380 \times 10^{-23} \text{ joules}/°K$$

Conversion Factors

length:	1 meter (m)	= 39.37 in
area:	1 m^2	= 1550 in^2
volume:	1 m^3	= 35.3 ft^3
mass:	1 kilogram	= 2.205 lb
power:	1 watt	= 3.413 BTU/hr
energy:	1 joule	= 0.2390 calories
force:	1 newton	= 0.2248 lb
pressure:	1 newton/m^2	= 1.450 $\times$ 10^{-4} lb/in^2
		= 0.987 $\times$ 10^{-5} atm
thermal conductivity:	1 watt/(m-°K)	= 0.5779 Btu/(hr-ft-°F)

APPENDIX G
INFORMATION ON CODES

Most of the mathematical models set up in this thesis were solved on an IBM-7094 digital computer. Because many long codes were written, it was not thought appropriate to include the entire flow charts and listings in this thesis. However, input information, listings, and FORTRAN decks are available through Professors E. A. Mason and K. F. Hansen for the following codes:

1. THERMAL SPECTRUM. This program solves the Wilkins Equation and computes average thermal cross sections.

2. SLOWING DOWN SPECTRUM. This code solves the Goertzel-Selengut model discussed in section 3.3.

3. KINETICS CODE. This code solves the kinetic equations by the algorithm discussed in Appendix E.

4. KINETICS CHECK CODE. This very short program solves the kinetic equations for step reactivity insertions. It was used to check the march-out method discussed in Appendix E.

5. REACTIVITY. In this brief code, the reactivity is computed as a function of time for a linear power buildup. The equations involved in this code are discussed in section 6.2.

6. FLUID FLOW. This rather long code computes the core temperature and hydrogen density distribution during startup using the heat transfer model described in Chapter IV.

REFERENCES

1. Strauss, L. L., <u>Men and Decisions</u>, Doubleday and Company, Inc., New York (1962).

2. Bussard, R. W., "Nuclear Rocketry – The First Bright Hopes," Astronautics 7 (December 1962).

3. Tsien, H. S., "Rockets and Other Thermal Jets Using Nuclear Energy, with a General Discussion on the Use of Porous Pile Materials," The Science and Engineering of Nuclear Power, Vol. 2, Addison-Wesley Press (1949).

4. Schreiber, R. E., "Los Alamos' Project Rover," Nucleonics, Vol. 16, No. 7, p. 62 (1958).

5. Rom, F. E., A. F. Lietzke, and P. G. Johnson, "Nuclear Rockets for Unmanned Missions," Nucleonics, Vol. 20, No. 11 (November 1962).

6. Johnson, P. G., "Nuclear-Rocket Applications," Astronautics, Vol. 7, No. 12, pp. 22-27 (December 1962).

7. Finger, H. B., "Managing the Nuclear Rocket Program," Astronautics, Vol. 7, No. 12 (December 1962).

8. Kramer, A. W., "Nuclear Power in Space Technology," Atomics, Vol. 16, No. 3 (May-June 1963).

9. Nucleonics, Vol. 21, No. 10, p. 28 (October 1963).

10. Nucleonics, Vol. 22, No. 7, p. 31 (July 1964).

11. Nucleonics, Vol. 21, No. 11, p. 26 (November 1963).

12. Nucleonics, Vol. 21, No. 12, p. 42 (December 1963).

13. Bogart, D. and E. Lantz, "Nuclear Physics of Solid-Core Gas-Cooled Rocket Propulsion Reactors," NASA-UNIVERSITY CONFERENCE on the SCIENCE and TECHNOLOGY of SPACE EXPLORATION, Vol. 2, Chicago (1962).

14. Plebuch, R. K., "Reactor Physics of Nuclear Rocket Reactors," ScD Thesis, Department of Nuclear Engineering, Massachusetts Institute of Technology (1963).

15. Meghreblian, R. V. and D. K. Holmes, Reactor Analysis, McGraw-Hill Book Company, Inc., New York (1960).

16. Cohen, E. R., Neutron Velocity Spectrum in a Heavy Moderator, Nuclear Science and Engineering 2, pp. 227-245 (1957).

17. Henrici, P., Discrete Variable Methods in Ordinary Differential Equations, John Wiley and Sons, Inc., New York (1962).

18. "Nuclear Data for GAM-I Data Tape," Vol. I and II, GA-2451 (August 1961).

19. Hughes, D. J. and R. B. Schwartz, "Neutron Cross Sections," Second edition, BNL 325 (1958).

20. Nelkin, M., "Neutron Thermalization II. Heavy Crystalline Moderator," Nuclear Science and Engineering 2, pp. 199-212 (1957).

21. Mills, C. B., "Physics of Intermediate Reactors," LAMS-2288 (Suppl. 1) (October 1959).

22. Nightingale, R. E., Nuclear Graphite, Academic Press, New York (1962).

23. Ellerbrock, H. H., N. B. Livingood, and D. M. Straight, "Fluid Flow and Heat-Transfer Problems in Nuclear Rockets," NASA UNIVERSITY CONFERENCE on the SCIENCE and TECHNOLOGY of SPACE EXPLORATION, Chicago (1962).

24. Hendricks, Graham and Mederios Hsu, "Correlation of Hydrogen Heat Transfer in Boiling and Supercritical Pressure States," American Rocket Society Journal (February 1962).

25. King, C. H., "Compilation of Properties of Gaseous Hydrogen," NASA TN D-275 (April 1960).

26. Bussard, R. W. and R. D. Delauer, Nuclear Rocket Propulsion, McGraw-Hill Book Company, Inc., New York (1958).

27. Shapiro, A. H., The Dynamics and Thermodynamics of Compressible Fluid Flow, Vol. I, The Ronald Press, New York (1953).

28. Mohler, R. R. and J. E. Perry, "Nuclear Rocket Enginer Control," Nucleonics, pp. 80-84 (April 1961).

29. Keepin, G. R., "Neutron Data for Reactor Kinetics," Nucleonics, No. 8, Vol. 20, pp. 150-156 (1962).

30. Tobias, M. L. and T. B. Fowler, "The 20-Grand Program for the Numerical Solution of Few-Group Neutron Diffusion Equations in Two Dimensions," ORNL-3200.

31. Henry, A. F., "The Application of Reactor Kinetics to the Analysis of Experiments," Nuclear Science and Engineering 3, pp. 52-70 (1958).

32. Gyftopoulos, E. P. and J. Devooght, "On the Range of Validity of Nonlinear Reactor Dynamics," Nuclear Science and Engineering, Vol. 10, No. 4 (August 1961).

33. Soodak, H., Reactor Handbook, Vol. 3, Part A, "Physics," Interscience Publishers, New York (1962).

34. Bonilla, C. F., Nuclear Engineering, McGraw-Hill Book Company, Inc., New York (1957).

35. Boley, B. A. and J. H. Weiner, Theory of Thermal Stresses, John Wiley and Sons, Inc., New York (1960).

36. Mason, E. A., Course Notes for Subject 22.27 at Massachusetts Institute of Technology, "Nuclear Power Sources for Space Applications" (1963).

37. Jansen, W. and J. K. Buckner, "Starting and Control Characteristics of Nuclear Rocket Engines," AIAA Journal, No. 3, Vol. 1, pp. 563-573 (1963).

38. Keepin, G. R. and C. W. Cox, "General Solution of the Reactor Kinetics Equations," Nuclear Science and Engineering 8, pp. 670-690 (1960).

BIOGRAPHY

The author, Winston W. Little, Jr., was born on September 4, 1938 in Gainesville, Florida. He attended P. K. Yonge High School in Gainesville, and received his diploma in June 1956. He entered M. I. T. in the Fall of 1956, and graduated in physics in June 1960. After spending a summer at General Atomic, the author entered M. I. T. Graduate School in the Department of Nuclear Engineering. He received an MS degree in Nuclear Engineering in February 1962, and continued his work at M. I. T. in Nuclear Engineering. While in graduate school, he received three AEC Fellowships in Nuclear Science and Engineering. The author spent the summers of 1962 and 1963 working at the Los Alamos Scientific Laboratory.